klahoma State University Library

ADSORPTION AND DECOMPOSITION OF CYANOGEN HALIDES ON Si(100) SURFACE. CHARACTERIZATION AND CHEMICAL REACTION KINETICS OF MICROCRYSTALLINE TUNGSTEN BRONZE THIN FILMS.

By

EVGUENI BORISOVICH KADOSSOV

Bachelor of Technics and Technology
Mendeleev University of Chemical Technology of Russia
Moscow, Russia
1997

Master of Technics and Technology
Mendeleev University of Chemical Technology of Russia
Moscow, Russia
1999

Submitted to the Faculty of the
Graduate College of the
Oklahoma State University
in partial fulfillment of
the requirements for
the Degree of
DOCTOR OF PHILOSOPHY
December, 2004

ADSORPTION AND DECOMPOSITION OF

CYANOGEN HALIDES ON Si(100) SURFACE.

CHARACTERIZATION AND CHEMICAL REACTION

KINETICS OF MICROCRYSTALLINE TUNGSTEN

BRONZE THIN FILMS.

Thesis Approved:

Thesis Adviser

Dean of the Graduate College

DEDICATION

Dedicated to my beloved mother

ACKNOWLEDGMENTS

First of all I would like to thank the Almighty God, the One in the Holy Trinity, whose invisible support gave me strength to finish this work. I believe that everything that happens to me occurs by His grace and according to His will.

My deepest gratitude must be expressed to my research adviser Dr. Nicholas Materer for his guidance and support while working on this dissertation. His knowledge and experience as well as the time and efforts helped me to improve significantly my scientific background. I wish to thank Dr. Lionel M. Raff and Dr. Paul A. Westhaus for their time spent on my advisory committee. My special thanks are due to Dr. Allen W. Appblett, whose assistance in obtaining XRD data cannot be overestimated. The help of the former members of my committee, Dr. Nicholas A. Kotov and Dr. Donald Thompson, is also appreciated. Dr. Kotov must be thanked for his support during my first months in the United States. Dr. Thompson's critical comments led me to acquiring a proper scientific attitude.

I appreciate the help in the experimental part of the work provided by Dr. P. Rajasekar, the post-doctoral fellow from Dr. Materer's group. My acknowledgments are also due to the other members of our group: Dane Scott, Christina Hummel and Kashif Khan. Their physical and moral supports have filled me with optimism and hope while doing this research. Terry Colberg provided helpful assistance in obtaining SEM data.

I personally thank Dr. Saman Alavi for his advices related to the computational part of the silicon adsorption project. And, of course, this work could not be done without the help of Mike Lucas, the head of the machine shop, where some necessary parts for the tungsten bronze films project were manufactured.

Finally, I wish to express gratitude to my parents who raised me, educated me and always taught me to learn more and more. Their love and support have always been the source of inspiration for me in all my doings. In addition, I appreciate material and moral help from my brothers, Dmitry and Alexey.

TABLE OF CONTENTS

Chapter .... Page

INTRODUCTION....................................1

I. ADSORPTION ON SILICON: BACKGROUND....................................4

A. Functionalization of silicon surface....................................4
B. Si(100) and Si(111) surfaces....................................4
B.1. Si(100) surface....................................5
B.2. Si(111) surface....................................8
C. Mechanism of adsorption on Si(100) surface....................................9
D. Adsorption of CN-containing substances on Si(100)....................................10
D.1. HCN....................................11
D.2. C_2N_2....................................11
D.3. CH_3CN....................................12
D.4. s-triazine....................................13

II. XCN ADSORPTION ON Si(100) SURFACE STUDIED BY XPS, UPS AND TPD....................................14

A. Introduction....................................14
B. Experimental part....................................16
B.1. XPS, UPS and TPD techniques....................................16
B.2. Reagents and materials....................................17
C. Results and discussion....................................19
C.1. XPS study....................................19
C.1.1. At low temperature....................................19
C.1.2. At room temperature....................................30
C.1.3. At higher temperatures....................................31
C.2. UPS study....................................37
C.2.1. At low temperature....................................37
C.2.2. At room temperature....................................40
C.2.3. At higher temperatures....................................43
C.3. TPD study....................................43
D. Conclusions....................................46

III. COMPUTATIONAL STUDIES OF ADSORPTION AND DISSOCIATION PATHWAYS OF CYANOGEN HALIDES ON Si(100) SURFACE 48

A. Introduction 48
B. Quantum computation procedure 49
C. Results and discussion 50
C.1. Gas-phase isomerization 51
C.2. One-molecule adsorption 52
C.2.1. Dissociation pathways parallel to the Si-Si dimer-bond 52
C.2.2. Dissociation pathways perpendicular to the Si-Si dimer bond 64
C.2.3. Cluster-size effects 71
C.3. Two-molecule adsorption 76
C.3.1. On a double-dimer cluster 76
C.3.2. On a triple-dimer cluster 79
C.3.3. On a v-trench cluster 80
D. Conclusions 87

IV. TUNGSTEN TRIOXIDE AND ITS COLORED HYDROGEN BRONZES 89

A. WO_3 thin films and mechanisms of their coloration 89
B. Reduction of tungsten oxide to colored bronzes 90
B.1. Thermochromic coloration 90
B.2. Photochromic coloration 92
B.3. Electrochromic coloration 93
B.4. Gasochromic coloration 94
C. Bleaching of hydrogen tungsten bronzes 95
D. Structural properties of WO_3 and its bronzes 96

V. PREPARATION AND CHARACTERIZATION OF POLYCRYSTALLINE TUNGSTEN BRONZE THIN FILMS 99

A. Introduction 99
B. WO_3 thin films preparation 99
B.1. Sputter deposition of W-films 99
B.2. Oxidation of W-films 100
B.3. Reduction of tungsten oxide into tungsten bronze 101
B.3.1. Chemical reduction in aqueous solution 101
B.3.2. Direct hydrogen exposure in a UHV chamber 102
C. Characterization of WO_3 and H_xWO_3 thin films 102
C.1. XRD and SEM 102
C.2. XPS 107
C.3. UPS and UV-Vis 111
D. Conclusions 112

VI. KINETICS OF OXIDATION OF TUNGSTEN BRONZE THIN FILMS WITH NITROBENZENE....118

A. Introduction....118
B. Experimental....118
C. Kinetic model....119
C.1. Oxidation of tungsten bronze thin films....119
C.2. Oxidation of tungsten bronze in a powder form....124
D. Reaction rate measurements....126
E. Conclusions....129

CONCLUDING REMARKS....130

BIBLIOGRAPHY FOR CHAPTERS I-III....133

BIBLIOGRAPHY FOR CHAPTERS IV-VI....142

LIST OF TABLES

Table Page

II-1. The XPS C 1*s* peak position after a saturation exposure of ICN, BrCN and ClCN on Si(100) surfaces at low (100 K) and room (300 K) temperatures....26

III-1. B3LYP geometries (distance in Å and angles in degrees), fundamental frequencies, ν_1 – IC stretching mode, ν_2 – bending mode, ν_3 – CN stretching mode, (cm^{-1}) and relative energies (kJ/mol) of ICN and INC with respect to ICN obtained utilizing the Set 1 (LanL2DZ+6-31G*) and the Set 2 (CEP-31G+6-31G*)....51

III-2. B3LYP calculated geometries and adsorption energies (kJ/mol) for the ICN adsorption structures on single-dimer clusters....55

III-3. Calculated B3LYP/6-31G* adsorption energies (kJ/mol) for XCN1, XCN2, XCN3, SiNC and SiCN adsorption structures on single-dimer (1D) and triple-dimer (3D) clusters....59

III-4. Calculated B3LYP/6-31G* adsorption energies (kJ/mol) for the single-dimer transition state models....62

III-5. Calculated B3LYP/6-31G* geometries for TS1 and TS2 transition states on a single-dimer (1D) cluster....62

III-6. Calculated B3LYP/6-31G* geometries for TS3, TS4 and TS5 transition states on single-dimer clusters....62

III-7. Calculated B3LYP/6-31G* adsorption energies (kJ/mol) for one-molecule ClCN adsorption structures on a double-dimer $Si_{15}H_{16}$ cluster....66

III-8. Calculated B3LYP/6-31G* adsorption energies (kJ/mol) of the transition states for one-molecule ClCN adsorption structures on a double-dimer $Si_{15}H_{16}$ cluster....66

III-9. Calculated B3LYP/6-31G* geometries for XCN1 and XCN2 adsorption structures on single-dimer (1D) and triple-dimer (3D) clusters....73

III-10. Calculated B3LYP/6-31G* geometries for SiNC and SiCN adsorption

structures on single-dimer (1D) and triple-dimer (3D) clusters..........................75

III-11. Calculated B3LYP/6-31G* adsorption energies (kJ/mol) for one-molecule ClCN adsorption structures on a single-dimer (Si_9H_{12}) and v-trench ($Si_{23}H_{24}$) clusters..........................76

III-12. Calculated B3LYP/6-31G* adsorption energies (kJ/mol) for the second ClCN molecule adsorption structures on a double-dimer $Si_{15}H_{16}$ cluster..........................80

III-13. Calculated B3LYP/6-31G* adsorption energies (kJ/mol) of the transition states for the second ClCN molecule adsorbed on SiNC1 and SiCN1 double-dimer $Si_{15}H_{16}$ cluster sites..........................80

III-14. Calculated B3LYP/6-31G* adsorption energies (kJ/mol) for the second ClCN molecule adsorption structures on a triple-dimer $Si_{21}H_{20}$ cluster..........................84

III-15. Calculated B3LYP/6-31G* adsorption energies (kJ/mol) for the second ClCN molecule adsorption structures on a v-trench cluster..........................84

V-1. Relative amounts (%) of different tungsten oxidation states in non-hydrogenated and hydrogenated WO_3 thin films..........................111

LIST OF FIGURES

Figure Page

I-1. Si(100) and Si(111) surfaces....6

I-2. Si(100)-2×1 surface after reconstruction....7

II-1. Interaction between the lone electron pair of a halogen atom and the π-system of CN-bond: (a) Out-of-phase combination (b) In-phase combination....15

II-2. Nitrogen and carbon 1*s* XPS spectra as a function of ICN exposure to the Si(100) surface at 100 K....21

II-3. Nitrogen and carbon 1*s* XPS spectra as a function of BrCN exposure to the Si(100) surface at 100 K....23

II-4. Nitrogen and carbon 1*s* XPS spectra as a function of ClCN exposure to the Si(100) surface at 100 K....25

II-5. Si(100) XPS spectra for the (a) iodine 4*d*, (b) bromine 3*d* and (c) chlorine 2*p* peak as a function of the respective cyanogen halide exposure at 100 K....28

II-6. Carbon 1*s* XPS spectra as a function of (a) 0.2 L to 20 L ICN, (b) 0.3 L to 42 L BrCN and (c) 0.3 L to 33 L ClCN exposures to the Si(100) surface at 300 K....32

II-7. Nitrogen and carbon 1*s* XPS spectra from a Si(100) surface initially exposed to 25 L of molecular ICN at 100 K and annealed to various temperatures for 1 minute....34

II-8. Nitrogen and carbon 1*s* XPS spectra from a Si(100) surface initially exposed to 40 L of molecular BrCN at 300 K and annealed to various temperatures for 1 minute....35

II-9. Nitrogen and carbon 1*s* XPS spectra from a Si(100) surface initially exposed to 33 L of molecular ClCN at 300 K and annealed to various temperatures for 1 minute....36

II-10. He(I) UPS spectra of Si(100) after various exposures to (a) ICN, (b) BrCN and (c) ClCN at 100 K....39

II-11. He(I) UPS spectra for exposure of (a) ICN, (b) BrCN and (c) ClCN to the Si(100) surface at 300 K....42

II-12. TPD spectra of ICN^{2+} (76.5 amu) using a heating rate of 2 K/s....45

III-1. XCN derived adsorption models on the Si single-dimer cluster. (a) XCN1: XCN adsorbed on Si(100) surface in an end-on position. (b) XCN2: XCN adsorbed on Si(100) surface in a side-on position....53

III-2. Additional XCN derived adsorption models on the Si single-dimer cluster. (a) XCN3: Dissociated X and CN species adsorbed in a side-on position. Both the X-C and the silicon dimer bonds are broken. (b) SiNC: Dissociated X and NC species adsorbed on Si(100) surface. (c) SiCN: Dissociated X and CN species adsorbed on Si(100) surface....57

III-3. XCN1 adsorption model utilizing the Si triple-dimer cluster....58

III-4. Potential energy profile for different adsorption modes of XCN and their transition states on Si single-dimer cluster....60

III-5. First adsorption and dissociation pathway perpendicular to the dimer bond for one ClCN molecule adsorbed on a double-dimer cluster....67

III-6. Potential energy profile for different adsorption modes of one ClCN molecule on a double-dimer cluster corresponding to the first pathway perpendicular to the dimer bond....68

III-7. Second adsorption and dissociation pathway perpendicular to the dimer bond for one ClCN molecule adsorbed on a double-dimer cluster....69

III-8. Potential energy profile for different adsorption modes of one ClCN molecule on a double-dimer cluster corresponding to the second pathway perpendicular to the dimer bond....70

III-9. Two possible configurations for molecular ClCN adsorbed on a v-trench cluster....77

III-10. Adsorption of the second ClCN molecule on double-dimer dissociated structures with the lowest values of adsorption energies: (a) 1ClCN-SiNC2 (b) 1ClCN-SiCN2 (c) 2ClCN-SiNC2 (d) 2ClCN-SiCN2....81

III-11. Dissociation pathway for the second ClCN molecule adsorbed on a dissociated structure with Cl and CN species bound to the same dimer bond....82

III-12. Potential energy diagram for different adsorption modes corresponding to the dissociation of the second ClCN molecule on a double-dimer

cluster with Cl and CN species bound to the same dimer-bond....83

III-13. Structures of two ClCN molecules adsorbed in an end-on position on a triple-dimer cluster: (a) 1ClCN1-ClCN1 (b) 2ClCN1-ClCN1 (c) 3ClCN1-ClCN1 (d) 4ClCN1-ClCN1....85

III-14. Structures of two ClCN molecules adsorbed in an end-on position on a v-trench cluster: (a) 1ClCN1-ClCN1 (b) 2ClCN1-ClCN1 (c) 3ClCN1-ClCN1....86

IV-1. Schematic bandstructure for WO_3 defect perovskite structure....91

IV-2. The cubic "ReO_3 type" structure of WO_3....97

V-1. XRD spectrum of a microcrystalline tungsten thin film....103

V-2. XRD spectrum of a WO_3 thin film....104

V-3. XRD spectrum of a hydrogen tungsten bronze thin film....105

V-4. SEM-micrograph of a 210 nm WO_3 film....106

V-5. XPS spectra of (1) a H_xWO_3 thin film (2) H_xWO_3 in a powder form....108

V-6. XPS spectrum and deconvolution curves for W 4*f* peak in a non-hydrogenated WO_3 film....109

V-7. XPS spectrum and deconvolution curves for O 1*s* peak in a non-hydrogenated WO_3 film....110

V-8. XPS spectrum and deconvolution curves for W 4*f* peak in a hydrogenated H_xWO_3 film....113

V-9. XPS spectrum and deconvolution curves for O 1*s* peak in a hydrogenated H_xWO_3 film....114

V-10. UPS spectra of (1) a H_xWO3 thin film (2) a non-hydrogenated WO_3....115

V-11. UV-Vis absorbance spectra of 30 nm WO_3 and H_xWO_3 thin films....116

VI-1. Oxidation kinetics of H_xWO_3 thin films of different thickness in 0.1M solution of nitrobenzene in Hexanes....120

VI-2. Time dependent proton concentration distribution in a tungsten bronze film with thickness L....122

VI-3. Thickness dependence of the relaxation time for H_xWO_3 thin films oxidized in 0.1M solution of nitrobenzene in Hexanes..127

VI-4. Concentration dependence of the relaxation time for 103 nm H_xWO_3 thin films oxidized in the solution of nitrobenzene in n-Hexane..........................128

LIST OF SYMBOLS AND ABBREVIATIONS

Symbol	Meaning
∠SiSi	Si-Si dimer bond bucking angle
b	Reaction rate
C	Concentration
C_H	Hydrogen Concentration
CMA	Cylindrical Mirror Analyser
const	Constant
C_{ox}	Oxidant Concentration
D	Diffusion coefficient
d	Thickness
E_F	Fermi level
E_{rel}	Relative energy
F	Deposition rate
FWHM	Full Width at Half Maximum
HREELS	High Resolution Electron Energy Loss Spectroscopy
I	Absorbance intensity
i	Current
IRC	Internal Reaction Coordinate
k	Reaction constant
L	Film thickness

M	Molecular weight
n	Number of moles
NEXAFS	Near Edge X-Ray Absorption Fine Structure
NMR	Nuclear Magnetic Resonance
PES	Synchrotron Radiation Photoemission Spectroscopy
R	interatomic distance
S	Number of surface sites
SEM	Scanning Electron Microscopy
$Si_{15}H_{16}$	Double-dimer Si(100) cluster
$Si_{21}H_{20}$	Triple-dimer Si(100) cluster
$Si_{23}H_{24}$	V-trench Si(100) cluster
Si_9H_{12}	Single-dimer Si(100) cluster
STM	Scanning Tunneling Microscopy
T	Temperature
t	Time
TDS	Thermal Desorption Spectroscopy
TMP	Turbo-Molecular Pump
TPD	Temperature Programmed Desorption
TS	Transition State
U	Potential
UHV	Ultra-High Vacuum
UPS	Ultraviolet Photoelectron Spectroscopy
UV-Vis	Ultraviolet-Visible (Spectroscopy)

XCN	Halogen cyanide where halogen is chlorine, bromine or iodine
XPS	X-Ray Photoelectron Spectroscopy
XRD	X-Ray Diffraction
λ	Wavelength
ρ	Density
θ	Surface coverage
τ	Relaxation time

INTRODUCTION

This work consists of two independent research projects. The first one is related to the functionalization of silicon surface with CN-containing compounds, namely cyanogen halides. The second project is devoted to oxidation kinetics of hydrogen tungsten bronze thin films prepared by thermal oxidation of sputter deposited tungsten films.

Chapter I contains a brief review devoted to silicon surface functionalization with organic species. The significance of this area can be realized from the application perspective of silicon surface functionalized with different organic groups. Such systems have possible use in electronic devices that combine the properties of conventional semiconductor with the features of an attached functional group. Potential applications of such hybrid materials may include sensors, devices for implantation, molecular memories. Organic covering can also be used for protection and passivation of silicon semiconductor surface.

Since all organic groups contain carbon and nitrogen species the study of adsorption of C- and N-containing functional groups on Si surface is important for better understanding the mechanism of Si surface functionalization with a broad class of organic species. Adsorption of some CN-containing compounds (HCN, C_2N_2, $(HCN)_3$) on Si surface has already been investigated both theoretically and experimentally; however, it turned out to be impossible in all these cases to form -C≡N covering without

undesirable side reactions and corresponding by-products (like HCNC). In the current research XCN (X=I, Br or Cl) species were used as precursors to produce uniform –CN films on Si(100) surface since X-C bond easily dissociates and halogen atom, unlike hydrogen, does not form by-products with CN species. In Chapter II the adsorption of ICN, BrCN and ClCN on Si(100) surface was studied experimentally by means of XPS, UPS and TPD techniques. To further support the experimental results, in Chapter III the adsorption of XCN on Si(100) was also investigated by quantum calculations. In this case the Si(100) surface was represented by hydrogen-terminated clusters containing different number of dimer bonds. Both experimental and calculation data agree on the formation of dissociated halogen and CN species on Si surface at room temperature as a result of XCN adsorption without side reactions.

Chapter IV is devoted to the review of tungsten bronze thin films and their properties. The reason for the interest to this field rests in the ability of tungsten oxide to reversibly change its optical properties when reducing to bronze. Visually, a transparent yellow tungsten oxide film becomes deep-blue after reduction. Among the applications of tungsten oxide films are oxide gas sensors, "smart windows", displays. However, reducing ability of tungsten bronze may play a significant role in building devices for deactivation of explosives since many of them contain nitrogen oxides functional groups, which can be reduced to $-NH_2$. Hence, the investigation of tungsten bronze reactions with nitro-containing substances is of great importance for further advances in development of new modern types of explosive deactivation techniques.

In Chapter V of this dissertation tungsten oxide thin films were prepared and then reduced to their hydrogen bronzes by means of hydrogen evolving in the reaction of Zn

powder with HCl aqueous solution. Another method of tungsten bronze preparation includes direct hydrogenation of WO_3 films in an ultra-high vacuum chamber. The characterization of the films was done by various methods including XPS, UPS, UV-Vis, SEM and XRD. In Chapter VI the reaction kinetics of tungsten bronzes with nitrobenzene solution, studied by UV-Vis spectroscopy, is described. The appropriate kinetic model was developed and then fitted to the experimental data. Due to such an approach both the reaction constant and the diffusion coefficient of tungsten bronze thin films can be determined. These parameters are significant for manufacturing explosive deactivation devices because they relate the actual concentration of nitro-containing compounds with the optical property of tungsten bronze films. The value of the diffusion coefficient is compared with the results obtained previously by NMR study of hydrogen transport in tungsten oxide thin films.

CHAPTER I

ADSORPTION ON SILICON: BACKGROUND

A. Functionalization of silicon surface.

The surface functionalization of group IV semiconductors with organic molecules promises the opportunity to create devices that exploit combined properties of organic materials with conventional semiconductors. The adsorption of organic molecules to fine-tune the chemical and physical properties of the surface has applications in chemical sensors, biological recognition, and molecular and optical electronics.[1] The possible application of such a technique may be a chemical or biological sensor, in which the organic layer is terminated with different types of end groups sensitive to chemical or biological stimuli. The signal, occurring from the binding of the species of interest to the end group, can be coupled into the silicon substrate and then processed with the help of silicon microchip. Other possible application areas of hybrid organic/semiconductor materials are molecular electronics and biocompatible semiconductor devices for implantation. Besides that, they can be employed in manufacturing new-generation dielectric materials for metal interconnect isolation and for surface passivation and protection.[2]

B. Si(100) and Si(111) surfaces

The most widely studied silicon surfaces result from cutting the Si diamond

crystal in (100) and (111) directions producing the corresponding Si(100) and Si(111) surfaces (Fig. I-1). To reduce their energy both surfaces undergo reconstruction resulting in Si(100)-2×1 and Si(111)-7×7 surfaces.[3,4]

B.1. Si(100) surface

The ability of Si(100) to form stable oxides combined with low density of surface states provides a great opportunity for using Si(100) surface in microelectronics manufacturing. To realize this, a fundamental understanding of the reactivity of the Si(100) surface towards various organic compounds is required. The Si(100)-2×1 surface contains repeating units (dimers) with dimer bonds on their surface, which are responsible for the surface reactivity. Usually in quantum calculations only a small part ("cluster") consisting of one or several such units is used instead of the infinite surface. Figure I-2 shows a picture of the reconstructed Si(100) surface. From the formal point of view the dimer bond can be described in terms of a σ-bond and a π-bond, similar to a double C=C bond in alkenes.[4,5] Nevertheless, because of the large Si-Si distance the π-bond is relatively weak and can be considered in some cases as diradical.[6] The buckling of the Si dimer atoms is accompanied by the charge transfer from the buckled down atom to the buckled-up one.[7] STM measurements at low temperatures confirm the presence of buckled dimers with the ordering c(4×2), although the regions with p(2×2) symmetry also exist.[8] At room temperature STM experiments reveal symmetric arrangement of the dimers due to flip-flop type of motion of their dangling bonds.[9,10] According to the quantum calculation results[11,12], one of the major factors that controls dimer tilting is the electron correlation effect. Another factor is the electron-phonon coupling between

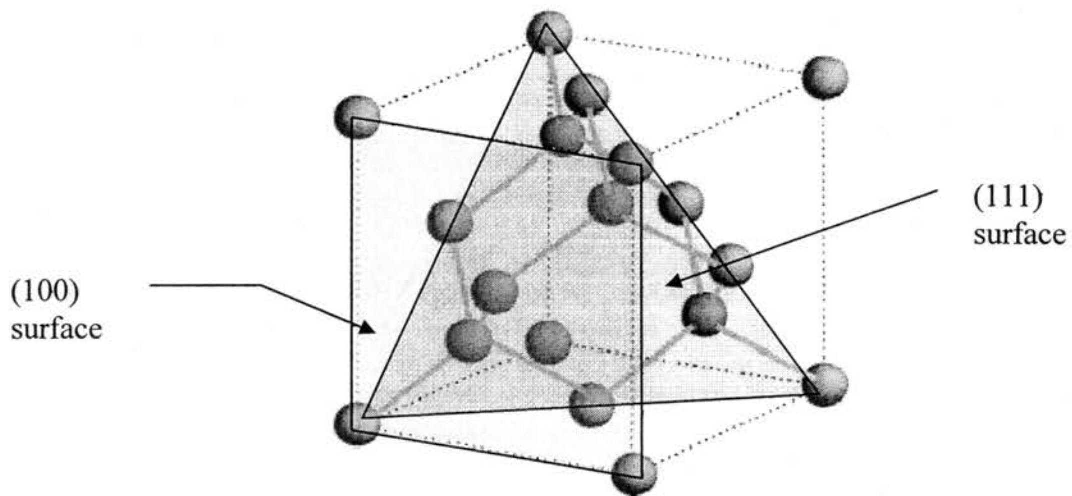

Figure I-1. Si(100) and Si(111) surfaces. The diamond structure of silicon is adapted from http://hyperphysics.phy-astr.gsu.edu/hbase/solids/sili2.html.

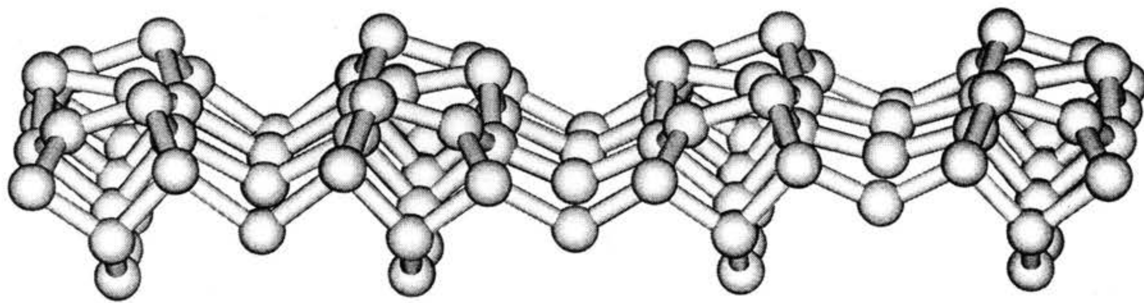

Figure I-2. Si(100)-2×1 surface after reconstruction.

Shockley surface states in the vicinity of the Fermi energy and the deformation modes. The coupling between dimerization and buckling distortions is primarily caused by the interaction between bridge and dangling bonds in the Si(100) surface.[13,14] Such unique bonding of the Si(100) surface provides high chemical reactivity towards a broad variety of organic and inorganic molecules.[15]

The adsorption and decomposition of many organic compounds containing N and O with the Si(100) surface has recently been reviewed.[16] One important feature of the Si(100) surface is the presence of Si dimers that act as electron acceptors and play a critical role in the adsorption chemistry of nitrogen containing organic compounds.[17-19] The surface reactions of Si(100) with many substances including NH_3,[20,21] N_2H_4,[22-24] HN_3,[25,26] CO,[27-30] CH_2O,[31,32] CH_3OH,[31] HCOOH,[33-35] NH_2CHO,[36] Pyrrole,[18,37,38] Tiophene,[39,40] s-triazine,[41] have been explored.

B.2. Si(111) surface

The structure of Si(111)-7×7 surface after reconstruction adopts the so-called dimer-adatom-stacking-fault (DAS) configuration.[42] The upper layer contains chemically non-equivalent atoms, leading to a number of spatially inhomogeneous chemical sites. Seven distinguishable types of surface atoms constitute the (7×7) surface unit cell. They, in turn, produce 19 dangling bonds, which participate in chemical reactions. Twelve of these bonds are situated at upper adatoms, while other six are at the rest atoms and the remaining one – at the corner atom in the fourth layer. It was predicted theoretically that charge transfer occurs from the adatoms to the rest atoms.[43] Such a process leads to completely occupied dangling bonds at the rest atoms as well as the corner hole atoms

and partially occupied or empty dangling bonds at the adatoms. These predictions were confirmed by scanning tunneling microscopy (STM).[44,45] It should be expected that chemical reactivity of the Si(111)-(7×7) is related to the inhomogeneous dangling bond states on the surface. The adsorption of a variety of species has been studied on the Si(111) surface: ammonia,[45] N_2H_4,[46] HN_3,[47] CO,[29] CH_3CHO,[48] CH_2CO,[49] methanol,[50] HCOOH,[33] HCN,[51] CH_3CN,[52] C_2N_2,[53] $CH_3N_2H_3$,[46] pyrrole,[54] thiophene,[55] furan[55] and pyridine.[52]

C. Mechanism of adsorption on Si(100) surface

Since the dimer bond of a Si(100) surface cluster can be considered at some approximation as a double bond, the adsorption mechanism should be very similar to that found for alkene reactions.[2] One useful class of these reactions are cycloaddition reactions. These are the reactions in which two π-bonds interact, forming a new cyclic molecule and making two new σ-bonds. There are two main types of cycloaddition reactions for alkenes: [2+2] cycloaddition and [4+2] cycloaddition, also known as the Diels-Alder reaction. In the first type of reaction, two alkene molecules react to form a four-member ring. In [4+2] cycloaddition, a diene molecule reacts with an alkene. As a result, a six-member ring is produced. One of the biggest difficulties with [2+2] cycloaddition is that it violates a Woodward-Hoffman selection rule, stating that in order for the reaction to be "symmetry-allowed", the molecular orbitals must overlap "in phase". Therefore, the [2+2] reaction (and, consequently, the adsorption of alkene-type molecules on the Si(100) surface) cannot occur without a significant transition barrier.

Nevertheless, the alkene adsorption takes place quite easily,[56] apparently contradicting the Woodward-Hoffman rule. Several mechanisms were proposed to explain this fact.[57] One of them, proceeding via the formation of a π-complex precursor and a singlet diradical intermediate was supported by density-functional quantum calculations. The STM experiments confirmed the calculation results showing that adsorption of alkenes on Si(100) is not stereospecific, but highly stereoselective in nature.[58] Besides the common intradimer [2+2] cycloaddition, the interdimer [2+2] addition mechanism, in which an alkene molecule initially adsorbs across the dimer bonds is also possible.[59]

Due to buckling of surface Si atoms, accompanied by charge distribution, adsorption of O-, N- and halogen-containing species occurs through the dative bonding between the lone pair of the species and an electrophilic buckled-down silicon.[21,60,61] Therefore, this positively charged buckled-down atom is primarily responsible for adsorption of molecules with atoms containing electron lone pairs.

D. Adsorption of CN-containing substances on Si(100)

The interaction of carbon-nitrogen containing molecules with Si(100) is of practical importance for the understanding of chemical vapor deposition of CN_x films. Amorphous thin CN_x films are chemically inert and exhibit crystalline texture and a wide bandgap.[62-65] From a more fundamental perspective, the surface chemistry of carbon nitrogen triple-bonded moieties (CN) complements the current effort to advance the mechanistic understanding of chemical reactions of carbon and nitrogen containing species with the Si(100) surface.

D.1. HCN

Hydrogen cyanide (HCN) has been studied experimentally by M. C. Lin and coworkers on the Si(100) surface by means of XPS, UPS and HREELS.[66] The addition of the adsorbed H atom complicates the surface chemistry by reacting with the CN functional group. It was found that at high exposures, HCN dimerizes and possibly polymerizes on the Si(100) surface at low temperatures. Upon warming, iminium (HC-NH) and CN species were identified as decomposition products. Heating above 680 K leads to the dissociation of NH and CN bonds, whereas annealing to the temperatures greater than 820 K results in the formation of Si carbides and nitrides.

The theoretical studies of HCN adsorption and decomposition pathway have also been performed.[67,68] In this case the Si(100) surface was represented by the single-dimer (Si_9H_{12}) and double-dimer ($Si_{15}H_{16}$) models. The results reveal that HCN can adsorb molecularly or dissociatively in an end-on or side-on configuration leading eventually to the dissociated H and CN species on the surface as the most thermodynamically favorable mode. The investigation of adsorbate-adsorbate interactions for HCN on the Si(100) surface observes the synergetic effect for the parallel adsorption of two HCNs with their groups bridging across the two dimers. On the other hand, the adsorbate-adsorbate interaction is negligible in the case of a side-on adsorption configuration.

D.2. C_2N_2

The adsorption and decomposition studies of C_2N_2 on Si(100) done by TPD, XPS, UPS and HREELS show that at low temperatures C_2N_2 adsorbs molecularly. After annealing to 600 K, the NC-CN bond breaks and CN species were identified on the

surface.[53] Above 800 K, the CN adsorbed species decompose into silicon carbides and nitrides.

Quantum computations involving single-dimer (Si_9H_{12}) and double-dimer ($Si_{15}H_{16}$) clusters were performed to investigate the adsorption of C_2N_2 on the Si(100) surface.[69] The single-dimer model computations revealed that the adsorption of C_2N_2 molecule occurred through the interaction of one N atom with Si atom of the surface. Two further reaction pathways are possible; the first one via the adjacent carbon atom adsorption producing a four-member ring product –Si-N-C-Si-. The other pathway involves interaction of the second nitrogen atom with the surface giving rise to a six-member-ring species –Si-N-C-C-N-Si-. The calculations involving double-dimer cluster show that the reaction barriers are lower than those for the single-dimer system. The predicted stabilities of various surface species resulting from adsorption of C_2N_2 on Si(100) are consistent with the experimental studies described above.

D.3. CH_3CN

The adsorption of acetonitrile on the Si(100) surface has been studied both experimentally and theoretically. TPD, XPS and HREELS studies show that acetonitrile chemisorbs on Si(100) in a side-on di-σ binding configuration, forming Si-C and Si-N σ bonds.[70] The analogous results were obtained by using PES and NEXAFS techniques.[71] The quantum computations predicted two adsorption configurations: end-on and side-on ones with the predicted energies equal to -66.1 and -116.3 kJ/mol correspondingly. The last structure can be obtained directly from the gaseous phase or from the end-on configuration via a transition barrier with the height of 38.1 kJ/mol.[16] The work of Miotto

and coworkers[72] suggests that the di-σ–CN model is found to be the most probable adsorbed structure from the energetic point of view. The adsorption via the Si-N dative bond is also possible.

D.4. s-triazine.

The thermal decomposition of s-triazine ($C_3N_3H_3$) adsorbed on Si(100) was investigated with the help of XPS, UPS, HREELS and TDS techniques.[41] Above 200 K s-triazine lies flat on the surface. Annealing to 550 K causes the dissociation of $C_3N_3H_3$ into HC=N, leading to formation of NH and SiH species. Above 800 K a mixture of silicon nitrides and carbides is produced. Density functional calculations using a single-dimer cluster revealed two chemisorption states with the energy values equal to 76.2 kJ/mol and 107.5 kJ/mol.[16] The first one corresponds to the end-on configuration with a dative bond between the lone pair of the N atom of s-triazine and the buckled-down electrophilic Si atom of the dimer bond. The second energy value is attributed to the side-on structure, produced via a [4+2] cycloaddition mechanism.

In addition to HCN and organic nitriles, the adsorption of phenyl isothiocyanate[73] and benzonitrile[74] has been studied experimentally on the Si(100) surface. At room temperature, the CN group undergoes a 1,2-dipolar addition reaction across the Si-dimer bonds forming a surface product that contains a four-member Si-N-C-Si ring.

CHAPTER II

XCN ADSORPTION ON Si(100) SURFACE STUDIED BY XPS, UPS AND TPD

A. Introduction

The adsorption and thermal chemistry of XCN (X=I, Br and Cl) on Si(100) surface were studied both theoretically and experimentally, using ultraviolet photoelectron spectroscopy (UPS), X-ray photoelectron spectroscopy (XPS), and temperature programmed desorption (TPD). The content of this chapter is based on the results reported in Refs. 75, 76.

The ground state of the iodide, bromide and chloride cyanogen halides in the gas phase has been determined to be a $^1\Sigma^+$ state with a $(1\sigma)^2(2\sigma)^2(3\sigma)^2(1\pi)^4(4\sigma)^2(2\pi)^4$ electron configuration for the valence electrons.[77-83] An important aspect of the chemical binding between the halogen and the CN group is the overlap between the atomic *p* orbital centered on the halogen and the π system of the CN group. This overlap splits the originally degenerate π system into two energetically distinct molecular orbitals, an in-phase (1π) and an out-of-phase (2π) combinations (Fig. II-1). For a molecular ICN film on Si(100), the out-of-phase combination results in one broad peak at 4.4 ± 0.4 eV with respect to the Fermi energy. The in-phase combination is energetically close to the $^2\Sigma^+$ photoelectron peak from the nitrogen lone pair (the 4σ molecular orbital).[78] Surface broadening merges these transitions into one broad peak at 6.7 ± 0.4 eV with respect to

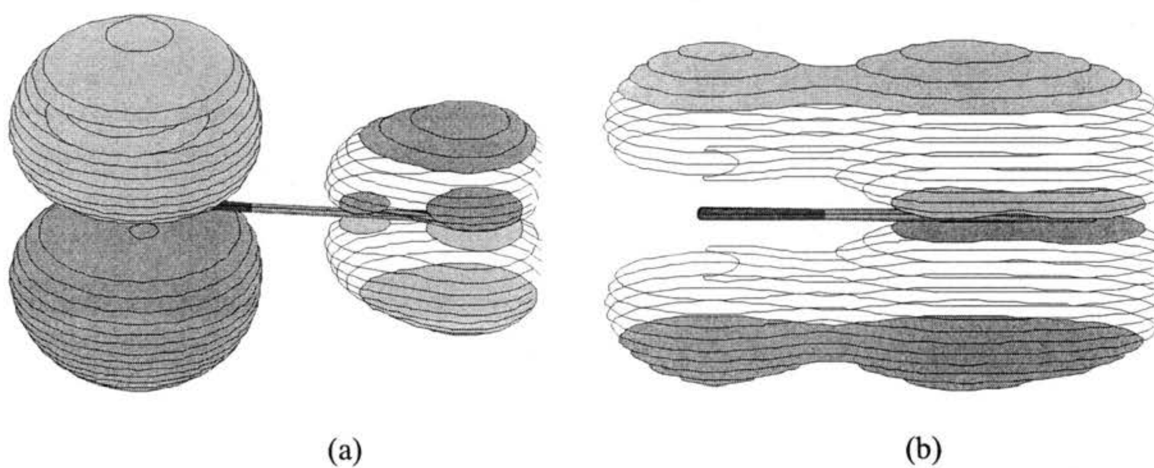

Figure II-1. Interaction between the lone electron pair of a halogen atom and the π-system of CN-bond: (a) Out-of-phase combination (b) In-phase combination.

the Fermi energy. Finally, the 3σ orbital due to the lone pair on the halogen gives rise to a photoelectron peak at 9.7 ± 0.4 eV.

B. Experimental part

B.1. XPS, UPS and TPD techniques

XPS, UPS and TPD experiments were conducted using a load-lock chamber coupled to a surface analysis instrument via a transfer system based on two O-ring seals. The pumping of the seals was provided with the help of a 70 L/s turbo-molecular pump (TMP). 300 L/s TMP was utilized to pump the load-lock chamber and also to initially evacuate the analytical UHV chamber. In the latter, the high vacuum at $2x10^{-10}$ Torr was maintained by using a 330 L/s ion pump, backed by a titanium sublimation pump. The pressure in the main chamber was measured by a nude ionization gauge.

For XPS experiments the Mg anode of a PHI 300W twin anode X-ray source was utilized. Detection of photoelectrons was performed by a PHI double-pass cylindrical mirror analyzer (CMA) with the pass energy equal to 50 eV. UPS spectra were obtained by a differentially pumped He discharge ultra-violet source from UG Microtech. In the latter case the pass energy of CMA was set equal to 5 eV. The Fermi level reference was obtained by taking UPS spectra of a copper foil. For TPD experiments, a 0-300 amu quadropole mass spectrometer was used for gas phase species characterization and product detection. The Si(100) surface was exposed to ICN with the sample positioned in front of the CMA and then moved to a position normal to the mass spectrometer. This process allows a direct comparison between the exposure data taken with XPS and UPS and the TPD experiments. The TPD experiments were performed with a heating rate of

2 K/s. Due to the high mass of ICN^+, the mass spectrometer was fixed at 76.5 amu in order to monitor the doubly ionized ICN^{2+} species.

B.2. Reagents and materials

Arsenic doped silicon (100) wafers were purchased from Virginia Semiconductor and cleaved into samples with the width 6 mm and length 16 mm. The thickness was equal to 0.5 mm. For TPD experiment samples with a slightly shorter length were employed in order to ensure uniform heating during the temperature ramp. The samples were mounted on the UHV manipulator using tantalum foil, tungsten spacers and molybdenum clamps to prevent the thermal stress in the sample. Hydrochloric acid was used to eliminate all traces of nickel impurities[84] and then the thermocouple was attached to the sample using the method described by Nishino *et al.*[85] Before each experiment the silicon samples underwent cleaning by repeating flashing to temperatures greater than 1400 K. This procedure was repeated until no impurities were detected by XPS. All exposures are reported in langmuirs (1 L=10^{-6} Torr/s). The typical background pressure during exposures was equal to about 10^{-7} Torr.

ICN was synthesized using a method described in the literature.[86] Briefly, ICN was formed by a complex aqueous reaction between sodium cyanide and iodine at 273 K according to the equation:

$$I_2 + NaCN \rightarrow ICN + NaI \qquad (2.1)$$

The products from this reaction were extracted by diethyl ether. The ether was removed and the resulting extract was mixed with water at 320 K. This mixture was heated in water under a mild vacuum and finally filtered to yield a crude product. The

crude product was purified by recrystallization in chloroform to yield large needle-like crystals. The final product is more than 99.5% pure by elemental analyses. Typical dosing arrangements for ICN resulted in unacceptable levels of oxygen and nitrogen contaminations due to its low vapor pressure at 298 K. To avoid oxygen and nitrogen contaminations, the compound was placed in small UHV compatible container attached to a precision leak value mounted on the load-lock chamber. Dry ice/acetone mixture was used to cool the sample during repeated freeze-thaw-pump cycles. The pump cycle reduces the pressure in the ICN container to 10^{-7} torr by employing the turbo molecular pump in the load-lock chamber. During dosing, the ICN container was heated to approximately 330 K to increase the vapor pressure. The ICN pressure measurements were made using an uncorrected nude ionization gauge.

Mass spectroscopy confirmed the presence of ICN^+ at 153 amu. Due to the deceasing transmission of the quadrupole mass spectrometer with mass, ICN^{2+} was more easily measured at 76.5 amu. In addition, CN^+, I^+ and I^{2+} species were detected. By mass spectroscopy, chloroform was the major impurity with peaks at 83 and 85 amu. However, chloroform was a trace impurity as no evidence of any chlorinated species was found by XPS after large exposures (20 ML or more) of ICN to the silicon surface at 100 K. This result is consistent to what has been previously found for both in the gas phase and on the surface in a study of ICN adsorption on Ni(100).[87]

BrCN was obtained from Aldrich chemical company. Contact between BrCN and the stainless steel container was avoided by first placing a small quantity in a quartz tube which was in turn slipped into the container. Even with these precautions, cyanogen was found to be slowly formed in the container as a precedent contaminant. Fortunately, the

cyanogen could be removed before each experiment by additional repeated freeze-pump-thaw cycles. ClCN was synthesized by using standard inorganic techniques.[88] Cl_2 gas was bubbled through a tetrachloromethane solution of sodium cyanide with a trace amount of acetic acid at temperatures between -10 and -5°C. After the solution turned green, the flowing Cl_2 gas was replaced by He, and the solution was slowly heated to 60°C. The resulting gas-phase reaction products were collected in a dry ice/acetone cooled flask. Excess Cl_2 gas was removed from the final reaction product by repeated freeze-pump-thaw cycles. In the collected product 1,3,5-trichlorotriazine is found to be a major contaminant. This species was eliminated by cooling the flask down to -5°C in a water/salt bath. The pure gas-phase ClCN was collected in a dry ice/acetone cooled receiving flask.

C. Results and discussion

C.1. XPS study

C.1.1. At low temperature

Figure II-2 shows the carbon and nitrogen 1*s* XPS spectra as a function of molecular ICN exposure to Si(100) at 100 K. After an initial 0.2 L exposure, the C 1*s* and N 1*s* photoelectron peaks are located at 285 and 399 eV, respectively. These binding energies agree favorably with previous XPS studies of intact CN species adsorbed on various surfaces. In CN_x films prepared by low-power inductively coupled plasma-activated transport reactions from a solid carbon source, XPS studies by Popov *et al.*[89] attribute a C 1*s* photoelectron peak at 285.9 eV and N 1*s* peak at 398.4 eV to the presence of nitrile group (C≡N) in the carbon nitride film. In another study, Hammer *et al.*[90] also

assign a N 1*s* photoelectron peak at 398.4 eV to the presence of a nitrile group. In addition to CN species found in CN_x films, adsorbed intact CN species can be prepared on Rh(110) by a 20 L C_2N_2 exposure at 100 K followed by a 373 K annealing treatment.[91] The XPS spectrum of this CN covered Rh(110) surface shows C 1*s* and N 1*s* photoelectron peaks corresponding to adsorbed CN groups at 284.3 and 397.4 eV, respectively.

Figure II-2 shows that after a 0.6 L molecular ICN exposure to Si(100) at 100 K the XPS photoelectron peak intensities increase but the peak shape remains similar to that found after a 0.2 L exposure. With ICN exposures greater then 0.6 L, the intensities of the C 1*s* and N 1*s* photoelectron peaks increase due to the formation of a molecular ICN multilayer film on the Si(100) surface. In addition, the peak positions shift slightly (less than 1 eV) to higher binding energies. As the coverage is increased further to 20 L (not shown in Figure II-2), a thick multilayer molecular ICN film is formed and the intensity of the Si peak almost vanished due to the attenuation of the photoelectrons by the thick film. The C 1*s* and N 1*s* photoelectron peaks after 0.2 L and 0.6 L exposures appear to be slightly broader and have a tail towards higher binding energies when compared to the peaks measured after multilayer ICN exposures. The C 1*s* and N 1*s* XPS photoelectron spectra as a function of BrCN exposure to Si(100) surfaces at 100 K are shown in Figure II-3. The C 1*s* photoelectron peak after a 0.3 L BrCN exposure is slightly broader and skewed toward higher binding energy. Like the ICN adsorption model, the BrCN C 1*s* peak can be fit using two Gaussian components. One component is assigned to a molecular species at 286.5 eV and the other to a dissociated species at 284.5 eV. The peak position of the dissociated species is justified by the room temperature XPS and

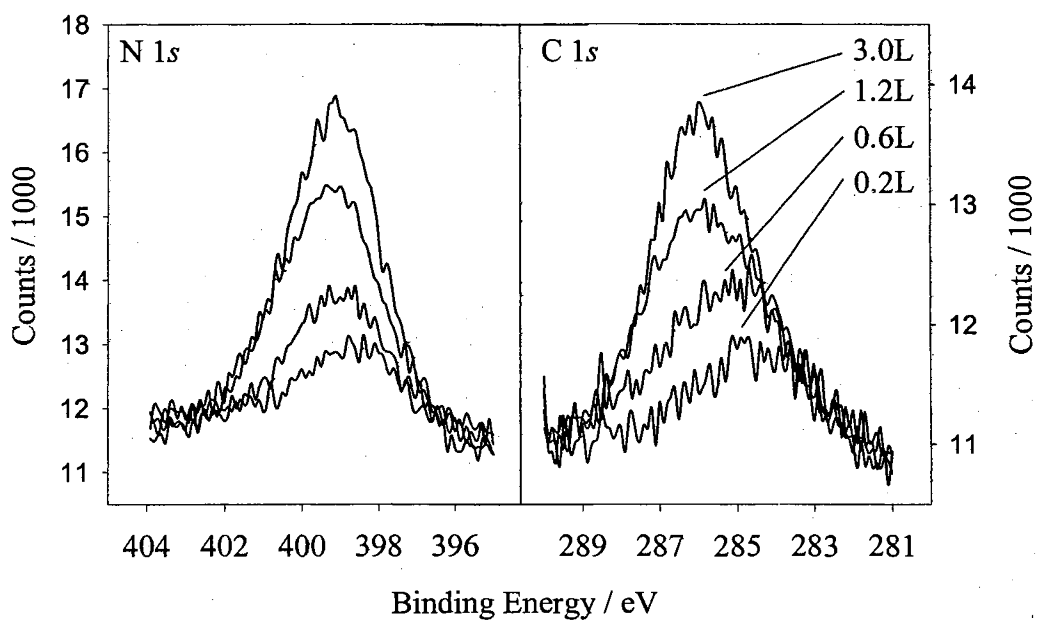

Figure II-2. Nitrogen and carbon 1*s* XPS spectra as a function of ICN exposure to the Si(100) surface at 100 K. The XPS intensities are relative. Adapted from Ref. 75.

UPS results discussed below. The analysis indicates that about 60 % is adsorbed molecularly (286.5 eV) following a 0.3 L BrCN exposure with the remaining 40 % adsorbed as atomic Br and CN groups (284.5 eV). The 60 % adsorbed molecularly is much greater than the 25 % found for low ICN exposures to Si(100) at 100 K and can be attributed to the stronger Br-CN bond energy.[92]

As the exposure is further increased to 0.9 L, Figure II-3 also shows a simultaneous intensity increase of the C 1*s* and N 1*s* photoelectron peaks with increasing BrCN exposures. Both the C 1*s* and N 1*s* peaks become more symmetrical and their peak positions shift slightly upward in energy, approaching a constant with the highest exposures. No shift with increasing BrCN exposures is observed for the Si 2*p* photoelectron peak. With increasing exposures of molecular BrCN to the Si(100) surface at 100 K, an increasingly thick molecular BrCN film with a C 1*s* binding energy of 286.5 eV is formed. However, a simple adsorption model in which the BrCN first adsorbs as a dissociated species followed by molecular adsorption can be ruled out. The concentration of the dissociated species continually increases until an exposure of approximately 1.2 L is reached.

Figure II-4 shows the C 1*s* and N 1*s* XPS spectra as a function of ClCN exposure to the Si(100) surface at 100 K. With increasing ClCN exposures to Si(100), a simultaneous increase in intensity for both the C 1*s* and N 1*s* photoelectron peaks is observed. For the C 1*s* peak, a second peak clearly grows in at 289.2 eV with increasing exposure at 100 K. As in the case of BrCN and ICN, these results indicate that a molecular film forms with increasing ClCN exposures. The C 1*s* binding energy for ClCN in the film is 289.2 eV, higher than that for both BrCN and ICN. Table II-1

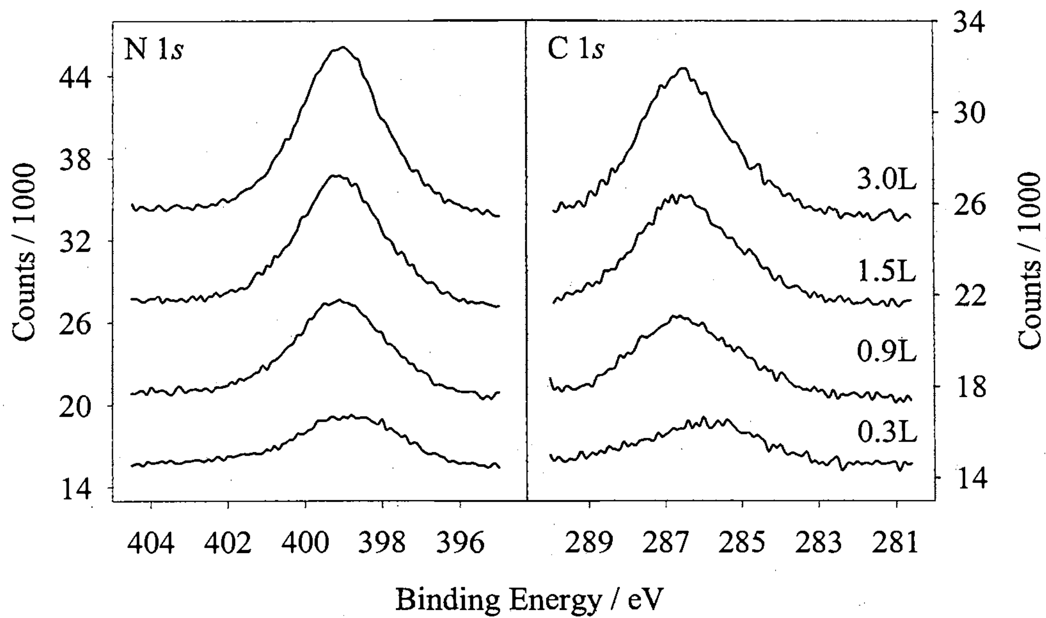

Figure II-3. Nitrogen and carbon 1*s* XPS spectra as a function of BrCN exposure to the Si(100) surface at 100 K. The XPS intensities are relative. Adapted from Ref. 76.

summarizes the measured binding energy for the C 1*s* photoelectron peak of molecularly adsorbed ICN, BrCN and ClCN. As expected, the increasing electronegativity of the halogens from I to Cl results in an upward shift in the binding energy of the C 1*s* the photoelectron peak.

Compared to the analogous experiments for ICN and BrCN, the uptake rate is significantly smaller for ClCN. Visual examination of the 3 L exposures for BrCN (Figure II-3) and ClCN (Figure II-4) clearly shows the dramatic difference in the uptake. For BrCN, the multilayer film is clearly formed, while for ClCN, the multilayer peak is clearly much smaller in relationship to the peak due to the dissociated species. Unlike ICN and BrCN, ClCN is prepared as a gas at a pressure greater than 760 Torr. In addition, the boiling point of ClCN is 13.8°C while for ICN and BrCN are 146 and 61°C, respectively.[86,88] Thus, possible undetected contributions to the measured pressure during ClCN dosing, but not ICN or BrCN, are unlikely. In addition, differences in the ionization cross sections between these analogous compounds are unlikely to cause such a dramatic difference in the uptake. The most probable explanation is that the sticking coefficient for ClCN is significantly smaller than that for ICN and BrCN.

As in the case of BrCN, the C 1*s* photoelectron peak for a 0.6 L molecular ClCN exposure to Si(100) is slightly broader than that measured for higher exposures. This low exposure peak possesses a tail towards higher binding energy similar to that found for BrCN and ICN. Using an analysis similar to that utilized for BrCN, nearly 40 % of ClCN is found to be adsorbed molecularly (289.2 eV), while the remaining 60 % dissociates upon adsorption to form atomic Cl and CN groups (284.5 eV) after a 0.6 L exposure of ClCN to Si(100) at 100 K. As in the case of BrCN, this peak position for the dissociated

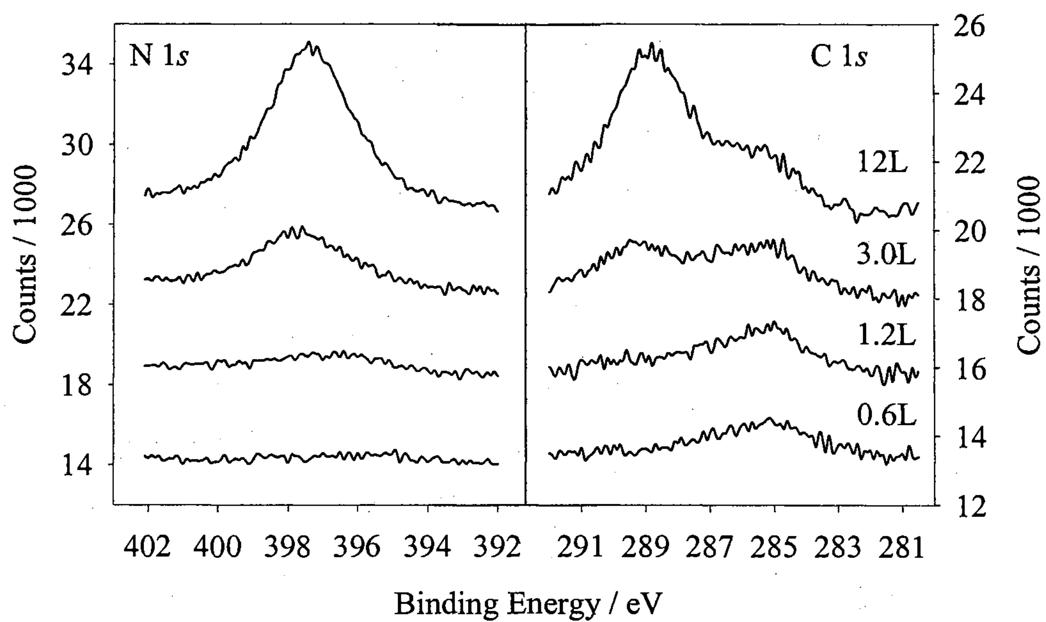

Figure II-4. Nitrogen and carbon 1*s* XPS spectra as a function of ClCN exposure to the Si(100) surface at 100 K. The XPS intensities are relative. Adapted from Ref. 76.

Table II-1. *The XPS C 1s peak position after a saturation exposure of ICN, BrCN and ClCN on Si(100) surfaces at low (100 K) and room (300 K) temperatures.*

	Low temperature	Room temperature
ICN	285.5 eV	284.5 eV
BrCN	286.5 eV	284.5 eV
ClCN	289.2 eV	284.5 eV

species is justified by the room temperature results discussed below. Although the Cl-CN bond strength is stronger than the Br-CN bond,[92] approximately 20 % more ClCN adsorbs dissociatively than BrCN after low exposures to Si(100). This contradicts the bond-energy trend inferred from the BrCN and ICN results. One likely explanation is that the low sticking probability of molecular ClCN with respect to ICN and BrCN results in the disproportional buildup of the dissociated species. However, the concentration of the dissociated species continues to increase as the molecular species starts to build in. Thus, ClCN is similar to BrCN in that ClCN does not saturate the dissociated state before molecular adsorption occurs.

The chemical state of the adsorbed I gives additional information about the ICN adsorption. At ICN exposures of 0.2 and 0.6 L, the iodine 4*d* photoelectron peak (Figure II-5(a)) is centered at 50 eV and also shows a tail to higher binding energies. Although the spin-orbit splitting is not resolved, the XPS spectra are similar to the high-resolution soft XPS spectra in Ref. 93. With increasing molecular ICN exposure at 100 K, an upward shift in the I 4*d* binding energy is observed. In addition, increasing exposures

results in a continuous increase in the relative amount of molecular ICN with respect to the dissociated ICN species. One explanation for the high energy tail observed in the C 1*s* and I 4*d* XPS spectra after the low temperature 0.2 and 0.6 L ICN exposures is the presence of molecular ICN clusters in addition to dissociated ICN. Thus at low temperatures, ICN adsorption results in partial dissociation to form molecular ICN, atomic I and CN functional groups on the Si(100) surface. Further exposures at low temperatures result in a multilayer molecular film. An analysis of the C 1*s* XPS spectra measured after an ICN exposure of 0.2 L suggests that approximately 75 % of the ICN molecules dissociate. The non-dissociated ICN species are likely adsorbed on the Si(100) surface via a dative bond between the nitrogen and the Si-dimers.[18] Although molecular ICN was not observed at low exposures, Marshall and Jones observe that ICN dissociates on Ni(111) at low temperatures followed by multilayer adsorption of ICN at higher exposures.[87] For BrCN exposures of 0.3 L to Si(100) at 100 K, the Br 3*d* photoelectron peak (Figure II-5(b)) is centered at 70 eV with a tail towards higher binding energies.

In addition, for exposures sufficient to form a multilayer, the Br 3*d* peak is found at higher binding energies (72 eV). Consistent with the ICN C 1*s* photoelectron studies, the high energy tail observed in the Br 3*d* spectrum for submonolayer BrCN exposures to Si(100) at 100 K supports an analogous adsorption model with both molecular BrCN and dissociated BrCN present on the surface. This conclusion is also consistent with the BrCN C 1*s* photoelectron results discussed above. The Cl 2*p* XPS spectrum shown in Figure II-5c contains an analogous trend in peak positions and widths. For a 0.6 L exposure of ClCN at 100 K (Figure II-5(c)), the Cl 2*p* photoelectron peak is observed at

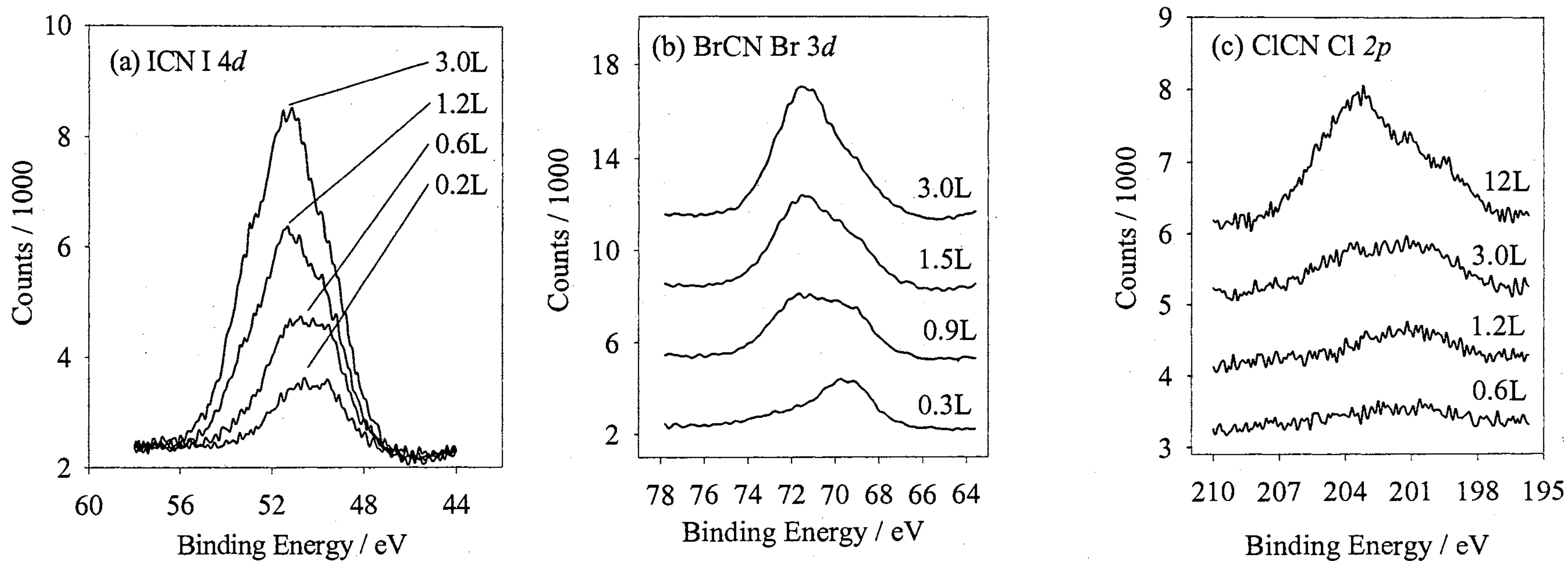

Figure II-5. Si(100) XPS spectra for the (a) iodine 4*d*, (b) bromine 3*d* and (c) chlorine 2*p* peak as a function of the respective cyanogen halide exposure at 100 K. The XPS intensities are relative. Adapted from Refs. 75,76.

200 eV with a tail towards higher binding energy. For large exposures (33 L), multilayers of ClCN are formed and the Cl 2*p* peak is shifted upwards to 203 eV. Along with the ClCN C 1*s* information, these results also support the adsorption model found for ICN and BrCN, with ClCN adsorbed both molecularly and as atomic Cl and CN at low exposures and temperatures on Si(100).

The low temperature adsorption of ICN, BrCN and ClCN is simpler than that found for HCN on Si(100). When high resolution electron energy loss spectroscopy is performed after low HCN exposures at 100 K, the resulting spectra are complex due to contributions from HCN, HCNH and CN species along with HCN dimers.[66] At larger exposures and lower temperatures, HCN dimers and possibly polymers become the dominant species on the Si(100) surface. In contrast, the low temperature cyanogen halide chemistry is simpler, with only molecular and one dissociated species adsorbed on the Si(100) surface.

The driving force for the formation of this dissociated species is the replacement of the XC bond with stronger XSi and CSi bonds.[94] The resulting CSi and CN bonds are stronger than an XC or an XN bond. The XC bond in XCN is stronger than the typical XC bond due to overlap between the *p* orbital on the halide and the π-system on the CN group.[92] However, for possible adsorption geometries where this overlap is not possible, the XSi bond is slightly stronger than the XC bond.[94] Thus, a side-on adsorption geometry for XCN where the CN group adds across the Si dimer bond is not energetically favorable compared to the observed dissociated species. In contrast for HCN, the formation of a side-on adsorbed HCNH species is possible due to the formation of stronger HC and HN bonds with respect to the HSi bond. Intermediates to this species

can react with other adsorbed HCN molecules leading to dimerization or polymerization on the Si(100) surface. Consistent with these ideas, the C_2N_2 molecule adsorbs molecularly on the Si(100) surface at low temperatures due to the stronger C-C bond and the lack of surface H.[53] The exclusive molecular adsorption of the aromatic $(HCN)_3$ species can also be rationalized by the strong intramolecular bonds.[41]

C.1.2. At room temperature

Following an exposure of ICN, BrCN or ClCN to the Si(100) surface at room temperature, the resulting C 1*s* and N 1*s* photoelectron peaks are nearly Gaussian in shape and are centered at approximately 284.5 and 398 eV, respectively. Figures II-6(a)-(c) show the C 1*s* photoelectron spectrum for XCN (X=I, Br or Cl) as a function of exposure to Si(100) at room temperature. This C 1*s* peak position is consistent with other XPS studies of intact CN species adsorbed on various surfaces.[89-91] Based on these observations, cyanogen halides dissociatively adsorb on Si(100) at room temperature to form an adsorbed halide and an intact CN functional group. The identification of the 284.5 eV C 1*s* photoelectron peak in the room temperature spectra justifies the assignment of the lower binding energy component in the low temperature XPS analysis of ICN, BrCN and ClCN C 1*s* photoelectron peak to a dissociated species. After approximately a 0.2 L ICN and BrCN exposure or a 0.6 L ClCN exposure, Figure II-6(a)-(c) shows that the C 1*s* photoelectron peak position and intensity are unchanging with further exposures of the respective cyanogen halide. Therefore, room temperature exposure of XCN to Si(100) results in a saturated layer containing the atomic halide species and intact CN functional groups. For this layer, the ratio of the number of carbon

atoms to nitrogen is found to be approximately 1. This ratio is computed, taking into account the atomic sensitivity factors,[95] from the integrating area ratio of the C 1*s* to the N 1*s* photoelectron peak. Thus, XCN dissociatively adsorb on Si(100) at room temperature to form an adsorbed halide and a CN functional group.

The I 4*d*, Br 3*d* and Cl 2*p* photoelectron peaks for ICN, BrCN and ClCN, respectively, support the above room temperature adsorption model. Consistent with C 1*s* and N 1*s* spectra, the I 4*d* photoelectron spectra resulting from RT absorption of ICN are similar to the spectra taken at low temperature without the high energy tail. The lack of the high energy tail seen in the RT adsorption experiments indicates that only atomic iodine is adsorbed on the Si surface. In addition, intensity and binding energy of the I 4*d* photoelectron peak is constant with increasing molecular ICN exposures. The XPS spectra of the BrCN exposed Si(100) surface at room temperature show a Br 3*d* photoelectron peak at 69 eV. Consistent with the above adsorption model and in contrast with the low temperature adsorption results for BrCN, the room temperature Br 3*d* peak lacks the high energy tail previously attributed to molecularly adsorbed BrCN. A similar absence of a high energy tail is also found for the Cl 2*p* photoelectron peak at 200 eV for room temperature ClCN exposed Si(100). Again, this result is consistent with the above adsorption model and is in contrast with the low temperature adsorption results for ClCN. In conclusion, at room temperature ICN is adsorbed as atomic I and CN groups, BrCN is adsorbed as atomic Br and CN groups, and ClCN as atomic Cl and CN groups.

C.1.3. At higher temperatures

Figures II-7 – II-9 present the XPS spectra of the C 1*s* and N 1*s* photoelectron

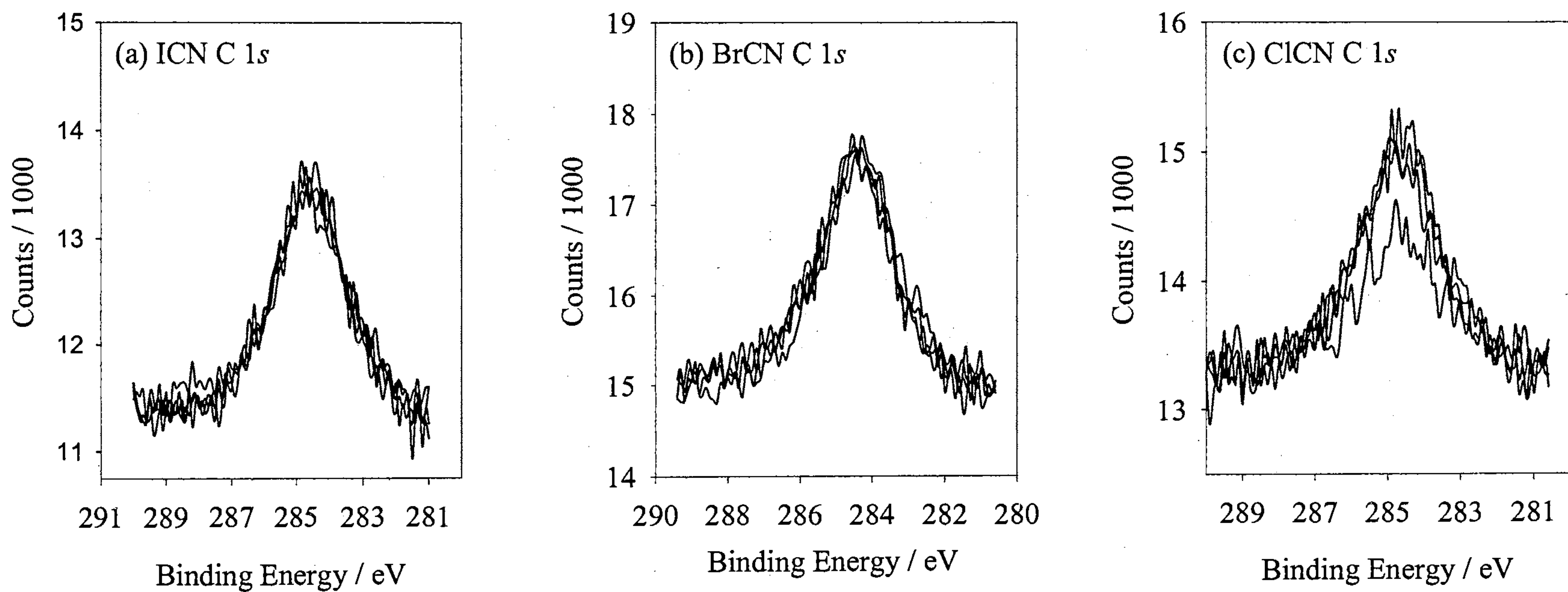

Figure II-6. Carbon 1*s* XPS spectra as a function of (a) 0.2 L to 20 L ICN, (b) 0.3 L to 42 L BrCN and (c) 0.3 L to 33 L ClCN exposures to the Si(100) surface at 300 K. The XPS intensities are relative. Adapted from Refs. 75,76.

peaks for surfaces prepared by room temperature saturation exposures of ICN, BrCN and ClCN, respectively, and subsequently annealed for one minute at indicated temperatures. When the saturated surface is annealed to 473 K, the C 1*s* and N 1*s* photoelectron peaks start to broaden and shift slightly towards lower binding energies. This shift in binding energy is attributed to the increasing presence of atomic C and N surface species formed from partial decomposition of the surface CN groups. The initial decomposition of the CN groups at 473 K is similar to that found for other systems.[67] As the annealing temperature is further increased, the C 1*s* and N 1*s* peaks continue to broaden and shift towards lower energies as the concentration of adsorbed atomic C and N species increases with the simultaneous decrease in the concentration of adsorbed CN. Finally at around 873 K, the C 1*s* and N 1*s* peaks indicate only the atomic species with binding energies of 283 and 398 eV, respectively, remaining on the Si(100) surface. At this temperature, all surface CN species are decomposed into Si-C and Si-N species.

The decomposition temperature of the adsorbed CN species on the Si(100) surface is similar to that found for other C and N containing compounds on the Si(100) surface.[16] The CN surface bonds created by HCN adsorption on Si(100) decompose between 600 and 800 K.[66] The C_2N_2 and $(HCN)_3$ molecules also decompose in the same temperature range.[41,53] In addition to silicon surfaces, for CN adlayers on Rh(110), Bondino *et al.*[91] observe partial decomposition of the adlayer around 450 K.

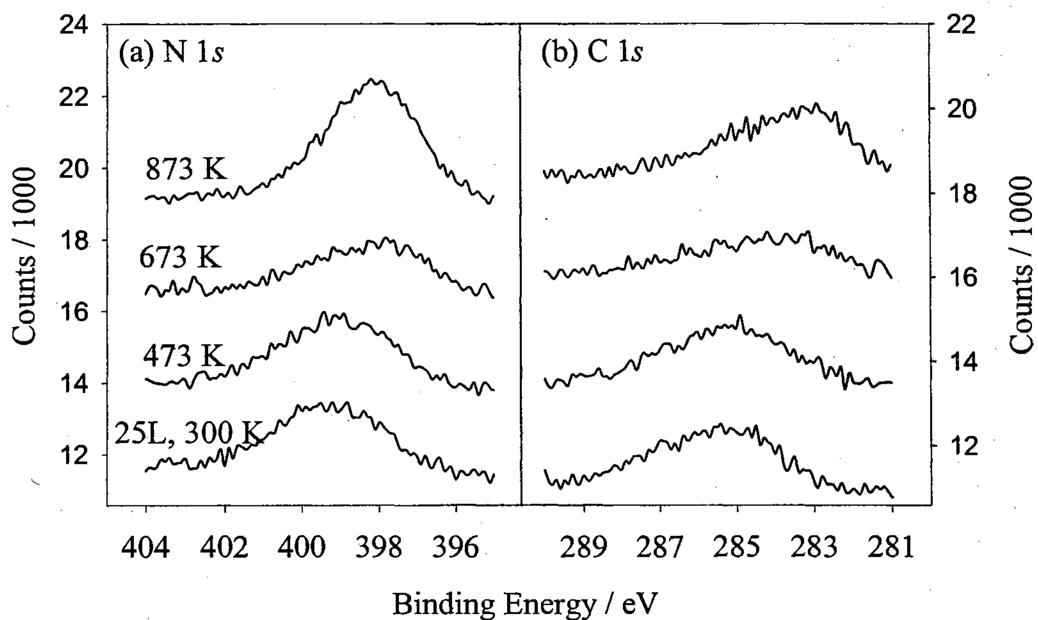

Figure II-7. Nitrogen and carbon 1*s* XPS spectra from a Si(100) surface initially exposed to 25 L of molecular ICN at 100 K and annealed to various temperatures for 1 minute. The XPS intensities are relative. Adapted from Ref. 75.

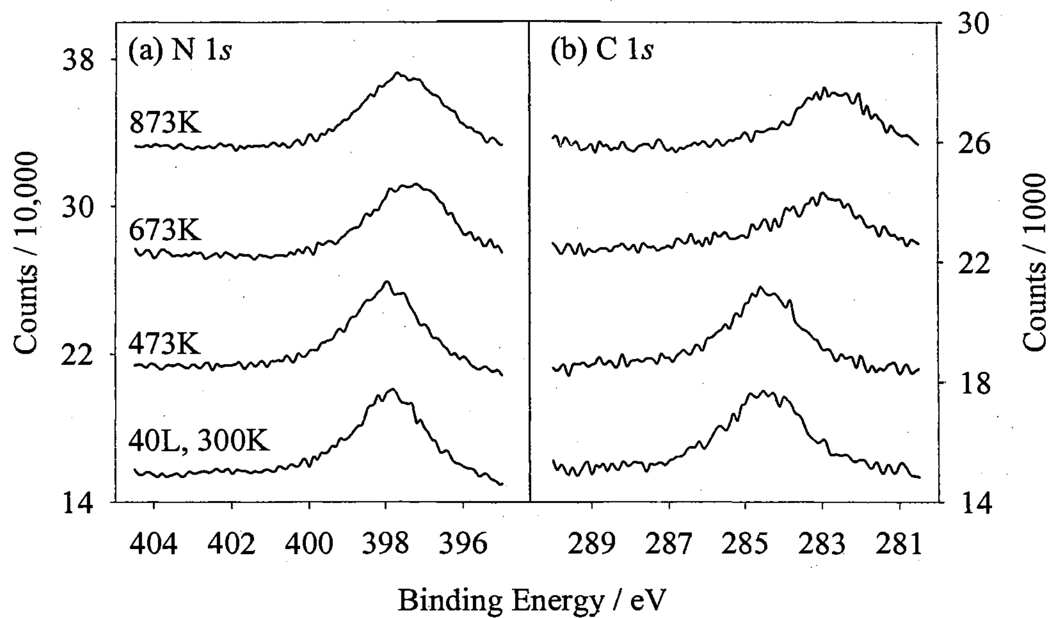

Figure II-8. Nitrogen and carbon 1*s* XPS spectra from a Si(100) surface initially exposed to 40 L of molecular BrCN at 300 K and annealed to various temperatures for 1 minute. The XPS intensities are relative. Adapted from Ref. 76.

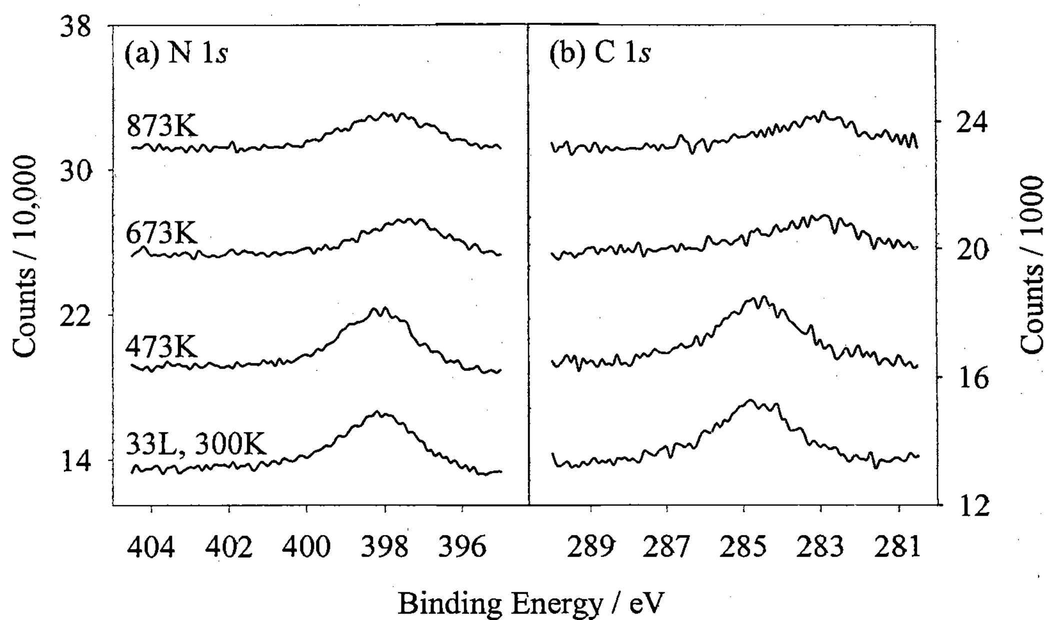

Figure II-9. Nitrogen and carbon 1*s* XPS spectra from a Si(100) surface initially exposed to 33 L of molecular ClCN at 300 K and annealed to various temperatures for 1 minute. The XPS intensities are relative. Adapted from Ref. 76.

C.2. UPS study.

C.2.1. At low temperature

The UPS spectra as a function of ICN, BrCN and ClCN exposure to the Si(100) surface at low temperature are shown in Figures II-10(a)-(c). For ICN the peak (Fig. II-10(a)) with the lowest binding energy at 4.4 ± 0.4 eV with respect to the Fermi energy is assigned to the 2π molecular orbital. A similar transition at 4.8 eV is seen by Marshall and Jones for multilayer films of ICN on the Ni(111) surface.[87] At higher binding energies, a peak at 6.7 ± 0.4 eV contains contributions from the spin-orbit split 1π and the 4σ molecular orbitals. For ICN on the Ni(111) surface, a similar peak at 7.1 eV is also observed. Given that the surface broadened widths of the UPS peaks are greater than 1 eV, there is very good agreement between these two photoelectron peaks for multilayer ICN films on Si(100) and Ni(100) surfaces. Finally, the UPS peak at 9.7 ± 0.4 eV is assigned to the 3σ molecular orbital of the adsorbed molecular ICN.

For BrCN exposures between 0.3 and 0.6 L, the BrCN UPS spectra look similar to that at high exposures (Fig. II-10(b)). Although features from molecular BrCN after a 0.3 L exposure are visible, there is both a shoulder toward lower energy and considerable intensity between the molecular BrCN peaks (5.3 and 7.7 eV). The XPS studies have shown that at low exposure and temperature a fraction of the BrCN is adsorbed as atomic Br and CN. For CN generated from room temperature adsorption of ICN, a single photoelectron peak at 6.0 eV is visible. Thus, CN generated from BrCN adsorption should appear between the two lowest energy molecular BrCN peaks (5.3 and 7.7 eV). The additional broadening to lower binding energies (5.3 eV) is due to a contribution of atomic Br at 5.0 eV. To confirm this assignment, the Si(100) surface was exposed to

molecular Br_2 at room temperature. The UPS spectrum of this system contains a feature at 5.0 eV, which is assigned to the presence of atomic Br on the surface. Similar UPS transition energies are reported for Br on other surfaces. For Br adsorbed on Cu(111), Jones and Kadodwala[96] attribute an UPS peak at 4.7 eV to a state of majority Br character. On the Ag(110) surfaces, Kruger and Benndorf[97] identify a peak at 5.2 eV due to chemisorbed Br.

The UPS spectra as a function of ClCN exposure to the Si(100) surface at low temperature are shown in Figure II-10(c). An interpretation similar to ICN and BrCN can be applied to the high exposure ClCN UPS spectra. For a 33 L ClCN exposure, the spectrum of the resulting multilayer film is shifted and broadened with respect to lower exposures. The 3 L ClCN exposure spectrum is better resolved. This spectrum contains four peaks at 6.5, 8, 9.5 and 13 eV. Using the UPS spectra of gaseous ClCN as a reference,[79,82] the peak at 6.5 eV can be assigned to the out-of-phase (2π) combination, the 8 eV transition to the nitrogen lone pair (4σ), and the 9.5 eV transition to the in-phase (1π) combination. The 13 eV transition is assigned to the 3σ MO of the adsorbed molecular ClCN.

The UPS spectra following low ClCN exposures to the Si(100) surface at low temperature are more complex than those of BrCN and ICN. For a 0.3 L ClCN exposure, the spectrum (Figure II-10(c)) contains a single peak around 5 eV due to the presence of chlorine from ClCN dissociation. At 0.3 L, no discernable concentration of CN functional groups is detected by XPS. Due to the higher sensitivity of the Cl 2*p* peak, a very small amount of atomic Cl is detected on the surface. In addition, UPS is found to be very sensitive to atomic Cl. These results indicate that no molecular ClCN is present and that

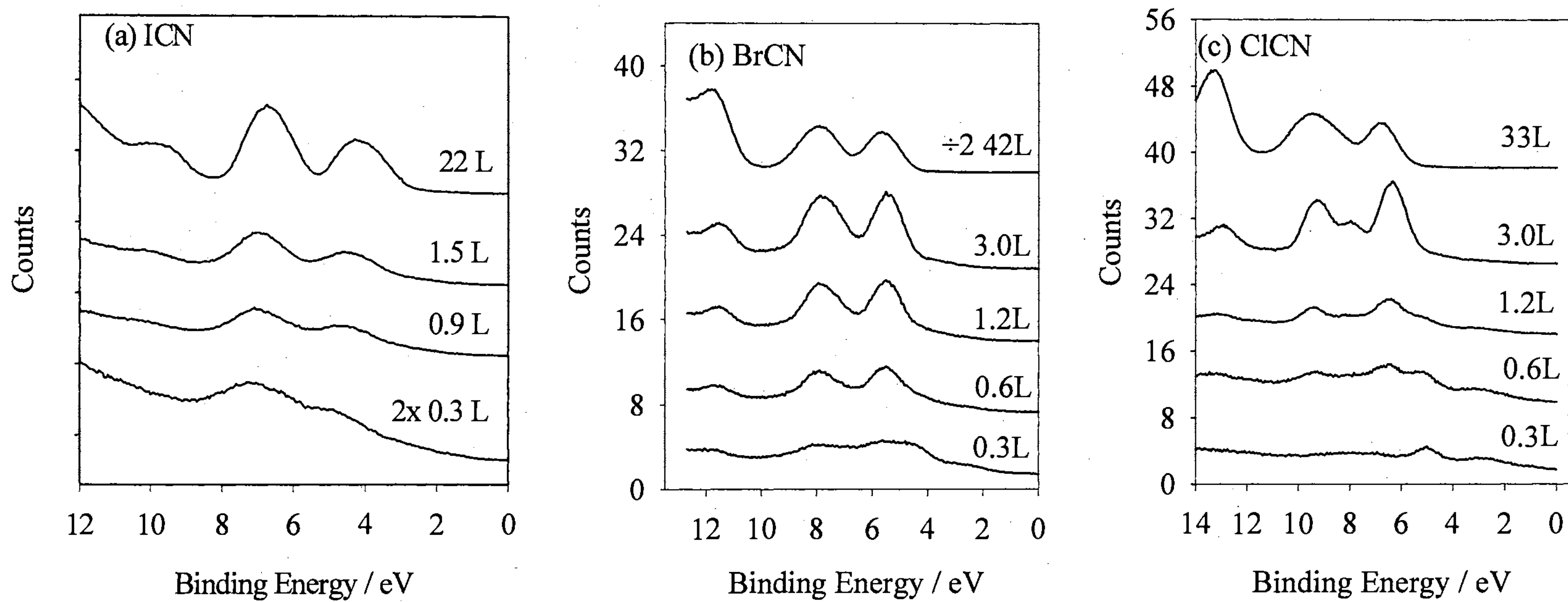

Figure II-10. He(I) UPS spectra of Si(100) after various exposures to (a) ICN, (b) BrCN and (c) ClCN at 100 K. The UPS intensities are relative. Adapted from Refs. 75,76.

Cl is formed by the dissociation of a trace amount of ClCN. This conclusion is also consistent with the low ClCN sticking probability with respect to BrCN and ICN found by the XPS experiment. After 0.6 L ClCN exposures, the UPS spectrum contains two additional peaks at 6.5 and 9.5 eV. These transitions are assigned to the out-of-phase (2π) and in-phase (1π) combinations, respectively. However, XPS results also indicate the presence of CN groups on the surface, which have a transition at 6.0 eV. Thus, the 6.5 eV peak also contains a decreasing contribution due to the surface CN groups with increasing exposures. This contribution explains the varying intensity of the 6.5 eV transition with respect to the 9.5 eV peak. The 4σ molecular orbital is not clearly seen for exposures less than 3 L. However, at lower exposures, it contributes to the almost featureless intensity between 6.5 and 9.5 eV.

C.2.2. At room temperature

The UPS spectra for the room temperature adsorption of ICN, BrCN and ClCN as a function of exposure are given in Figure II-11. In contrast to the low temperature adsorption (Figure II-10), the UPS spectra after room temperature adsorption contain only one peak due to the CN π system centered at 6 eV. The XPS results show the surface rapidly saturates at relatively low exposures. Unlike XPS, which regulated the power to the anode, the gas flow into the UPS source is not regulated and the photon flux can drift with time. Thus, the small increase in intensity of the larger exposures is attributed to a small drift in the photon flux. Since only one species exists on the surface, possible photochemistry reactions leading to an intensity increase is unlikely. A single peak is also observed after room temperature adsorption of ICN on Si(100) (Fig. II-11(a))

and is assigned to the degenerate π molecular orbitals on the CN groups. The UPS shows only a single peak from the now degenerate π molecular orbitals. After the dissociation of the I-CN bond, the π molecular orbitals are no longer split by the overlap between the atomic p orbital centered on the halogen with the CN π system. For BrCN and ClCN, the room temperature UPS results are consistent with the XPS data and support the room temperature adsorption model found for ICN. In this model, the cyanogen halides (XCN) dissociate to form atomic halogen (X) and intact CN species on the surface. However, in contrast to atomic I, adsorbed Br and Cl have discernable features in the UPS spectra. The UPS photoelectron peak at 5.0 eV resulting from atomic Br originating from the dissociation of BrCN on the surface imparts a shoulder towards the lower binding energy on the measured 6 eV peak due to surface CN groups (Fig. II-11(b)). The UPS spectrum obtained after a 50 L of Br_2 exposure to the Si(100) surface at 300 K contains a broad peak at around 5.5 eV. An examination of the UPS spectra taken after an exposure of ClCN to the Si(100) surface at room temperature (Fig. II-11(c)) reveals that the peak at 6.0 eV is also broader than expected and contains a visible shoulder toward high binding energies. In addition, a small feature is observed at approximately 3.0 eV. These additional fractures are due to the contribution from atomic Cl originating from ClCN dissociation. The UPS spectrum of a Si(100) surface after Cl chemisorbed at room temperature has been studied by a number of authors.[98,99] The resulting spectra are complex and contain many peaks between 3 and 9 eV. Although not as well resolved, a similar spectrum after a 32 L of Cl_2 exposure to the Si(100) surface at 300 K was obtained by our apparatus. Thus, the shoulder at 6.0 eV and the broad feature at approximately 3 eV are due to adsorbed Cl.

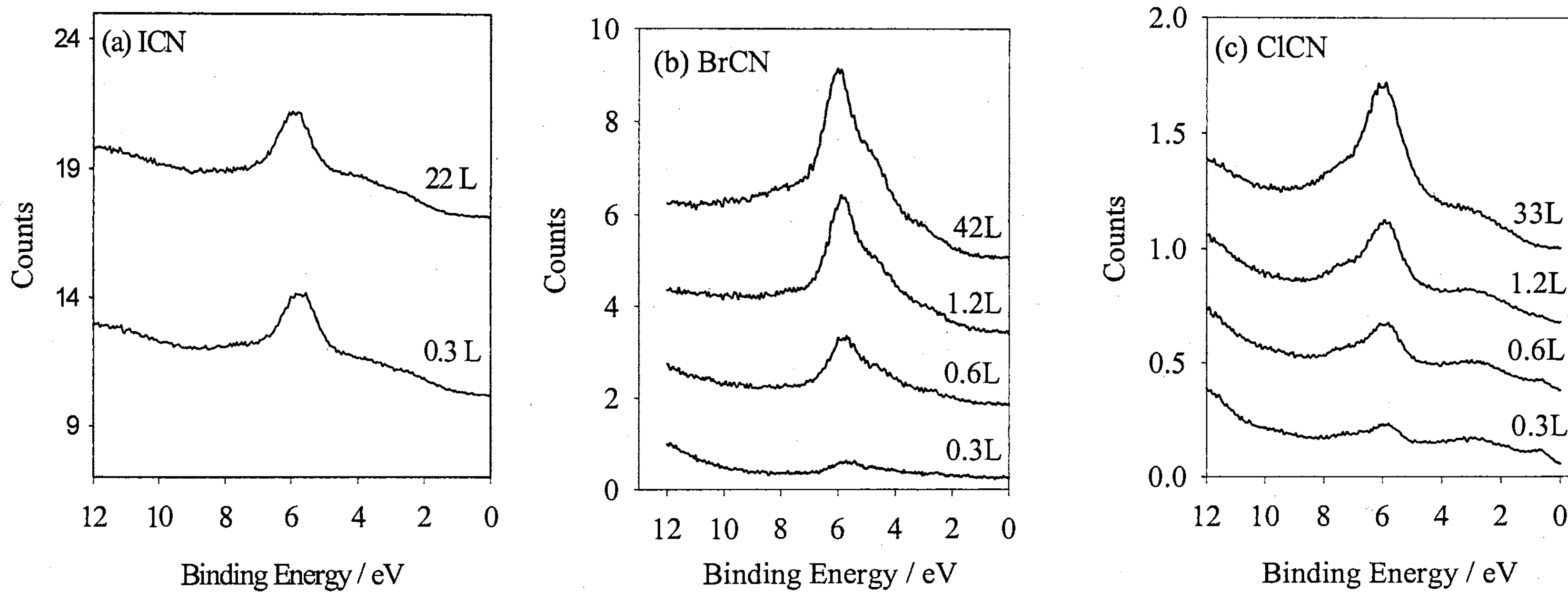

Figure II-11. He(I) UPS spectra for exposure of (a) ICN, (b) BrCN and (c) ClCN to the Si(100) surface at 300 K. The UPS intensities are relative. Adapted from Refs. 75,76.

C.2.3. At higher temperatures

At 273 K, the UPS spectra of XCN are identical to those obtained by room temperature adsorption. No further changes were observed in the UPS spectra with increasing annealing temperatures until 470 K. Concomitantly with the changes in the XPS spectra, the UPS peak at 6.0 eV starts to decrease in intensity at 470 K and disappears completely by 873 K, indicating complete decomposition of the surface CN groups. This observation further supports the assignment of the UPS transition at 6.0 eV to an adsorbed CN species on the Si(100) surface at room temperature. A similar temperature is found for complete decomposition of HCN and C_2N_2 on the Si(100) and Si(111) surfaces.[51,53,66] Moreover, complete decomposition of surface CN groups on the Rh(110) surface into adsorbed atomic C and N occurs at approximately 775 K.[91]

C.3. TPD study

Fig. II-12 shows the TPD spectra for ICN^{2+} (76.5 amu) generated by molecular ICN desorbing from the surface as a function of ICN exposure between 0.1 and 5 L to Si(100). Only one peak from ICN^{2+} at 170 K was observed. A small shoulder develops reproducibly at higher exposures. This shoulder appears only at very high exposures and is possibly due to ICN desorption from the metallic clips on sample holder. The ICN^{2+} peak in the mass spectrometer directly reflects the flux of molecular ICN that desorbed from the Si(100) surface. For a molecular ICN film grown on the Ni(111) surface, Marshall and Jones found that the film desorbed at around 173 K.[87] This desorption temperature corresponds well with the ICN^{2+} TPD peak shown in Figure II-12 for 5 L, an exposure, which is sufficient to form a molecular ICN film on the Si(100) surface. On

Ni(111) at low temperatures, ICN initially chemisorbs and forms adsorbed atomic I and CN as an intact functional group.[87] In contrast to the Ni(111) surface, the TPD spectra from the Si(100) surface for ICN exposures as low as 0.1 L still contain a peak at 170 K. Figure II-12 demonstrates that the desorption temperature remains essentially constant as the intensity of the 170 K peak grows with increasing ICN exposures. This result implies that for submonolayer exposures, some fraction of ICN is either weakly bonded to the surface with binding energies similar to that between ICN molecules or that ICN forms molecular clusters even at low exposures. The similarity between the Ni(111) and the Si(100) desorption temperatures for ICN supports the later model in which ICN clusters form at low exposures. In addition, the presence of intact ICN molecules on the Si(100) surface at low temperatures is supported by the XPS and UPS measurements. The only other desorption product detected after ionization in the mass spectrometer is I^+ at 650 K. In a separate experiment, this temperature is similar to that observed for a Si(100) surface exposed to molecular I_2. In addition, the measured desorption temperature corresponds to temperature found by Michel *et al.*[100] after molecular I_2 exposure to Si(100). These results show that the adsorbed I acts independently of the CN group on the Si(100) surface and is chemically similar to adsorbed iodine formed from I_2 adsorption. Another possible desorption product generated from the coupling of two surface CN groups is C_2N_2. However, this species was not observed in TPD experiments following a large initial ICN exposure at 100 K.

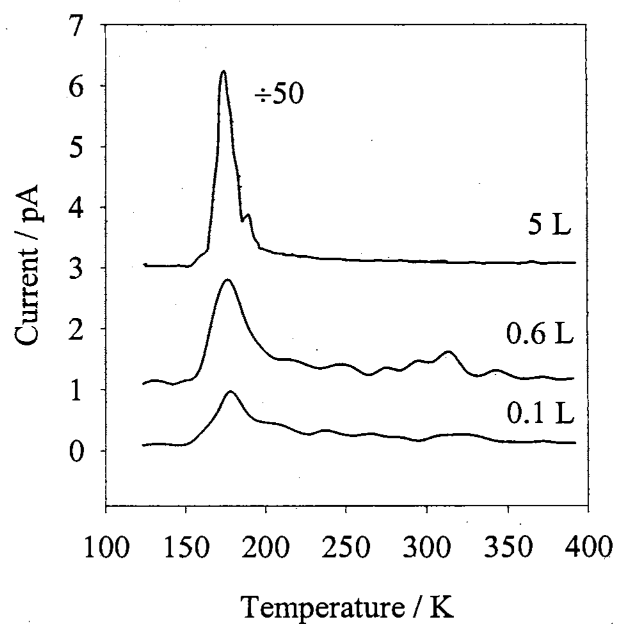

Figure II-12. TPD spectra of ICN^{2+} (76.5 amu) using a heating rate of 2 K/s. The initial ICN exposure at 100 K is varied between 0.1 and 5 L as noted. Adapted from Ref. 75.

D. Conclusions

The adsorption and decomposition of ICN, BrCN and ClCN on Si(100) were investigated utilizing XPS, UPS and TPD. For submonolayer exposures, XPS indicates that the CN triple bond remains intact upon adsorption at 100 K. The π electrons in the CN triple bond contribute to two peaks (4.4 and 6.7 eV for ICN, 5.3 and 7.7 eV for BrCN and 6.5 and 9.5 eV for ClCN) in the UPS spectrum. The splitting of the π system shows that some fraction adsorbs molecularly at low temperatures while the rest adsorbs in a dissociated state. XPS analyses of the C 1*s* photoelectron peak following submonolayer exposure at low temperatures suggest that molecular adsorption for BrCN is higher (60 %) than that of ClCN (40 %) and ICN (25%). The fraction of molecular BrCN is larger than the 25 % found for ICN adsorption on Si(100), possibly due to the stronger Br-CN bond. However, this possibility does not explain the large degree of dissociation found for low-temperature ClCN adsorption on Si(100) with respect to BrCN. It is proposed, based on the low temperature XPS uptake experiments, that molecular ClCN has a lower sticking probability with respect to ICN and BrCN, and that this lower sticking probability results in the disproportional buildup of the dissociated species. The dissociated species forms due to the relatively weak X-CN bond. Consistent with this idea, the C_2N_2 and aromatic $(HCN)_3$ molecules adsorb without dissociation on the Si(100) surface at low temperatures.[41,53] For low temperature HCN adsorption on Si(100), HCN, HCNH and CN species could be identified along with HCN dimers.[66] In contrast, the Si(100) surface after low temperature adsorption of BrCN and ClCN contains only the molecular and one dissociated species with an intact CN group on Si(100).

The C 1*s* and N 1*s* photoelectron peaks found after BrCN and ClCN exposure at room temperature on Si(100) are similar to those found for ICN and support the existence of intact CN function groups. As in the case of ICN, no contributions are found from the molecularly adsorbed species. The UPS spectra of BrCN and ClCN are more complicated than ICN due to the contribution of adsorbed atomic Br and Cl on the surface. However for both BrCN and ClCN, the CN species bonded to the Si(100) surface contributes only a single peak (6.0 eV) due to the π electrons in CN bond to the UPS spectra. This result indicates that the I-CN, Br-CN and Cl-CN bonds break while the CN bond remains intact during room temperature adsorption on Si(100). Upon annealing the CN saturated Si(100) surface to higher temperatures, the UPS and XPS spectra indicate that the CN triple bond starts to disappear at approximately 470 K. Simultaneous changes in the C 1*s* and N 1*s* photoelectron peaks between 470 and 800 K are consistent with the idea that CN bond cleavage is correlated with silicon carbide and nitride formation. By 800 K, all adsorbed CN species decompose completely into silicon carbide and nitride. These annealing results are similar with the results obtained for the CN saturated Si(100) surface prepared using other analogous CN containing systems.[51,53,66]

CHAPTER III

COMPUTATIONAL STUDIES OF ADSORPTION AND DISSOCIATION PATHWAYS OF CYANOGEN HALIDES ON Si(100) SURFACE

A. Introduction

To support the experimental results presented in the previous chapter, the adsorption of ICN, BrCN and ClCN was studied theoretically by performing *ab initio* quantum computations. The adsorption and dissociation pathways parallel to the Si-Si dimer bond were calculated with the help of Gaussian 98 package.[101] The Si(100)-2×1 surface was modeled by single dimer (Si_9H_{12}), double-dimer ($Si_{15}H_{16}$) and triple-dimer ($Si_{21}H_{20}$) clusters. The Si_9H_{12} cluster was utilized to investigate adsorption geometries and transition states, while the larger, more computationally demanding $Si_{15}H_{16}$ and $Si_{21}H_{20}$ clusters were used to assess cluster size dependent effects.

Besides pathways parallel to the dimer bond, additional pathways perpendicular to the Si-Si dimer bond were explored. Computations in this case were performed for the ClCN molecule adsorbed on double-dimer and triple-dimer clusters, since the single-dimer cluster does not allow investigation of the migration of Cl atom from one dimer bond to another. Finally, the energetics of a second ClCN molecule adsorption on Si (100) surface was studied using double-dimer, tripler-dimer and v-trench ($Si_{23}H_{24}$) clusters. The v-trench cluster was also used to investigate possible cluster size effects in the direction perpendicular to the dimer row.

The data related to the investigation of dissociation pathways parallel to the dimer bond are based on the studies presented in Refs. 102,103.

B. Quantum computation procedure

Energy calculations, geometry optimizations and frequency calculations were performed using the hybrid density functional method that includes Becke's 3-parameter nonlocal-exchange functional[104] with the correlation functional of Lee-Yang-Parr, B3LYP.[105] The 6-31G* all-electron split-valence basis set,[106] which includes the polarization *d*-function on non-hydrogen atoms, was employed for all BrCN and ClCN calculations. For the ICN calculations, the LanL2DZ basis, which includes the D95 double-zeta basis set,[107] combined with Hay and Wadt's effective core potential[108] was utilized for I. The larger 6-311++G(2d,p) basis set was utilized in selected calculations to verify the suitability of the 6-31G* basis set. The adsorption energy was defined as the difference between the total electronic energy of the adsorption model and the isolated molecule and cluster. All energies are reported without zero-point corrections. Frequency calculations confirm that the stable geometries have real vibrational frequencies. For the transition states, the optimized Gaussian 98 geometries contain only one imaginary normal mode. For all structures, atomic positions were optimized without geometry constraints. The buckling angle was calculated with respect to a plane that passes through the four Si atoms directly below the Si-Si dimer that was bonded to the cyanogen halide species.

The Si(100) surface was represented either as a single-dimer Si_9H_{12}, double-dimer $Si_{15}H_{16}$, triple-dimer $Si_{21}H_{20}$ or a v-trench $Si_{23}H_{24}$ cluster. The Si_9H_{12} cluster has been

utilized in the previous study of HCN[67] adsorption on Si(100) surfaces. In addition, this cluster was used in studies of other nitrogen containing compounds, such as ammonia and various amines.[20,21,109-111] However, the initial dative bonding geometry for ammonia and HCN is sensitive to the cluster size.[20,68] Size dependent effects on both the resulting stable structures and selective transition states were investigated using the larger $Si_{15}H_{16}$ and $Si_{21}H_{20}$ cluster. In order to study the lateral interactions and cluster-size effects on the adsorption of XCN on the surface the v-trench cluster $Si_{23}H_{24}$ was also involved.

C. Results and discussion

C.1. Gas-phase isomerization

The gas phase ICN to INC isomerization represents a straightforward chemical process to examine the effects of the two different basis sets. The B3LYP optimized geometric parameters (bond lengths and angles), vibrational frequencies (both stretching and bending) and relative total energies computed for ICN and INC utilizing both the LanL2DZ+6-31G* and CEP-31G+6-31G* basis sets are summarized in Table III-1. All energies are relative to ICN. Table 1 also includes optimized ICN and INC geometries and energies performed by Samuni *et al.*[112] using quadratic configuration interaction (including single and double excitations and a perturbational estimate of the triple excitations, QCISD(T)[113]), with both the LanL2DZ and CEP-31G basis sets. The experimental fundamental vibrational frequencies for ICN reported in Table III-1 are taken from a high resolution infrared spectroscopy study.[114] For INC, only low resolution values are available.[112] The tabulated equilibrium IC and CN bond lengths for ICN are determined by microwave spectroscopy.[115] Table III-1 shows that the density-functional

calculations for molecular ICN are essentially basis set independent since both basis sets accurately represent the experimentally determined quantities. These results are also consistent with calculations by Samuni *et al.*[112] Although both basis sets are acceptable, the B3LYP/LanL2DZ+6-31G* method was chosen for all further calculations involving ICN species.

Table III-1. *B3LYP geometries (distance in Å and angles in degrees), fundamental frequencies, ν_1 – IC stretching mode, ν_2 – bending mode, ν_3 – CN stretching mode, (cm^{-1}) and relative energies (kJ/mol) of ICN and INC with respect to ICN obtained utilizing the Set 1 (LanL2DZ+6-31G*) and the Set 2 (CEP-31G+6-31G*). The QCISD(T)/LanL2DZ results of Samuni et al[112] are included for comparison. In addition, experimental results from (a) Ref. 115, (b) Ref. 114 and (c) Ref. 112 are provided.*

	ICN				INC			
	Set 1	Set 2	QCISD(T)	Exper.	Set 1	Set 2	QCISD(T)	Exper.
R_{CI}	2.0147	2.0178	2.013	1.992[a]				
R_{NI}					2.0050	2.0136	1.991	
R_{CN}	1.1634	1.1636	1.185	1.160[a]	1.1856	1.1856	1.203	
ν_1	469	464	487	489[b]	442	443	479	494[c]
ν_2	325	314	309	304[b]	184	182	226	~200[c]
ν_3	2299	2296	2178.6	2179[b]	2146	2145	2073	2058[c]
$E_{rel,}$	0.0	0.0	0.0		123.1	123.4	118.3	

The B3LYP/6-31G* isomerization energy for BrCN is within 10 kJ/mol of that in a MP2/6-31G* study[116] and within 6 kJ/mol of a calculation using a closed-shell single and double coupled-cluster method that includes a perturbational estimate of the effects of connected triple excitations (CCSD(T)) with a 6-31G(p,d) basis set. Although the BrC bond length obtained using the B3LYP and the MP2 methods agree well, the B3LYP/6-31G* CN bond length is 0.03Å shorter than that found using MP2/6-31G*. Differences in

bond lengths between B3LYP/6-31G* results and CCSD(T)/6-31G(d,p) results are within 0.01Å. In addition, B3LYP/6-31G* BrC and CN bond lengths for BrCN are within 0.01Å of the experimental values determined by microwave spectroscopy.[117]

For ClCN, the isomerization energy obtained at the B3LYP/6-31G* level is within 2.5 kJ/mol of that calculated using CCSD(T) level with a cc-pVTZ basis set.[118] The bond length differences are less than 0.01 Å for both ClCN and ClNC. The final computed structure for ClCN also agrees favorably with the experimentally determined structure.[117,119] Thus, B3LYP/6-31G* method gives good agreement with both experimental and theoretical results for molecular BrCN and ClCN.

C.2. One-molecule adsorption

C.2.1. Dissociation pathways parallel to the Si-Si dimer-bond

Possible adsorption structures for XCN on single-dimer clusters are shown in Figure III-1. Without dissociation, the cyanogen halides can be adsorbed into two states: XCN1 and XCN2. In XCN1, the nitrogen lone pair forms a dative bond between the nitrogen end of the XCN molecule and the electrophilic (buckled-down) Si-dimer atom. Even with constrained geometry optimizations, no stable binding geometry is found for an analogous geometry in which the lone pair of the halide binds to the electrophylic Si-dimer atom. XCN2 is generated by the reaction of the CN group across the silicon-dimer to achieve a side-on configuration. Following XC bond cleavage, Figure III-2 illustrates three additional structures, XCN3, SiNC and SiCN. The SiNC and SiCN configurations contain an intact CN functional group bonded to the Si-dimer atom through either the N or C end. The halide is bonded to the Si-dimer atom opposite to the dimer atom bonded to

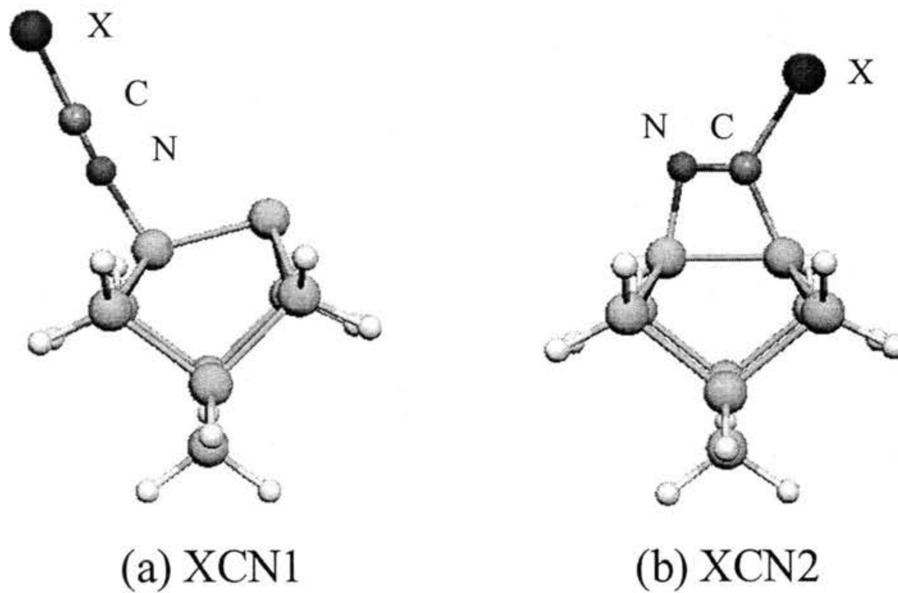

Figure III-1. XCN derived adsorption models on the Si single-dimer cluster. (a) XCN1: XCN adsorbed on Si(100) surface in an end-on position. (b) XCN2: XCN adsorbed on Si(100) surface in a side-on position. Adapted from Ref. 103.

the CN group. The XCN3 model has the C atom of the CN group inserted between the Si-dimer atoms. The reported SiC distance for this species was measured with respect to the Si-dimer atom bonded to the halide.

Geometry optimization at the B3LYP/6-31G* level for the XCN1, XCN2, SiNC and SiCN adsorption models for ICN were performed on single-dimer clusters for ICN. To further verify the acceptability of the 6-31G* basis sets for this system, additional calculations were performed for the ICN using the larger 6-311++G(2d,p) basis for the Si-dimer atoms and the N and C species. The results are summarized in Table III-2. The final geometry and total energy of these 6-31G* results are within 7 kJ/mol of that found using the larger basis set. The largest relative error between these two sets is found for the dative bonded XCN1 structure. Consistent with careful studies of ammonia adsorption on silicon clusters, the 6-31G* results are within 4 kJ/mol of the larger 6-311++G(2d,p) basis set.[20] Similar results are also found for methylamine adsorption on Si single-dimer clusters.[17,109] Thus, all further calculation were performed at the B3LYP/6-31G* level.

The computed adsorption energies for these five stable ICN, BrCN and ClCN adsorption structures on both single- and triple-dimer clusters are listed in Table III-3. For the triple-dimer cluster, the middle dimer is used for the adsorption site, while the two end dimers are bare. As an example, the triple-dimer XCN1 geometry is illustrated in Figure III-3. Since the formation of the XCN end-on adsorption structure (XCN1) from gas-phase ICN, BrCN and ClCN does not require bond cleavage, no adsorption barrier is expected. On the single cluster, the adsorption is exothermic with total energy changes of -54.2, -51.0 and -44.7 kJ/mol for ICN, BrCN and ClCN, respectively (see Table III-2).

With increasing halide electronegativity, the energy change decreases by a small amount. One explanation is that with the increased electronegativity of the halide, there is a decrease in the electron density that the nitrogen atom can donate to the dative bond. The

Table III-2. *B3LYP calculated geometries and adsorption energies (kJ/mol) for the ICN adsorption structures on single-dimer clusters. "St" refers to the standard 6-31G* basis while "Ex" refers to the larger 6-311++G(2d,p) basis for the Si dimer atoms and the N and C species. The bound distances are in Å while the XCN and SiSi buckling angles are in degrees. The SiC distance for ICN3 is measured with respect to the Si dimer atom bound to the halide.*

		ICN1	ICN2	ICN3	SiNC	SiCN
R_{IC}	St	2.004	2.240			
	Ex	1.973	2.200			
R_{CN}	St	1.162	1.264	1.258	1.186	1.165
	Ex	1.159	1.266	1.261	1.179	1.161
R_{SiC}	St		1.953	1.866		1.852
	Ex		1.944	1.853		1.846
R_{SiN}	St	1.893	1.845	1.883	1.756	
	Ex	1.866	1.827	1.857	1.749	
R_{SiSi}	St	2.383	2.358	3.534	2.404	2.403
	Ex	2.374	2.349	3.489	2.400	2.398
R_{ISi}	St			2.531	2.512	2.510
	Ex			2.505	2.488	2.486
∠ICN	St	180.0	120.6			
	Ex	179.4	120.6			
∠SiSi	St	10.6	0.43		0.32	0.32
	Ex	10.4	0.44		0.54	0.58
E_{rel}	St	-54.2	-192.9	-264.3	-344.5	-376.7
	Ex	-58.9	-191.0	-264.8	-351.9	-375.6

net result is a reduction in the adsorption energy. These results are consistent with the calculated -49.6 kJ/mol adsorption energy for an analogous HCN structure.[67] A lower adsorption energy of -69.6 kJ/mol is calculated using B3LYP/6-31G* for acetonitrile

(CH_3CN)[120] and is possibly due to the electron donating ability of the CH_3 group as compared to H or halide substitution. The single-dimer XCN adsorption energies are also less than the -96.2 kJ/mol value for ammonia, calculated using B3LYP/6-311++G(2df,2pd) and a single-dimer cluster,[20] or the -120 to -90 kJ/mol range found for methyl, dimethyl and trimethylamines calculated using a single-dimer cluster and B3LYP with varying basis sets.[17,109,110] The sp^3 N in both ammonia and amines appears to be able to form a stronger bond by donating more charge to the Si- dimer atom than the *sp* N in the CN triple-bonded species. This effect is consistent with the decreasing electron donor strengths due to the increasing *s* character of the lone pair.[121]

The reaction pathways between the various ClCN single-dimer derived adsorption configurations, along with the computed transition states energies, are shown in Figure III-4. Due to the similarity, the reaction pathways for ICN and BrCN on Si single-dimer clusters are not shown. All transition states contain one imaginary frequency and are further verified using the internal reaction coordinate (IRC) option in Gaussian 98. This procedure[122,123] computes the lowest energy pathway from the given transition state to either the product or the reactant. The primary pathway from the gas phase XCN species to the lowest energy of the dissociated structure, SiCN, is shown as a solid line in Figure III-4. Table III-4 reports the single-dimer transition state energies, while Table III-5 and Table III-6 list the geometrical parameters. At room temperature, UPS and XPS measurements indicate that molecular ICN, BrCN and ClCN dissociate upon exposure to the Si(100) surface and form an atomic halide and molecular CN species (see Chapter 2). Assuming that the reaction pathways shown in Figure III-4 are followed experimentally, some tentative conclusions can be inferred. The initial dative-bonded end-on adsorption

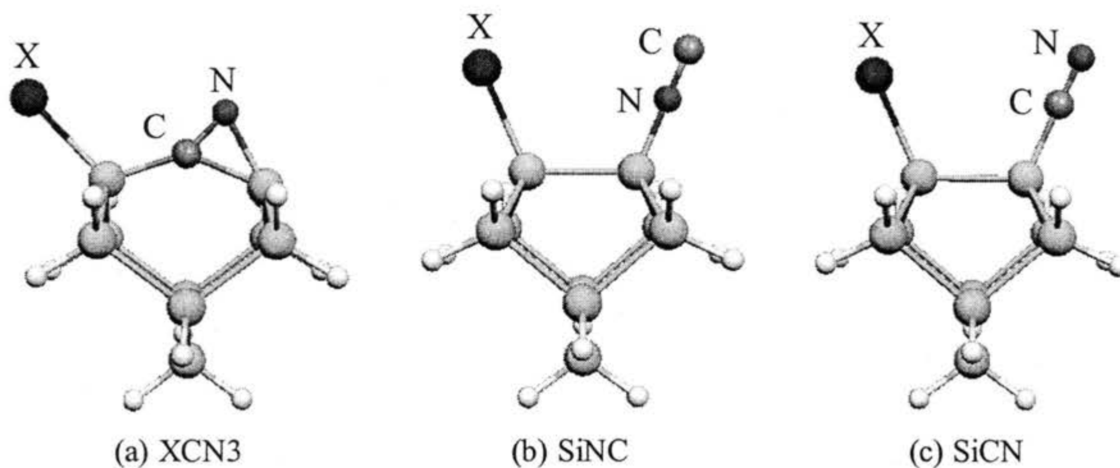

Figure III-2. Additional XCN derived adsorption models on the Si single-dimer cluster. (a) XCN3: Dissociated X and CN species adsorbed in a side-on position. Both the X-C and the silicon dimer bonds are broken. (b) SiNC: Dissociated X and NC species adsorbed on Si(100) surface. (c) SiCN: Dissociated X and CN species adsorbed on Si(100) surface. Adapted from Ref. 103.

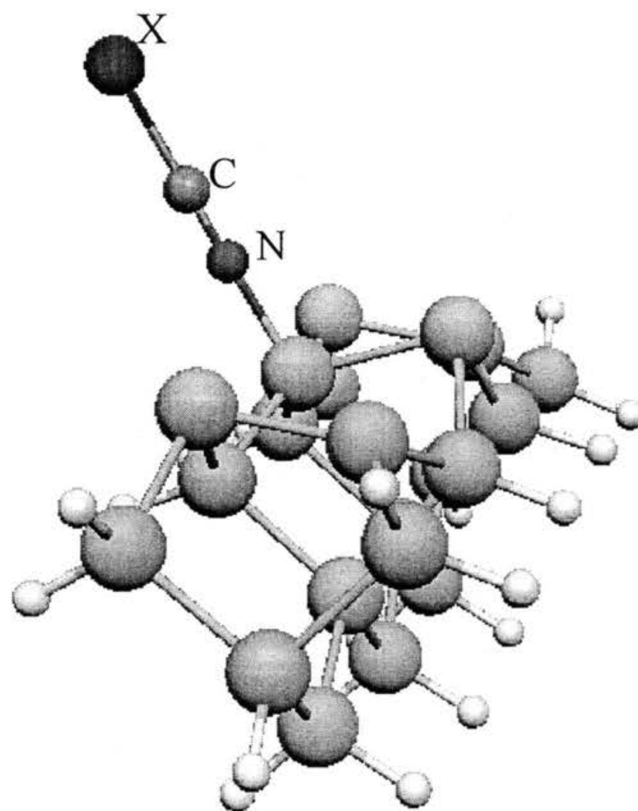

Figure III-3. XCN1 adsorption model utilizing the Si triple-dimer cluster. Adapted from Ref. 103.

structure (XCN1) is expected to form via a barrierless transition state. Similar conclusions have been drawn for other dative-bonded species such as HCN, acetonitrile, ammonia and various amines.[17,20,21,67,68,109,110,120] Assuming that kinetic energy gained through adsorption can be utilized, ICN1 and BrCN1 can react, through transition state

Table III-3. *Calculated B3LYP/6-31G* adsorption energies (kJ/mol) for XCN1, XCN2, XCN3, SiNC and SiCN adsorption structures on single-dimer (1D) and triple-dimer (3D) clusters. Percent differences are with respect to the single-dimer energy. Negative percent differences indicate that the triple-dimer is lower in energy.*

		XCN1	XCN2	XCN3	SiNC	SiCN
I	1D	-54.2	-192.9	-264.3	-344.5	-376.7
	3D	-81.3	-180.6	-240.7	-337.1	-367.9
%Difference		-50.0	6.4	8.9	2.1	2.3
Br	1D	-51.0	-198.9	-303.3	-380.5	-413.4
	3D	-78.9	-187.1	-281.8	-375.7	-407.3
%Difference		-54.7	5.9	7.1	1.3	1.5
Cl	1D	-44.7	-202.3	-289.4	-365.3	-397.9
	3D	-72.5	-189.9	-266.0	-359.0	-390.3
%Difference		-62.2	6.1	8.1	1.7	1.9

TS2, to form SiNC directly. The small buckling of the Si dimer atoms in TS2 (see Table III-6) indicates a relatively weak dative bond. In addition, the XCN molecule is bent and the CN bond is slightly (0.02 Å) elongated with respect to that found for gas-phase XCN. Due to the strength of the ClC bond, the transition state (TS2) between ClCN1 and SiNC is only 1.5 kJ/mol less than the energy of the isolated ClCN molecule and the single-dimer cluster. For the triple-dimer cluster, the energy is greater than that for the isolated species by 2.9 kJ/mol. Thus, the pathway between ClCN1 and SiNC through TS2 is

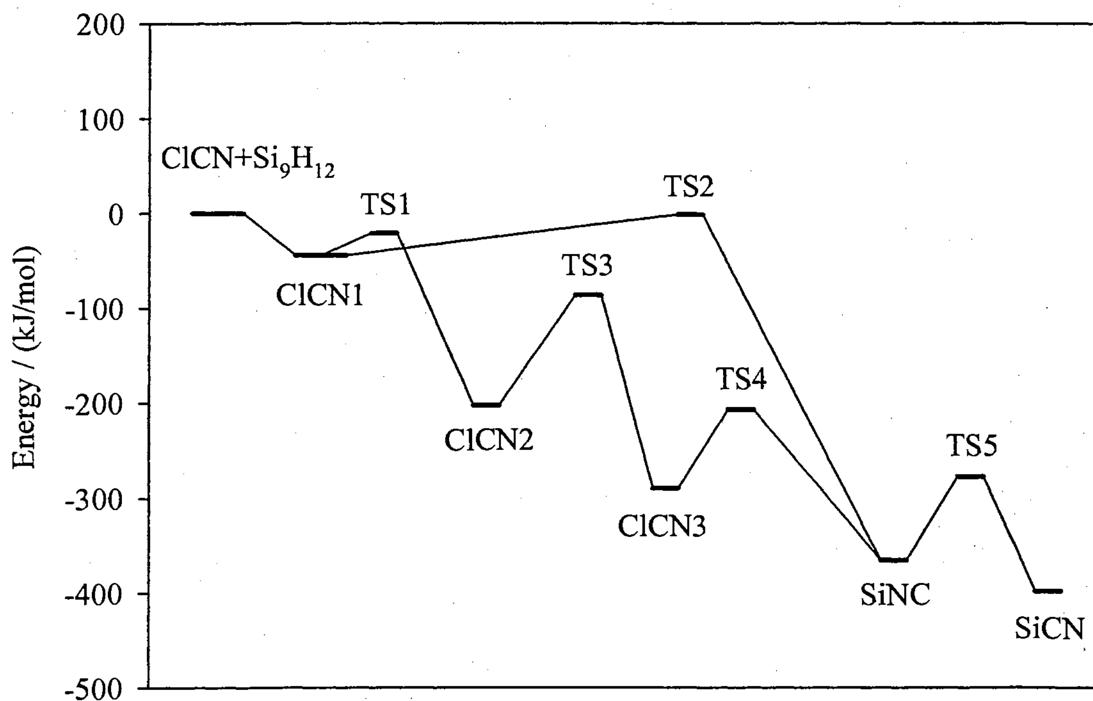

Figure III-4. Potential energy profile for different adsorption modes of XCN and their transition states on Si single-dimer cluster. The solid line represents the primary pathways for the decomposition of XCN into adsorbed atomic X and molecular CN. Adapted from Ref. 103.

unlikely. For ICN and BrCN, the adsorption energy of TS2 is negative and barrierless adsorption into this state may be possible. Thus, SiNC could be formed directly from the gas-phase via TS2. If SiNC via TS2 is energetically possible, the resulting kinetic energy gained is more than sufficient to overcome the barrier between SiNC and the final experimentally observed product, SiCN. An examination of the transition state structure TS5 between SiNC and SiCN reveals a partial breaking of the SiN bond before the SiC bond fully forms, which results in the 90 kJ/mol barrier. Supporting this conclusion, the barrier height is also independent of the halide.

The second pathway to form SiCN involves a 1,2-dipolar addition reaction of XCN1 across the Si dimer to achieve an intermediate side-on configuration, XCN2, through TS1. The Si dimer atoms in the TS1 geometry (see Table III-5) are buckled by approximately 8 degrees. In addition, XCN molecule is dative-bonded to the electrophylic (buckled-down) Si-dimer atom. Thus barrierless adsorption into TS1, followed by the direct formation of XCN2, may be possible. Similar conclusions have been reached for HCN[67,68] and CH_3CN.[120] Assuming that the single-dimer pathway represents the experimental pathway and given that the experimental species formed at room temperature is SiCN, the newly created XCN2 species must possess sufficient energy to overcome TS3, TS4 and TS5. If there is no thermal accommodation of the XCN2, this species will have enough kinetic energy to form XCN3 through TS3. The newly formed XCN3 species can use the kinetic energy gained from the previous reaction (again, assuming no thermal accommodation) to further reaction through TS4 giving SiNC. Finally, SiNC contains more than sufficient kinetic energy to overcome the barrier between SiNC and SiCN, the experimentally observed product. Given the calculated

Table III-4. *Calculated B3LYP/6-31G* adsorption energies (kJ/mol) for the single-dimer transition state models.*

	TS1	TS2	TS3	TS4	TS5
I	-38.4	-29.7	-116.2	-177.1	-255.6
Br	-25.2	-12.3	-106.1	-218.9	-292.4
Cl	-21.3	-1.5	-86.5	-206.9	-277.2

Table III-5. *Calculated B3LYP/6-31G* geometries for TS1 and TS2 transition states on a single-dimer (1D) cluster. The bond distances are in Å while the XCN and SiSi buckling angles are in degrees.*

	TS1			TS2		
	I	Br	Cl	I	Br	Cl
R_{XC}	2.230	1.812	1.653	2.538	1.850	1.689
R_{CN}	1.189	1.182	1.182	1.186	1.187	1.194
R_{SiN}	1.787	1.848	1.848	1.793	1.920	1.927
R_{SiSi}	2.418	2.405	2.408	2.333	2.326	2.315
∠XCN	139.4	156.1	153.3	131.0	141.7	141.2
∠SiSi	5.5	8.9	9.1	0.92	4.9	3.7

Table III-6. *Calculated B3LYP/6-31G* geometries for TS3, TS4 and TS5 transition states on single-dimer clusters. The bond distances are in Å and the XCN angles are in degrees.*

	TS3			TS4			TS5		
	I	Br	Cl	I	Br	Cl	I	Br	Cl
R_{CX}	2.873	2.520	2.434						
R_{CN}	1.220	1.221	1.219	1.222	1.224	1.223	1.191	1.190	1.191
R_{SiC}	1.865	1.849	1.848	2.124	2.108	2.126	2.022	2.020	2.022
R_{SiN}	1.939	1.944	1.947	1.875	1.873	1.874	2.110	2.120	2.116
R_{SiSi}	2.468	2.471	2.471	2.529	2.547	2.549	2.404	2.399	2.404
R_{XSi}	3.205	2.905	2.820	2.628	2.305	2.154	2.510	2.240	2.101
∠XCN	140.7	141.0	140.5						

barrier height, it is reasonable to assume that the reaction proceeds to the experimentally observed SiCN species at room temperature. The driving force for the formation of this

dissociated species is the replacement of the XC bond with the stronger XSi and SiC bonds.

The 1,2-dipolar addition reaction products from acetonitrile[70,71] and benzonitrile[74] on the Si(100) surface were experimentally observed. For acetonitrile, an adsorbed CH_3 group replaces the halide in the analogous SiCN geometry. Unlike the XCN, SiCN species where a strong XSi bond replaces a weaker XC bond, the formation of an analogous dissociated species from the nitriles requires that a strong CC bond is replaced by weaker SiC bond. In addition, a large activation energy is expected due to the need to break a CC bond. Thus, in contrast with XCN, the 1,2-dipolar addition reaction products from acetonitrile and benzonitrile are stable. For HCN, a stable side-on structure surrounded by transition state barriers larger than the adsorption energy is predicted.[67,68] The stronger HC bond with respect to the HSi bond gives the analogous HCN structure greater stability than that of XCN2. For XCN2, a low barrier reaction pathway driven by the formation of a strong XSi bond destabilizes this structure. In addition, a side-on adsorbed HCNH species was observed experimentally for HCN adsorption on Si(100) surfaces.[51] In contrast, an analogous species was not observed in UPS and XPS studies of XCN adsorption on Si(100) surfaces (Chapter 2). For HCN, surface H liberated by the formation of CN functional groups can further react with other adsorbed HCN molecules, leading to the HCNH species on the Si(100) surface. The formation of HCNH from the interaction between two HCN molecules on double-dimer clusters has been studied theoretically.[68] The formation of an HCNH species and a CN function group on a double-dimer is only 4 kJ/mol greater than two isolated side-on adsorbed species. The formation of the additional HN bond in HCNH counterbalances the loss of the HC bond required to

form the separately adsorbed CN functional group. Unlike HCNH, XCNX side-on species is expected to be energetically unstable with respect to separately adsorbed halides and CN functional group due to the stronger XSi bond as compared to either the XC or XN bond.

The adsorption studies of the INC isomer show that the analogous structure to XCN1 (XNC1) is improbable due to an abnormally long IN bond length. Similar results were found for both BrNC and ClNC. In addition, an intermediate side-on configuration structure analogous to XCN2 (XNC2) was also found for ICN. For ICN, there is a large barrier between the lowest energy SiCN species and the XNC2 species. In addition, the energy of the XNC2 species is only slightly below the transition state energy between SiCN and XNC2. Thus, these analogous XNC adsorption geometries are not expected to play a role in the surface reaction chemistry of XCN and are therefore not considered further.

C.2.2. Dissociation pathways perpendicular to the Si-Si dimer bond

Due to computational limitations the dissociation pathways across the Si-Si dimer bond are calculated only for ClCN molecule adsorbed on the Si(100) surface. The energies for the adsorption structures of ClCN dissociated along the dimer row are listed in Table III-7, and those for the transition states – in Table III-8. Two possible adsorption and dissociation pathways for one ClCN molecule perpendicular to the dimer bond were studied with the help of a double-dimer cluster. In the first case (Figure III-5) in the side-on intermediate ClCN2 obtained on a regular pathway parallel to the dimer bond from an end-on configuration, the Cl atom migrates to the adjacent Si-Si dimer bond. After that

CN-bridge left on the first dimer-bond can brake to produce CN species bound to the surface either through C or N atom. However the structure, in which CN and Cl species are attached on the same side of the cluster is unstable and leads to highly deformed cluster SiCN3. Imposing constraints on the Si atoms of low layers of the cluster results in the configuration with one imaginary frequency. This is also consistent with impossibility for Cl atom to migrate from the end-on structure to the Si atom of the adjacent dimer bond on the same side. The explanation of this phenomenon is that this Si atom possesses more negative charge than the Si of the same dimer bond (-0.0758e versus –0.0183e) and nucleophilic nature of the former prevents from both dissociation and adsorption of another ClCN molecule through dative N-Si bond on this site. Therefore, this mode cannot be considered as stable one and is not included in a main pathway further.

Another structure obtained on this pathway is that with Cl and CN species bound to different dimer bonds on the opposite sides of the cluster (SiNC2 and SiCN2). It leads further to the formation of SiCN1 mode in which Cl and CN are attached to the same Si-Si dimer bond via Cl migration. The configuration with CN species bound to the surface through its C atom is lower in energy than when it is bonded via the N atom. This is consistent with the corresponding potential energy diagram for this pathway, given in Fig. III-6.

In the second pathway the side-on configuration 2ClCN2 is formed across the two dimer bonds (Fig. III-7). Cl atom migrates to the adjacent Si atom forming an intermediate with CN-bridge connecting two Si atoms of the different dimer bonds

Table III-7. *Calculated B3LYP/6-31G* adsorption energies (kJ/mol) for one-molecule ClCN adsorption structures on a double-dimer* $Si_{15}H_{16}$ *cluster.*

Pathway	ClCN1	ClCN2	CNside	SiNC2	SiCN2	SiNC1	SiCN1
1	-62.8	-198.2	-284.3	-272.7	-304.9	-365.4	-397.4
2		-238.0	-327.4				
1-Dimer	-44.7	-202.3				-365.3	-397.9

Table III-8. *Calculated B3LYP/6-31G* adsorption energies (kJ/mol) of the transition states for one-molecule ClCN adsorption structures on a double-dimer* $Si_{15}H_{16}$ *cluster.*

Pathway	TS1	TS2	TS3	TS3a	TSside	TS4	TS4a	TS5a
1	-33.2	-2.5	-132.8		-224.6	-277.7	-180.7	-268.0
2	-54.6		-114.1	-327.1	-242.4			

(2CNside). Like before, two ways of breaking this bridge lead to the formation of either SiCN1 structure with Cl and CN species bound to the same dimer bond or SiNC2 configuration where Cl and CN are connected to the different dimer bonds on the opposite sides. In the latter case the process of migration of Cl atom to another dimer bond is analogous to that in the first pathway described above. Eventually both pathways result in the formation of the SiCN1 structure. The energy diagram for the second pathway also displays that this state possesses the lowest potential energy and, therefore, is the most energetically stable configuration (Fig. III-8).

The existence of these pathways can explain why the side-on structure ClCN2 is not observed experimentally in XPS experiments (see Chapter 2). Indeed, the Cl atom can migrate between two adjacent dimers with a quite low transition barrier creating the possibility for a ClCN2 configuration to dissociate quickly and transform into the dissociated Cl and CN species on the Si(100) surface.

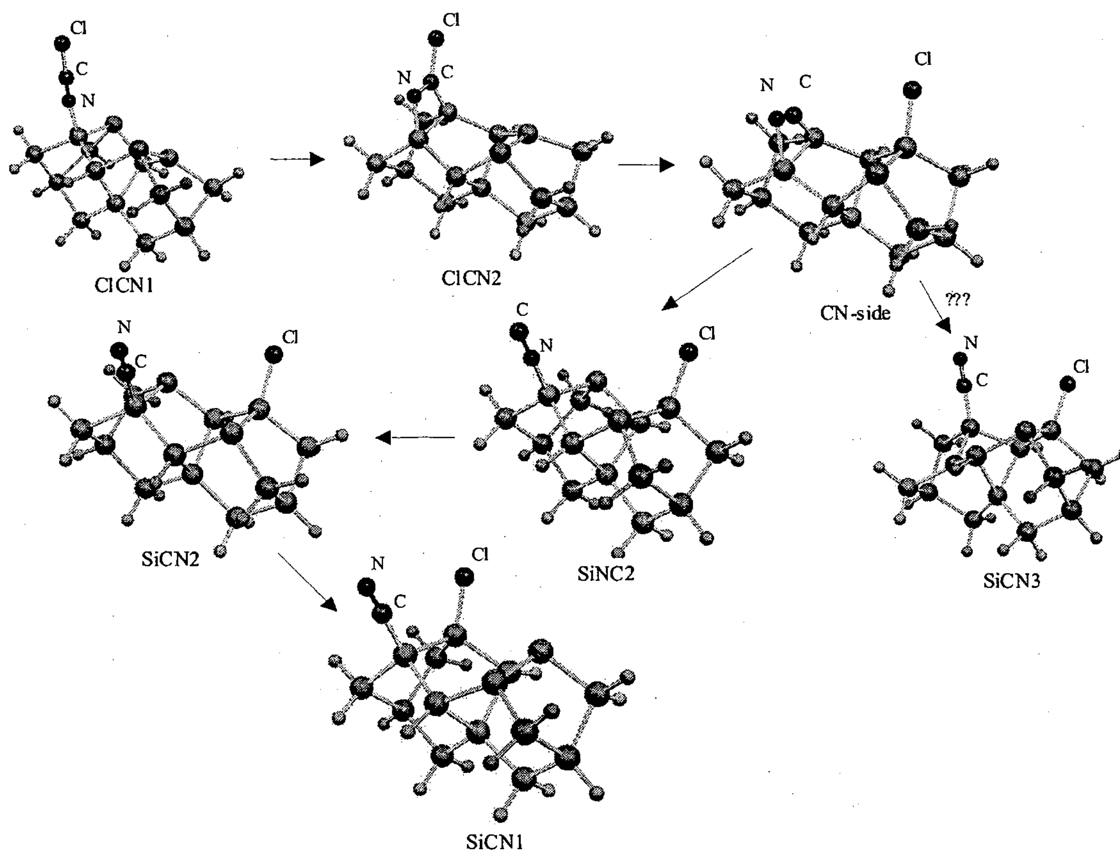

Figure III-5. First adsorption and dissociation pathway perpendicular to the dimer bond for one ClCN molecule adsorbed on a double-dimer cluster.

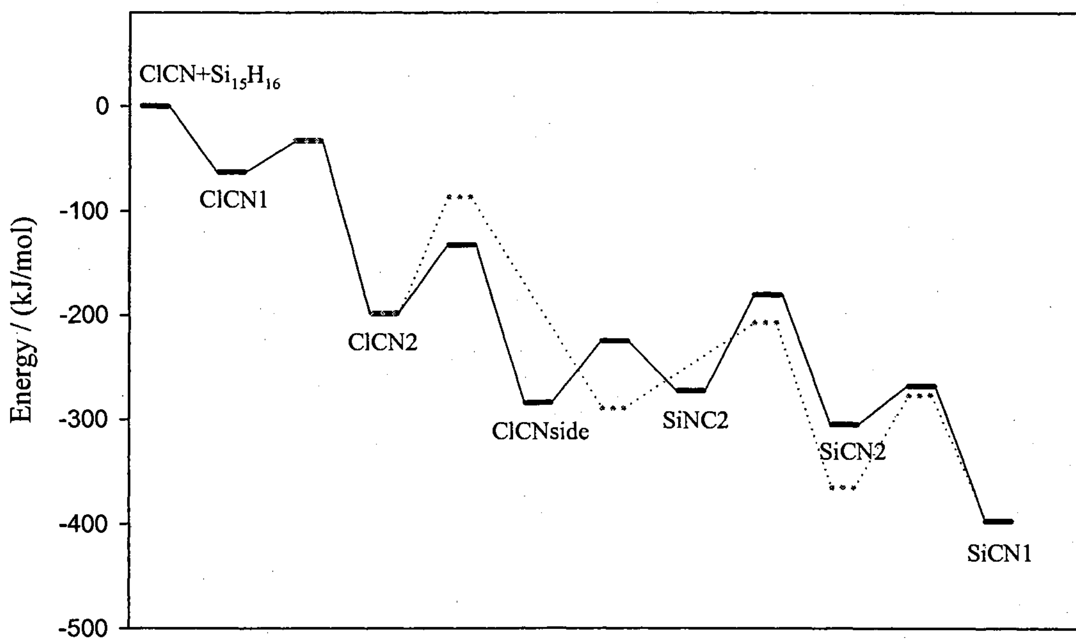

Figure III-6. Potential energy profile for different adsorption modes of one ClCN molecule on a double-dimer cluster corresponding to the first pathway perpendicular to the dimer bond. Dotted line depicts the pathway parallel to the dimer bond.

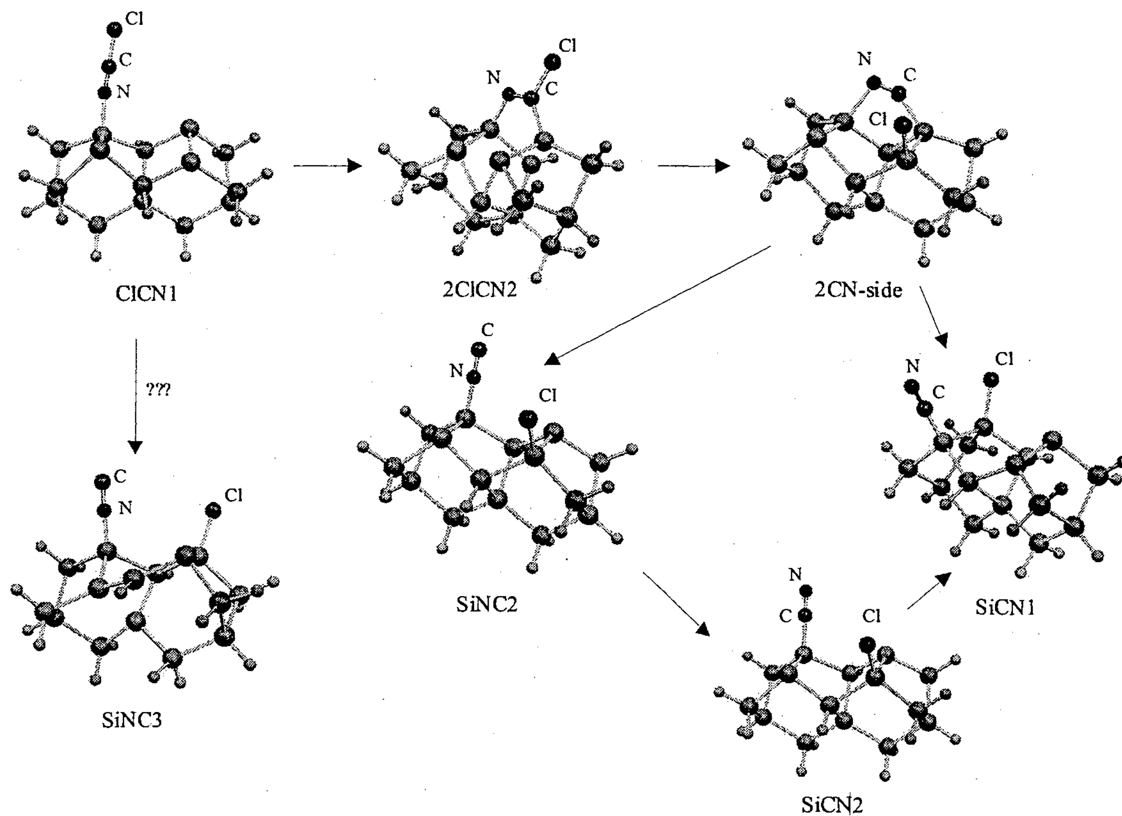

Figure III-7. Second adsorption and dissociation pathway perpendicular to the dimer bond for one ClCN molecule adsorbed on a double-dimer cluster.

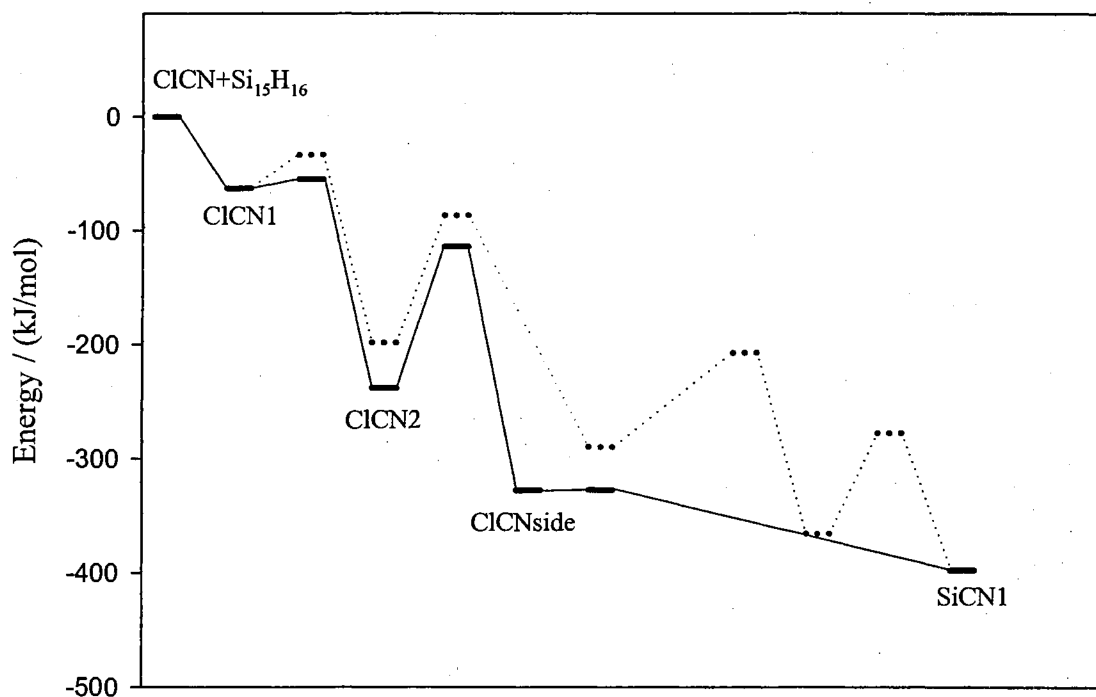

Figure III-8. Potential energy profile for different adsorption modes of one ClCN molecule on a double-dimer cluster corresponding to the second pathway perpendicular to the dimer bond. Dotted line depicts the pathway parallel to the dimer bond.

C.2.3. Cluster-size effects

In order to study the influence of a cluster size on the adsorption energy of XCN on Si(100) surface the stable adsorption configurations for the dissociation pathway parallel to the dimer bond were calculated with the use of the triple-dimer and v-trench clusters. Utilizing a triple-dimer cluster for ICN1, BrCN1 and ClCN1, the adsorption energy for XCN1 is consistently found to be 27 to 28 kJ/mol lower (see Table III-3) than that for a single-dimer. These differences correspond to a 50% error with respect to the single-dimer results. Thus, the total electronic energy of the dative bond structure is strongly dependent on the cluster size. For molecular ammonia adsorption, a 25 kJ/mol difference was found between a single-dimer and larger clusters using B3LYP/6-31G*,[20] while a 28 kJ/mol difference was found using B3LYP/6-311+G(2d,p).[109] This energy difference is attributed to a greater ability of the larger clusters to delocalize the additional density created by the dative bond along the dimer row. For the analogous HCN configuration, Bacalzo-Gladden *et al.* found an energy difference, including zero-point corrections, of 28 kJ/mol between the single- and double-dimer silicon clusters.[67] From these results, the magnitude of the cluster size effect appears to depend only on the presence of a dative bond and is relatively independent of the substitution on the nitrogen atom.

For XCN1, the geometrical parameters (see Table III-9) obtained from both single- and triple-dimer clusters are practically identical. In the XCN1 geometries, the CN bond length is only 0.04 Å greater than the gas-phase value, indicating that the CN triple bond is intact. In all cases, the nitrogen lone pair forms a dative bond between the nitrogen end of the XCN molecule and the electrophilic (buckled-down) Si generated by

an 11 to 12 degree buckling of the Si-dimer. The magnitude of the buckling is virtually independent of XCN species and cluster size. These buckling angles are consistent with 13 degree buckling found for ammonia[20,21,111] and the 10 degree buckling found for methylamines.[109]

The XCN2 species were generated by the reaction of XCN1 across the Si-dimer to achieve an intermediate side-on configuration. This 1,2-dipolar addition of the CN group across the Si-dimer bond results in a four member Si_2NC ring. For phenyl isothiocyanate,[73] acetonitrile[70,71,120,124] and benzonitrile[74] on the Si(100) surface, 1,2-dipolar addition reactions that result in a four member Si_2NC ring are theoretically predicted and experimentally observed. The calculated energy difference (see Table III-3) between the single- and triple-dimer XCN2 models is 12 kJ/mol. In contrast to the XCN1 results, this represents only a 6 % error with respect to the single-dimer result. Importantly, the adsorption energies of the triple-dimer clusters models are always smaller than that found for the single-dimer. Unlike XCN1, the Si-dimer atoms are unbuckled. For NH_3 adsorption, the additional strain energy due to the unbuckling is better described by the triple-dimer cluster and results in a 12 kJ/mol decrease in adsorption energy for the dissociated structures.[20] For XCN2, a similar 12 kJ/mol decrease (see Table III-3) in the adsorption energy is observed with the triple-dimer clusters. The XCN2 geometrical parameters (see Table III-9) for the single- and triple-dimer clusters are practically identical. With the exception of the expected changes in the XC bond length, all of the XCN2 structures are geometrically similar. The CN bond is significantly longer (1.26 – 1.27 Å), indicating a CN double-bond. Thus, even if direct

adsorption into the XCN2 state is possible, a barrier due to the partial breaking of the CN triple bond is expected.

Table III-9. *Calculated B3LYP/6-31G* geometries for XCN1 and XCN2 adsorption structures on single-dimer (1D) and triple-dimer (3D) clusters. Bond distances are in Å, XCN and Si-Si buckling angles are in degrees.*

		XCN1			XCN2		
		I	Br	Cl	I	Br	Cl
R_{XC}	1D	2.004	1.770	1.624	2.240	1.964	1.793
	3D	1.996	1.767	1.622	2.241	1.963	1.792
R_{CN}	1D	1.162	1.162	1.161	1.264	1.271	1.274
	3D	1.161	1.161	1.160	1.262	1.269	1.272
R_{SiC}	1D				1.953	1.943	1.951
	3D				1.955	1.945	1.952
R_{SiN}	1D	1.893	1.894	1.903	1.845	1.839	1.834
	3D	1.880	1.881	1.889	1.858	1.851	1.846
R_{SiSi}	1D	2.383	2.386	2.384	2.358	2.358	2.355
	3D	2.399	2.399	2.398	2.335	2.335	2.333
∠XCN	1D	180.0	180.0	180.0	120.6	121.0	120.7
	3D	180.0	180.0	180.0	121.1	121.5	121.0
∠SiSi	1D	10.6	10.7	10.8	0.43	0.39	0.47
	3D	11.5	11.6	11.7	0.12	0.17	0.12

Table III-10 lists the optimized geometrical parameters obtained for the dissociated adsorption structures (XCN3, SiNC, SICN) on single- and triple-dimer clusters. Since creating these structures requires bond breaking, no barrierless adsorption channel from XCN in the gas-phase into the XCN3, SiCN or SiNC state is expected. Similar to XCN2, for XCN3 only a small 8 % difference is found between the single-dimer clusters and triple-dimer clusters. The geometrical parameters (see Table III-10) are also insensitive to cluster size effects. In this structure, the C atom of the CN species inserts between the two Si-dimer atoms. In studies of ammonia decomposition on Si

single-dimer clusters, the N atom of an NH species can insert itself between the two Si-dimer atoms.[21] The weakness of both the Si-dimer bond compared to other Si-Si bonds connecting the dimer atoms to the rest of the cluster and the reduction of strain energy from the mismatch between the Si-N and the Si-Si bond lengths result in the Si-dimer insertion structure having the lowest energy compared to all other possible insertion geometries. For XCN3, a similar argument can also be made for the insertion into the Si-dimer bond and not into the Si-Si backbone. As in the case of the side-on XCN2 species, the CN bond length implies that the CN bond has a double-bond character. Thus, the greater stability of this structure with respect to XCN2 is due to the formation of a strong SiX bond and two SiC bonds. Although, the XC bond in XCN is stronger than the typical XC bond[92] due to the overlap between the *p* orbital on the halide and the π-system on the CN group, the formation of the XSi bond compensates for the loss of this bond. Thus, the main energetic difference between XCN3 and XCN2 is the formation of an additional SiC and the loss of the weaker Si-dimer bond.

The SiNC and SiCN structures are energetically more stable than all other geometries. As in the case of XCN3, the XSi bond compensates for the loss of the XC bond. Thus, the additional stability of SiNC and SiCN structures is due to the retention of the CN triple bond and the Si-dimer bond along with the creation of a strong SiN or SiC bond, respectively. In addition, the SiN and SiC bonds are shorter than those found in the XCN3 structure. For acetonitrile[70,120,124] and benzonitrile[74] theoretical investigations of an analogous dissociated adsorption geometries was not attempted. The influence of the Si cluster size on the total energy of the SiNC and SiCN species is minimal. Only a small 2 % difference in the adsorption energy relative to the single-dimer clusters is found for

these dissociation structures. As in the case of XCN2, the decrease in the adsorption energy for the triple- dimer clusters relative to that found for single-dimer clusters is attributed to the additional strain energy created by the unbuckled Si-dimer.

Table III-10. *Calculated B3LYP/6-31G* geometries for SiNC and SiCN adsorption structures on single-dimer (1D) and triple-dimer (3D) clusters. The bond distances are in Å while the XCN and SiSi buckling angles are in degrees. For XCN3, the SiC distance is measured with respect to the Si dimer atom bound to the halide.*

		XCN3			SiNC			SiCN		
		I	Br	Cl	I	Br	Cl	I	Br	Cl
R_{CN}	1D	1.258	1.260	1.260	1.186	1.185	1.186	1.165	1.165	1.165
	3D	1.257	1.258	1.259	1.186	1.186	1.186	1.165	1.165	1.165
R_{SiC}	1D	1.866	1.867	1.866				1.852	1.853	1.853
	3D	1.851	1.852	1.849				1.852	1.854	1.853
R_{SiN}	1D	1.883	1.883	1.883	1.756	1.758	1.757			
	3D	1.892	1.891	1.891	1.756	1.758	1.757			
R_{SiSi}	1D	3.534	3.536	3.531	2.404	2.400	2.404	2.403	2.400	2.400
	3D	3.460	3.471	3.453	2.387	2.383	2.387	2.386	2.382	2.386
R_{XSi}	1D	2.531	2.251	2.108	2.512	2.242	2.103	2.510	2.240	2.102
	3D	2.535	2.246	2.109	2.513	2.239	2.103	2.512	2.238	2.102
∠SiSi	1D				0.32	0.55	0.25	0.32	0.55	0.20
	3D				0.98	1.3	0.94	1.0	1.3	0.97

The standard bond enthalpies of SiC and SiN are similar.[94] This similarity results in the relative closeness of the SiN and SiC adsorption energies. Computationally, the SiCN structure is on an average 30 kJ/mol more stable than SiNC. A similar small energy difference is also found between the analogous HCN structures.[67] The bonding of the CN functional group in the SiNC and SiCN structures is independent of the halide that is bound to the opposite Si-dimer atom. In both the SiNC and SiCN structures, the Si-dimer is practically unbuckled. The CN bond lengths for SiNC and SiCN are 1.18 Å and

1.16 Å, respectively, indicating a triple-bond character. In addition, the optimized geometrical parameters (Table III-10) are similar for both the single- and triple-dimer calculations. At most, a 0.02 Å difference is found for the Si-dimer bond length.

Table III-11. *Calculated B3LYP/6-31G* adsorption energies (kJ/mol) for one-molecule ClCN adsorption structures on a single-dimer (Si_9H_{12}) and v-trench ($Si_{23}H_{24}$) clusters.*

		ClCN1	ClCN2	ClCN3	SiNC	SiCN
1-Dimer		-44.7	-202.3	-289.4	-365.3	-397.9
V-trench	1	-49.0	-203.7	-287.9	-366.0	-398.7
	2	-51.6	-204.0	-288.3	-366.6	-399.1

Unlike the triple-dimer cluster, there are almost no cluster size effects in the case of a v-trench cluster. Table III-11 displays the adsorption energies for the stable configurations of ClCN adsorbed on a single-dimer and a v-trench clusters. In the last case there are two possible adsorption sites and, therefore, two dissociation pathways parallel to the dimer bond (Fig. III-9). It is seen that the energy difference between the analogous structures is quite small. This supports the conclusion about negligible effect of electron density delocalization across the dimer row.

C.3. Two-molecule adsorption

C.3.1. On a double-dimer cluster

The adsorption of the second ClCN molecule on a double-dimer cluster is also studied. In Table III-12 the energy values for the different adsorption modes are listed. Rows show the adsorption structure of the first molecule and columns – of the second

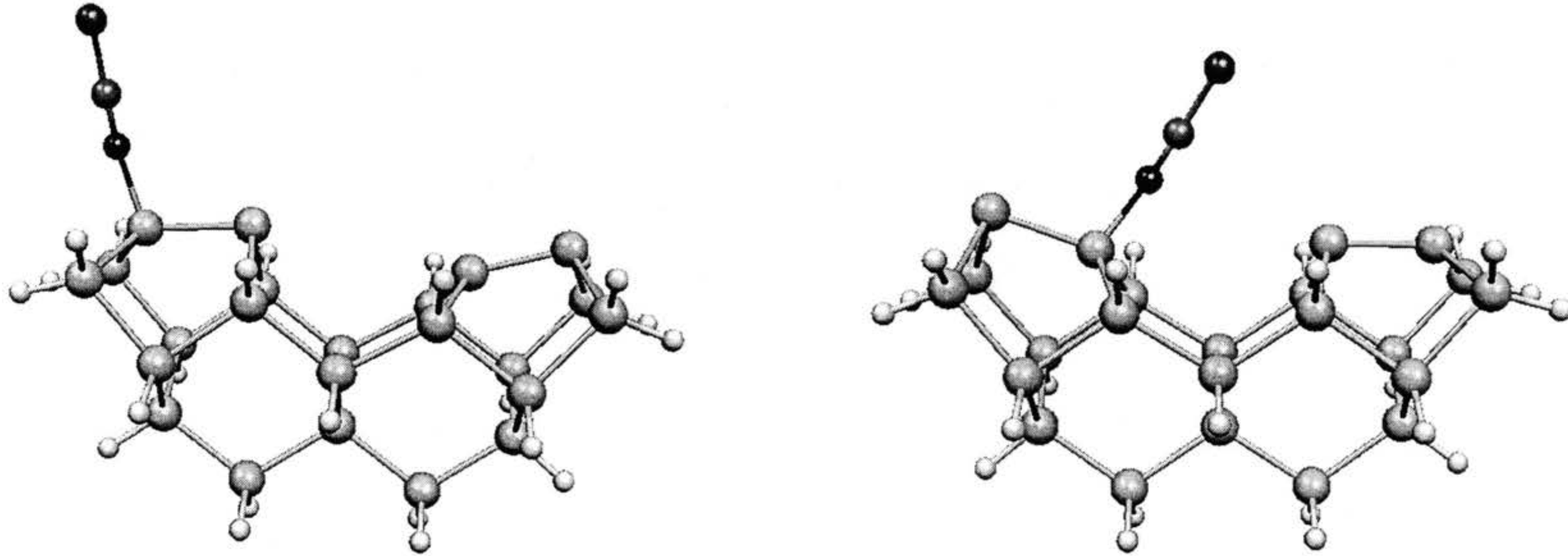

Figure III-9. Two possible configurations for molecular ClCN adsorbed on a v-trench cluster.

one. It is seen that for all side-on and dissociated states the energy values are almost identical. The only difference exists in their initial adsorption energy (ClCN1 end-on mode). When one ClCN molecule is in an end-on position the adsorption of the second molecule occurs with the energy value smaller than the original one by 9.3 kJ/mol. However, when the first molecule is in side-on or dissociated configuration the adsorption energy value increases. The most energetically favorable configurations for the adsorption of the second ClCN molecule are the dissociated SiNC2a and SiCN2a structures in which Cl and CN species are attached to different dimer bonds (Fig. III-10). Positive value of adsorption energy in the case of 1ClCN1 can be explained by repulsion of two ClCN molecules adsorbed on the same side of a cluster and the nucleophilic nature of the corresponding Si atom of the second dimer bond due to the fact that two dimer bonds are buckled in the opposite directions.

Since all one-molecule dissociation pathways lead to the formation of SiCN1 structure the dissociation pathway for a second ClCN molecule adsorbed on a structure with the Cl and CN dissociated species attached to the adjacent Si-Si bond was calculated. This was done in order to figure out the influence of the dissociated species on the process of adsorption of the second molecule. An example of such a pathway is given in Fig. III-11. It is seen from the data (Table III-12) that for the end-on adsorption configuration on a structure with Cl and CN dissociated species the magnitude of the adsorption energy is 20-30 kJ/mol higher than that on a bare double-dimer cluster. This supports the idea that adsorption and dissociation of one molecule increases the probability of adsorption of the second molecule on the neighbor site. On the other hand, relative energies for the corresponding second molecule side-on and dissociated states as

well as for their transition states (Table III-13) do not differ very much from the energy values of the corresponding ClCN single-molecule adsorption structures (Fig. III-12).

C.3.2. On a triple-dimer cluster

Lateral adsorbate-adsorbate interactions were also studied for two ClCN molecules adsorbed on a triple $Si_{21}H_{20}$ cluster. As it was shown before, the cluster size effects significantly change the energy of the system only in the case of the end-on structure. Therefore, the adsorption energies of four different molecularly adsorbed ClCN1-ClCN1 configurations on a triple-dimer cluster were calculated (Fig. III-13). Table III-14 contains the adsorption energies values for these structures. As in the case of a double-dimer cluster, the adsorption energy of the second molecule is determined by the charge distribution on the surface. For 1ClCN1-ClCN1 and 4ClCN1-ClCN1 configurations the adsorption energy values are smaller than those for corresponding one-molecule structures by 56.9 and 36.2 kJ/mol respectively. It occurs since the second dative N-Si bond is formed with the Si atom that is nucleophilic in nature because of the dimer bonds buckling and subsequent charge distribution unfavorable to such modes of adsorption. On the other hand, the energy difference for 2ClCN1-ClCN1 and 3 ClCN1-ClCN1 are 19.9 and 9.7 kJ/mol. It can be said that adsorbed molecule not only “poisons” the site on the same side of adjacent dimer bond but has also some “long-distance effects” attenuating, however, with the increase of the distance from the adsorbed ClCN molecule.

C.3.3. On a v-trench cluster

The possible two-molecule end-on adsorption structures for a v-trench cluster are shown in Fig. III-14. The corresponding energy values are listed in Table III-15. In 1ClCN1-ClCN1 configuration both ClCN molecules are adsorbed on the "buckled-down"

Table III-12. *Calculated B3LYP/6-31G* adsorption energies (kJ/mol) for the second ClCN molecule adsorption structures on a double-dimer* $Si_{15}H_{16}$ *cluster. Rows indicate the adsorption configuration of the first ClCN molecule, columns – the mode of the second one.*

	Pathway	ClCN1	ClCN2	SiNC1	SiCN1
ClCN1	1	2.2			
	2	-53.5	-200.7		
ClCN2	1	-70.1	-199.7		
	2	-65.3	-200.3		
SiNC1	1	-69.8	-198.9	-360.1	-359.0
	2	-65.0	-198.8	-360.7	-359.9
SiCN1	1	-74.8	-198.0	-359.0	-389.6
	2	-66.1	-197.8	-359.9	-391.0
SiNC2	1	-132.1			
	2	-126.2			
SiCN2	1	-138.3			
	2	-128.8			

Table III-13. *Calculated B3LYP/6-31G* adsorption energies (kJ/mol) of the transition states for the second ClCN molecule adsorbed on SiNC1 and SiCN1 double-dimer* $Si_{15}H_{16}$ *cluster sites.*

Site	Pathway	TS1	TS2	TS4
SiNC1	1	-35.6	-5.8	-272.3
	2	-34.7	-5.9	-271.8
SiCN1	1	-37.9	-6.4	-271.4
	2	-36.0	-6.5	-270.8

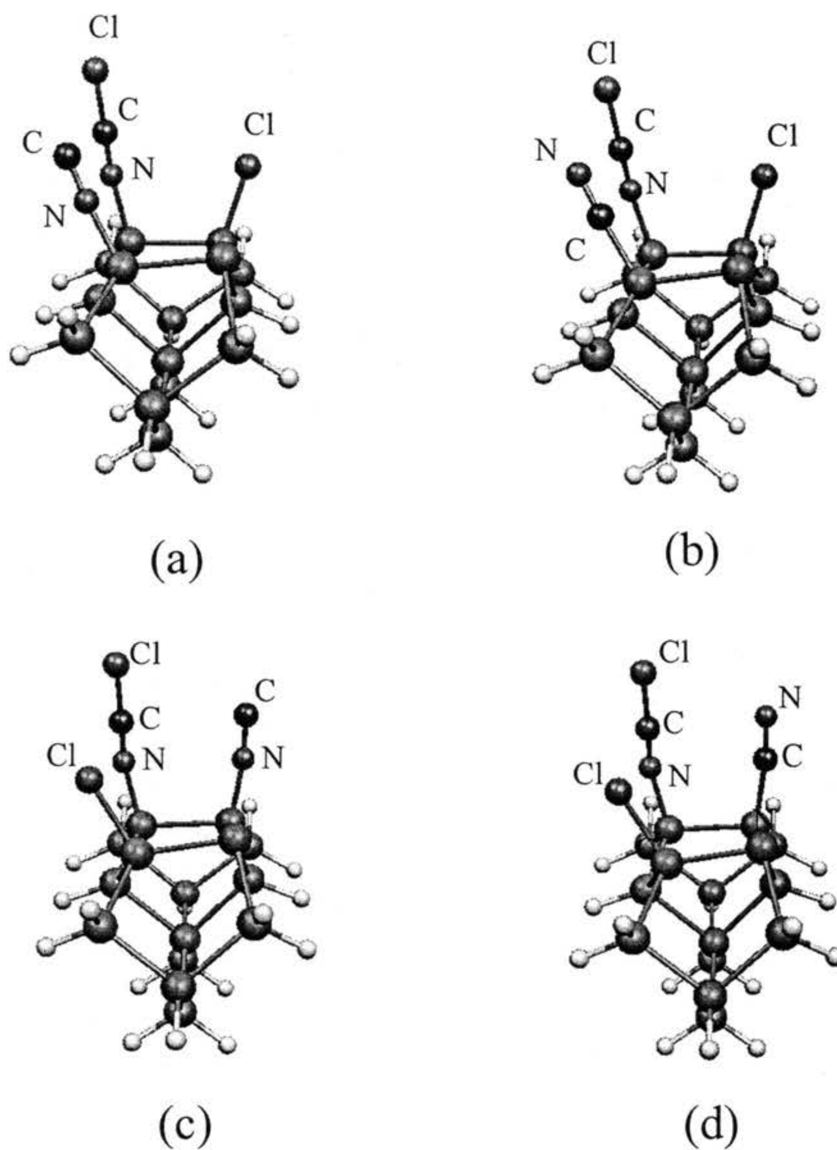

Figure III-10. Adsorption of the second ClCN molecule on double-dimer dissociated structures with the lowest values of adsorption energies: (a) 1ClCN-SiNC2 (b) 1ClCN-SiCN2 (c) 2ClCN-SiNC2 (d) 2ClCN-SiCN2.

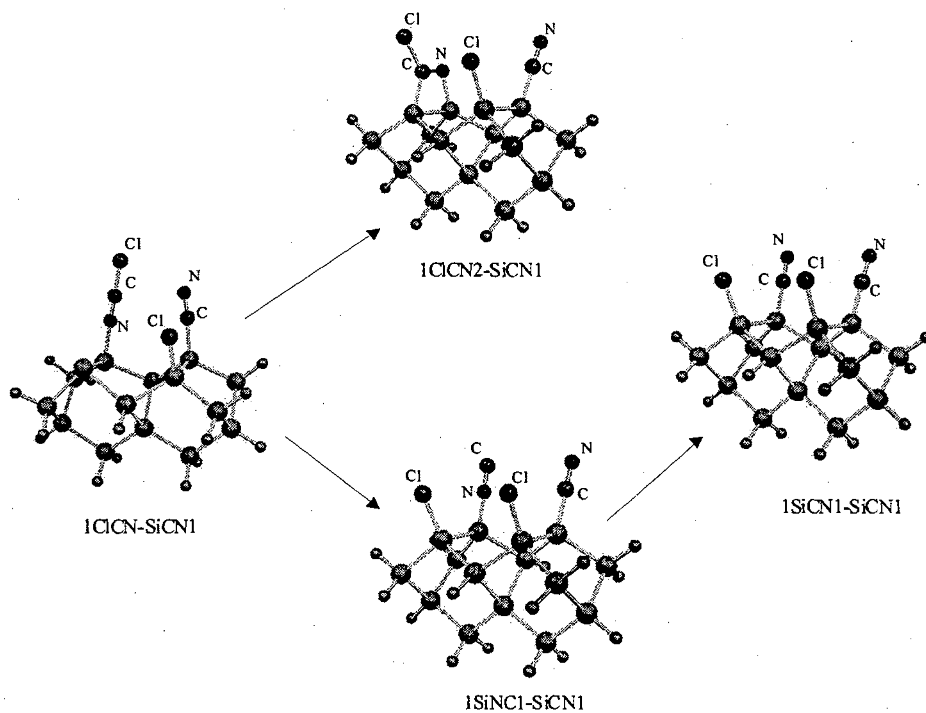

Figure III-11. Dissociation pathway for the second ClCN molecule adsorbed on a dissociated structure with Cl and CN species bound to the same dimer bond.

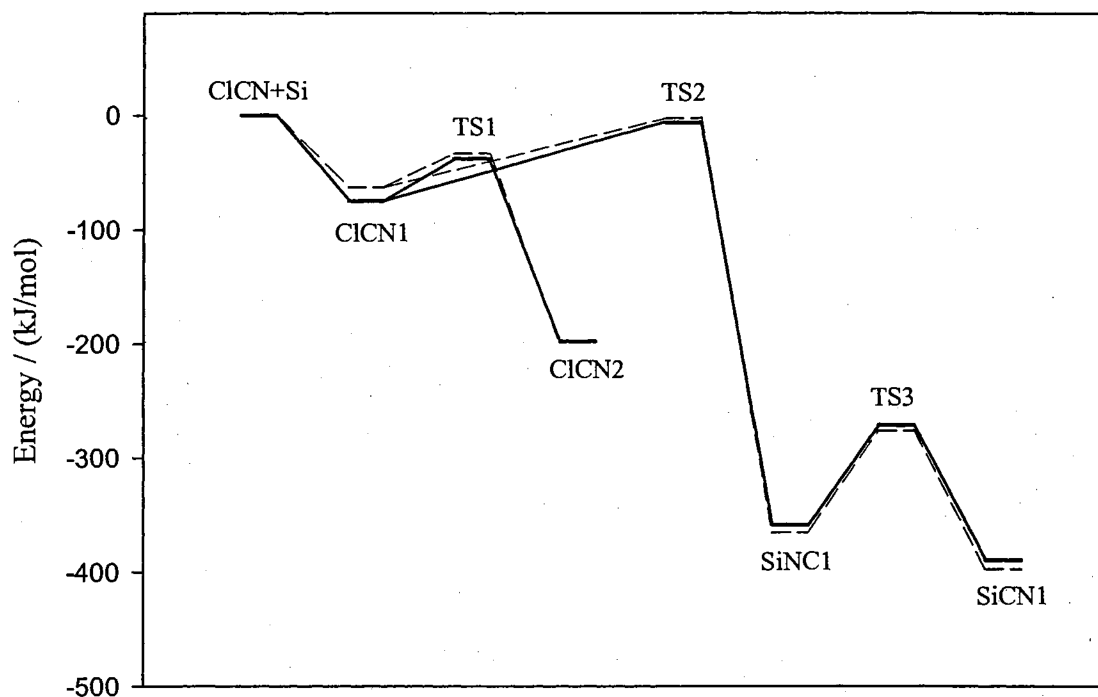

Figure III-12. Potential energy diagram for different adsorption modes corresponding to the dissociation of the second ClCN molecule on a double-dimer cluster with Cl and CN species bound to the same dimer-bond.

Table III-14. *Calculated B3LYP/6-31G* adsorption energies (kJ/mol) for the second ClCN molecule adsorption structures on a triple-dimer $Si_{21}H_{20}$ cluster.*

ClCN1	1ClCN1-ClCN1	2ClCN1-ClCN1	3ClCN1-ClCN1	4ClCN1-ClCN1
-72.5	-15.6	-52.5	-62.7	-36.3

positively charged Si atoms and adsorption energy of the second-molecule is almost equal to that of a one-molecule adsorption on v-trench cluster. Therefore, unlike double- and triple-dimer clusters, there is no "poisoning" effect across the dimer row for the electropositive silicon atom of the second row. In two other structures – 2ClCN1-ClCN1 and 3ClCN1-ClCN1 the adsorption energy of the second ClCN molecule is smaller than the first one by 19.9 and 35.6 kJ/mol correspondingly. This phenomenon can be explained by the fact that in these structures one ClCN molecule is attached to the nucleophilic "buckled-up" Si site. Besides that, in the case of 3ClCN1-ClCN1 there is a steric repulsion between two ClCN species, which significantly raises the energy of the whole configuration.

Table III-15. *Calculated B3LYP/6-31G* adsorption energies (kJ/mol) for the second ClCN molecule adsorption structures on a v-trench cluster.*

Pathway	ClCN1	1ClCN1-ClCN1	2ClCN1-ClCN1	3ClCN1-ClCN1
1	-49.0	-49.1	-31.7	
2	-51.6	-51.7		-13.4

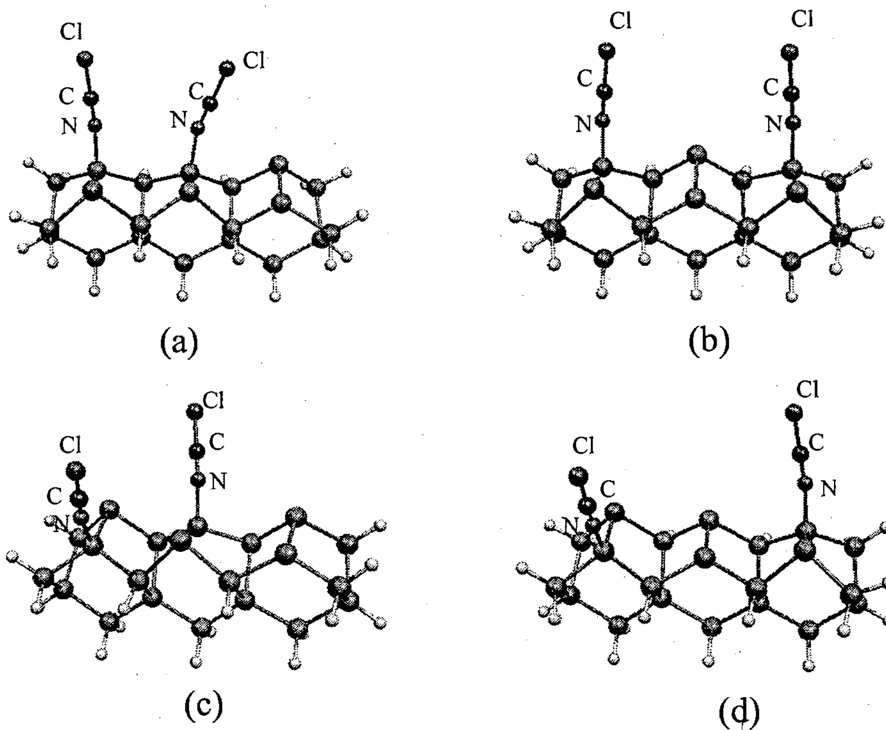

Figure III-13. Structures of two ClCN molecules adsorbed in an end-on position on a triple-dimer cluster: (a) 1ClCN1-ClCN1 (b) 2ClCN1-ClCN1 (c) 3ClCN1-ClCN1 (d) 4ClCN1-ClCN1

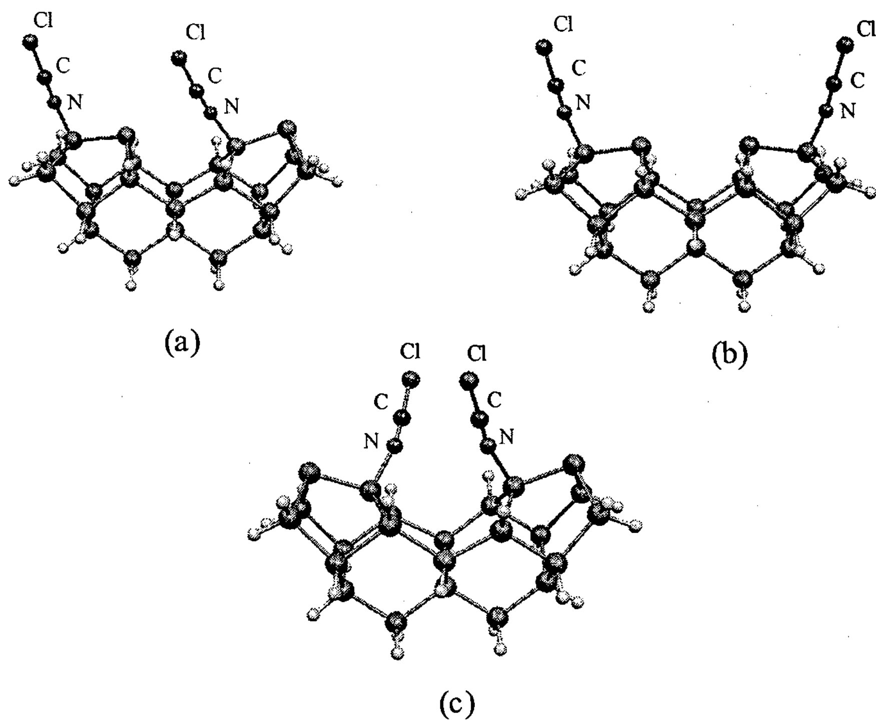

Figure III-14. Structures of two ClCN molecules adsorbed in an end-on position on a v-trench cluster: (a) 1ClCN1-ClCN1 (b) 2ClCN1-ClCN1 (c) 3ClCN1-ClCN1.

D. Conclusions

The adsorption and surface reactions of ICN, BrCN and ClCN on the Si(100)-(2x1) surface were studied using *ab initio* quantum calculations on single-, double- and triple-dimer clusters. These cyanogen halides can physisorb into an end-on molecular species that is bound through the N to the Si cluster via dative bond. The adsorption energy of this dative bonded species is sensitive to the cluster size, with the lowest energy obtained using a triple-dimer cluster. This species can further react to form either an adsorbed CN group with the N bond to the surface or a side-on intermediate by reacting across the Si-dimer bond. For ClCN, the energy of the transition state for the former process is close to that of the isolated molecule and cluster. The N bonded CN species can subsequently rotate to form a C bonded CN group. Of the two possible orientations, the C bonded species is found to have the lowest adsorption energy. Once the first barrier to form the N bonded CN species is overcome, no significant transition state barriers are present. The side-on intermediate can react to form an additional structure in which the halide-carbon bond is broken and the C end of the CN group inserts into the Si-dimer bond. This reaction is facilitated by the formation of both a strong XSi and a strong SiC bond. The insertion species can further react to form triple bonded CN species adsorbed through the N atom by recreating the Si-dimer bond. Finally, this newly created species can reorient itself to form a C bonded CN species. After the side-on species is formed from the dative bonded species, no significant barriers are present. Thus, for both pathways, the lowest energy structure is expected to form in agreement with experimental studies.

For ClCN adsorbed on Si double- and triple-dimer and v-trench clusters two main pathways perpendicular to the dimer bond are discovered. In both cases the transition barrier to form a side-on intermediate is lower than that for adsorption pathway parallel to the dimer bond. The adsorption energy is enough to overcome these barriers and reach eventually the mode with dissociated CN and Cl species on the surface. The configuration with Cl and CN species bound to the same dimer bond in a double cluster is lower in energy than that with Cl and CN attached to different Si-Si dimer bond and can be obtained from the latter by a Cl atom migration across the dimer bond through a low energy transition barrier. These pathways provide a possible explanation for not observing the side-on ClCN2 structure on the surface experimentally.

The energetics of the second-molecule adsorption strongly depends on the position and configuration of the first ClCN molecule, which in this case "poisons" certain adsorption sites. If the first ClCN molecule dissociates on the surface the adsorption energy of the second molecule increases comparatively to the energy corresponding to the adsorption energy of a single ClCN molecule on a bare cluster. In this case it occurs most easily on a structure with CN and Cl species bonded to different dimer-bonds. However, when both ClCN molecules are in the end-on position the adsorption energy value for the second molecule is lower than that for a bare cluster. It is mostly favorable when ClCN goes to the electropositive Si atom, determined by the buckling of the dimer bonds and corresponding charge distribution. The "poisoning" effect is negligible for the adsorption of the second molecule on the electrophilic site of the adjacent dimer row, however, it becomes more significant when it goes to the more adsorption unfavorable "buckled-up" site.

CHAPTER IV

TUNGSTEN TRIOXIDE AND ITS COLORED HYDROGEN BRONZES

A. WO_3 thin films and mechanisms of their coloration

Tungsten trioxide (WO_3) thin films and the corresponding tungsten bronzes (M_xWO_3, M=H, Li, K etc) are very well known substances due to their ability to reversibly change color from yellow (WO_3) to deep blue (bronzes) under the influence of some external parameters, such as temperature, irradiation or applied voltage.[1] This results in the possibility to use them in a variety of applications, which include gas sensors[2-4], "smart windows",[5,6] displays,[7,8] rear view mirrors.[9] The preparation techniques for WO_3 films include sputtering in $Ar+O_2$ plasma,[10-12] chemical vapor deposition,[13,14] plasma-enhanced chemical vapor deposition,[15] anodic oxidation,[16,17] sol-gel-derived films,[18-20] decomposition of oxalatotungstate compounds,[21] electro-deposition,[22] thermal oxidation[23] and hydrothermal treatment.[24] The structural properties, as well as optical and electrical behaviors of the film depend on the deposition method.

Different models were proposed to explain the optical adsorption in colored tungsten bronze thin films. Early work on the properties of the colored WO_3 formed by optical and electrical excitation suggested a model involving trapping electrons in oxygen ion vacancies.[25] It can be supported by the fact that as soon as the color centers have been bleached by heating in oxygen at high temperature they cannot be regenerated. A more favorable model involves intervalence charge transfer.[26]. The injected electrons in this

model are trapped at the tungsten sites and the optical adsorption is caused by the resonance transfer of the trapped electrons between the tungsten atoms. The third model suggests the formation of small polarons.[27,28] This theory offers a possibility to formulate a quantitative explanation for the optical absorption. Small polarons are formed when electrons polarize their surroundings, so that localization of the wavefunction takes place. A small overlap between wavefunctions corresponding to adjacent sites, as well as strong disorder is conducive to polaron formation.[28] This model uses a local structural distortion brought about by the electron trapping and W^{5+} formation. This lowers the energy of the occupied state relative to the unoccupied state of the surrounding W^{6+}. There is a very good agreement between theory and experiment for the spectral optical density of tungsten oxide films. It is comparable to the results obtained from the intervalence charge transfer theory.[26,29]

The schematic bandstructure explaining the optical absorption of tungsten bronze films is shown in Figure IV-1. In the transparent state, the Fermi level lies between the O *2p* and the t_{2g} bands. When tungsten oxide is reduced to bronze the Fermi level is shifted upwards and populates the lower part of the t_{2g} band with excess electrons. The material starts to exhibit absorption.

B. Reduction of tungsten oxide to colored bronzes

B.1. Thermochromic coloration

Thermochomism is the ability of WO_3 to change its optical property while varying the temperature. Tungsten oxide films turn blue when heated in vacuum at T~300°C for 15 min and get bleached while being subjected to heat treatment at

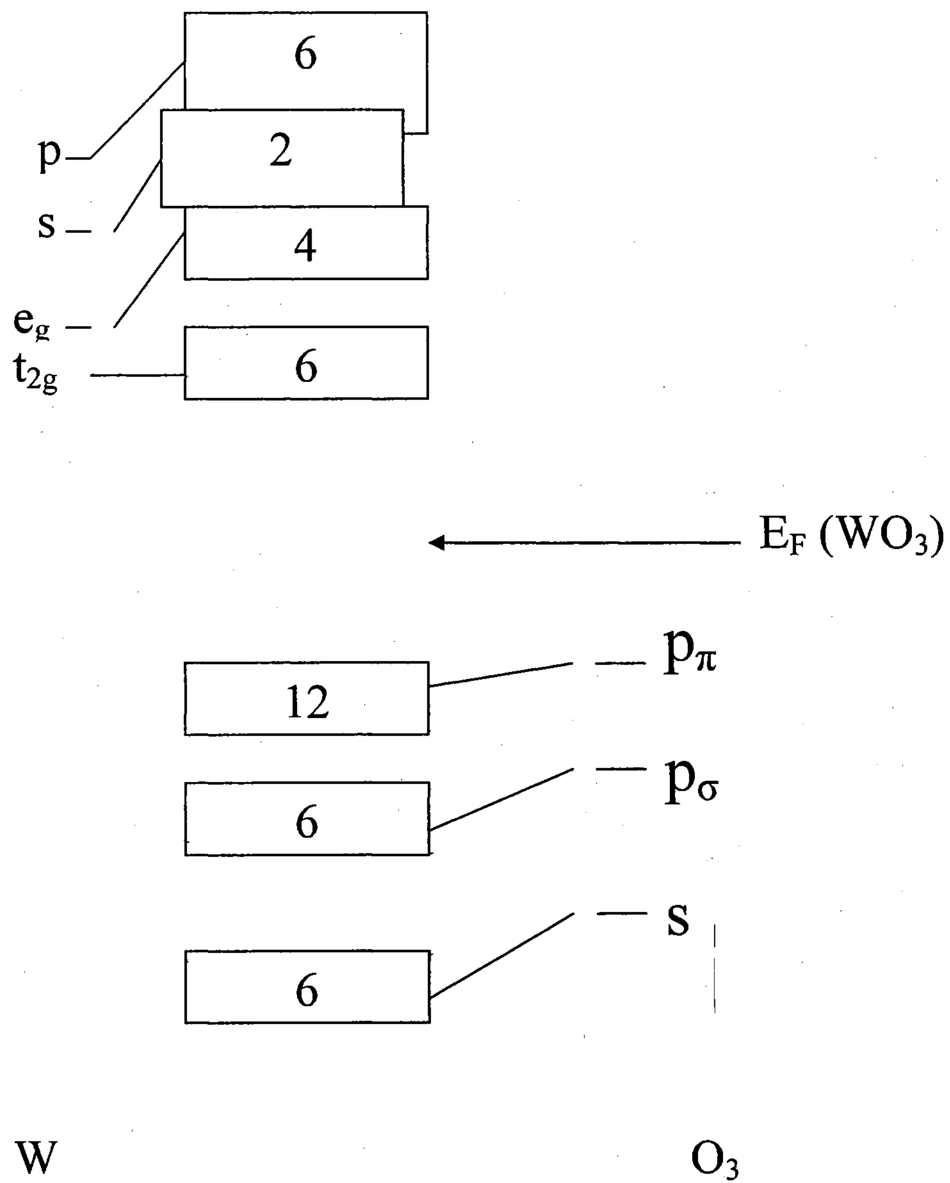

Figure IV-1. Schematic bandstructure for WO_3 defect perovskite structure. Adapted from Ref. 32.

T~450°C for 1.5 h.[30] The mechanism of thermal coloration was related to increasing the oxygen deficit in vacuum due to desorption of oxygen in the form of O^+ [31] and increasing negative surface charge of the density of surface state. Oxidizing annealing of colored films in the air reduces the surface charge back to zero.[30] Thermochromic coloration was also studied at lower temperatures. Color change was observed while annealing WO_3 films in vacuum at T>80°C.[33] The equation describing the oxygen loss and consequent color change at high temperatures in vacuum is as follows:

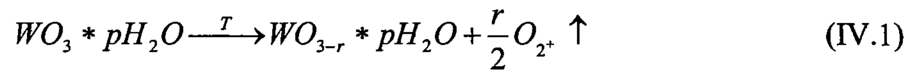

$$WO_3 * pH_2O \xrightarrow{T} WO_{3-r} * pH_2O + \frac{r}{2} O_{2^+} \uparrow \qquad \text{(IV.1)}$$

where p may vary.[32]

B.2. Photochromic coloration

Photochromism is the reversible absorption change caused by film exposure to different types of irradiation accompanied by regaining the original properties without irradiation. For tungsten oxide various results on its coloration by UV illumination are reported.[10,25,33-39] The photochromic behavior of tungsten oxide depends on different parameters including the film density and its thickness. However, the surrounding medium is also of a great importance. For example, the photochromic response considerably increases in the presence of the vapors of hydrogen-containing compounds.[40-44] It is also found that the bleaching is strongly affected by the presence of oxidizing agents such as ozone or hydrogen peroxide.[25] The UV-induced coloration process may be described with the equation:[33]

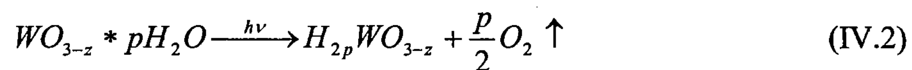

$$WO_{3-z} * pH_2O \xrightarrow{h\nu} H_{2p}WO_{3-z} + \frac{p}{2} O_2 \uparrow \qquad \text{(IV.2)}$$

In a typical optical absorption spectrum of a tungsten oxide film before and after UV irradiation a broad absorption band with a maximum at 900-1000 nm is usually seen, exhibiting almost the same optical profile as those colored by other techniques. After an irradiation of approximately 200 days, a saturation of absorbance is observed for the films with different thickness (from 400 to 700 nm).[34]

The coloration of the films with thickness between 300 and 1000 nm also depends on their composition, especially on the hydrogen and oxygen contents. Gerard *et al.*[10,36] distinguish between different ranges for the H_xWO_y thin films. At high oxygen deficiency the films have a metallic aspect and do not change their properties after UV irradiation, whereas at $y>2.65$ UV illumination induces a strong blue color and also changes the electrical conductivity.

B.3. Electrochromic coloration

Electrochromism is the property of thin films to change color due to an applied potential and change back to the original state by a potential reversal. The electrochromic reaction of WO_3 is usually described by a double injection of a proton and an electron in the tungsten oxide films:

$$WO_3 + xH^+ + xe^- \leftrightarrow H_xWO_3 \quad (IV.3)$$

Despite the fact that the assumptions of this model are not verified,[36] the change in optical properties of the tungsten oxide films is usually attributed to the electron insertion or extraction (which means that the term xe^- is the dominating factor in the equation (IV.3)). The data on electrochemical coloration of tungsten oxide films using the method of cyclic voltammetry are extensively reported.[5,16,26,45-54] The experiments were

performed in acidic (2M HCl or H_2SO_4) solution with Ag/AgCl electrode as a reference. The sample consisted of a glass/ITO/tungsten oxide electrode and a platinum sheet was taken as a counter electrode. The films were characterized by measuring their transmittance T and current i while changing the potential U on the working electrode.

Electrochromism of tungsten oxides provides the opportunity to measure the diffusion coefficients D of colored tungsten bronzes. It is shown that D varies both with hydrogen content[55,56] and deposition parameters as well as the density of the films.[57] The measurement of D is carried out with the help of a chronoamperometric technique. The relationship between current i and time, from which D can be estimated, is governed by the following formula:[58]

$$\ln i(t) = -\frac{\pi^2 Dt}{2d^2} + const \quad \text{(IV.4)}$$

Where d is the film thickness. For amorphous tungsten oxide films a value $D=5.5\times10^{-10}$ cm^2/s was obtained. In different electrochemical experiments the reported values of D lie in the range of 1.5×10^{-9} – 3×10^{-12} cm^2/s for approximately 500-nm-thick WO_3 films deposited by evaporation with densities between 3.38 and 5.84 g/cm^3.[53,57]

B.4. Gasochromic coloration

Gasochromism is the property of WO_3 to change color as result of its reduction by different types of gases. Due to this property tungsten oxide can be used in manufacturing gas sensors. Studies on the formation of tungsten bronzes from the interaction of WO_3 with H_2,[59-61] H_2S,[62] NO_2,[4] SO_2,[63] NH_3,[64] gases have been carried out. For the reactions with hydrogen gas the catalyst (Pd, Pt, Rd) should be applied on the tungsten oxide surface in order to reduce the activation barrier for the reaction.[32] The coloration intensity

is proportional to the partial pressure of the gas. The mechanism of gasochromic tungsten oxide reduction involves dissociation of H_2 molecules at the surface of catalyst, rapid diffusion of hydrogen to the metal/tungsten oxide interface, followed by a creation of the dipole layer. This dipole layer results in a field across the interface, producing a sharp potential drop, which, in turn, lowers the energy of the conduction band edge with respect to the Fermi level.[65]

The reaction of WO_3 with other gases (like H_2S or NO_2) can be described in the following way. Presence of the species in the gas phase reduces oxidized donor centers in the oxide film, which liberates electrons near the conduction band of the film. These donor centers were identified by XPS as W^{5+} sites (oxygen vacancies). The Fermi level shift was also observed.[66] Formation of tungsten bronze upon decomposition of hydrogen-containing gases is also possible.

C. Bleaching of hydrogen tungsten bronzes

Tungsten bronzes normally get bleached by the reaction with oxygen gas. In this case the protons in the H_xWO_3 films are oxidized to H_2O. When tungsten bronze is oxidized in air the rate of the oxidation is very slow and it may take several tens of hours to decolorize the blue tungsten bronze thin film completely.[67] For the films with catalyst on the surface the process of oxidation is much faster. For example, in the case of Pt-impregnated H_xWO_3 thin films, exposed with humid O_2 (20%)/Ar mixture the complete decolorization of the film took about 20 min.[68]

The bleaching of tungsten bronzes can be also achieved by using other oxidizing reagents. Kikuchi *et al.* studied the kinetics of decolorization of H_xWO_3 thin films in

aqueous $Fe_2(SO_4)_3$ and H_2O_2 solutions by means of UV-Vis spectroscopy.[39] The analysis of the results included solving the diffusion equations taking into account the surface reaction of oxidation agent with H_xWO_3. The decolorization process was found to be nearly exponential due to the non-adiabatic nature of the surface reaction between the film and the oxidizing agent. The rate-determining step is the surface reaction for a wide range of concentration of the oxidizing agent. The total bleaching time for this case may lie in the region from 10 seconds to several minutes.

Hydrogen tungsten bronze can also react with tetrachloromethane resulting in the formation of chloroform.[69] It interacts as well with chloroform and methylene chloride. The kinetic studies of reduction of nitro-containing compounds with powder tungsten bronzes are ongoing in Dr. Allen Apblett's research group at Oklahoma State University. This research has possible application in detecting and decapacitating explosives.

D. Structural properties of WO_3 and its bronzes

Tungsten trioxide crystals have perovskite-type atomic configurations ("ReO_3 type") based on corner-sharing WO_6 octahedra (Fig. IV-2). Deviations from the ideal cubic perovskite-type structure occur due to antiferroelectric displacements of W atoms and to mutual rotations of oxygen octahedra. Since the magnitude of distortion depends on the temperature, at certain temperatures phase transitions may occur. There are three stable allotropic varieties of WO_3, in which the lattice is distorted to monoclinic, orthorhombic or tetragonal symmetry. The monoclinic to orthorhombic transition occurs at 330°C, whereas the orthorhombic symmetry becomes tetragonal at 770°C. The volatility of WO_3 above 1200°C does not allow identification of a high-temperature cubic

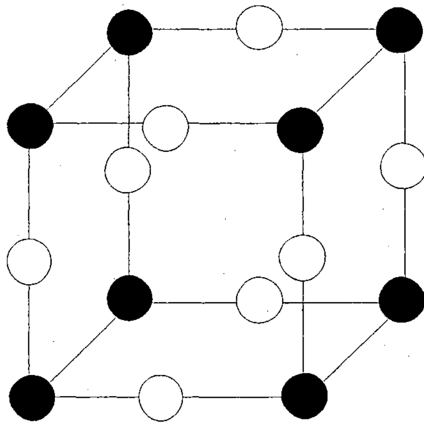

Figure IV-2. The cubic “ReO_3 type” structure of WO_3. Adapted from Ref. 71.

form. The overall composition can be written as WO_{3-z}, where $z>0$.[70]

At room temperature WO_3 is usually monoclinic with lattice parameters a=7.30 Å, b=7.53 Å, c=3.85 Å, β=90.88°.[72] However, if tungsten oxide hydrate ($WO_3 \cdot 2H_2O$) is annealed to 300°C it assumes a metastable cubic form, c-WO_3.[73] The relative stability of the cubic phase is in correlation with the presence of some kind of impurities. In another experiment with powder tungsten acid hydride the cubic phase was observed at 200°C.[74] The initially amorphous tungsten oxide films begin to crystallize after annealing to 390°C and completely adopt a crystalline phase after 450°C.[75]

The crystalline structure of H_xWO_3 bronzes depends on the density of H species added to a WO_3 host. The covalent WO_3 arrays consist of tungsten-occupied oxygen octahedra which are distorted or regular. The W-O-W angles may vary creating a series of channels in which H atoms can be inserted. The gradual insertion hydrogen produces an evolution of structure types similar to that caused by an increase of temperature. The distortions decrease in magnitude as the concentration of hydrogen increases. Three main phases for hydrogen tungsten bronze are found. There are reports about an orthorhombic phase at $x=0.1$,[70] whereas the tetragonal phase is formed at $x=0.23$ and $x=0.33$.[76,77] Finally, when $x \geq 0.5$ cubic tungsten bronze is obtained.[78]

CHAPTER V

PREPARATION AND CHARACTERIZATION OF POLYCRYSTALLINE TUNGSTEN BRONZE THIN FILMS

A. Introduction

This chapter discusses the preparation and characterization of tungsten bronze thin films. First, WO_3 films were prepared by thermal oxidation of sputter deposited tungsten metal. Then those got reduced by Zn/HCl system or direct hydrogenation in a UHV chamber. The characterization of the films was done by means of various techniques including XPS, UPS, SEM, UV-Vis and XRD. The structures of tungsten oxide and corresponding bronze have been determined; the bronze composition was compared to that in a powder form. The electronic bandstructure analysis of obtained WO_3 and H_xWO_3 films is also done.

B. WO_3 thin films preparation

B.1. Sputter deposition of W-films

Tungsten thin films were prepared by sputter deposition in a UHV (10^{-6} torr) chamber of metallic W (99.95% purity, A.D. Mackay, Inc.) on 2×0.6 cm quartz substrates. The deposition was carried out by ionization of argon gas and subsequent bombardment of W target with Ar^+ ions. The ejected W species from the target surface in

turn got deposited on the quartz substrate rotating with a constant velocity. The rate of deposition was measured using a microbalance Maxtek TM-400. The actual thickness of the W film is calculated by the following formula:

$$L(t) = \int_0^t \frac{1}{2} * F * \left|\cos(\alpha + \frac{2\pi}{T} * t')\right| dt' \qquad (V.1)$$

where F is the deposition rate (Å/s), α is the initial angle between the W species flux and the normal to the substrate, T is the period of rotation of the substrate (s) and t is the time of deposition (s). The coefficient 0.5 comes from the fact that only one side of the substrate gets deposited. Since t>>T the influence of the initial angle value α on L is negligible. If the deposition rate F is constant, the simplification of equation (V.1) leads to the following expression:

$$L(t) = 0.318 \times F \times t \qquad (V.2)$$

Here L is linearly proportional to the time of deposition.

B.2. Oxidation of W-films

Tungsten films were converted into WO_3 films by oxidation of W in a continuous stream of oxygen at 400°C for 3 hours according to the equation:

$$W + 3/2 O_2 \rightarrow WO_3 \qquad (V.3)$$

The resulting thickness of the films was calculated regarding the difference in density between W and WO_3. From (V.3) it follows that

$$n(W) = n(WO_3) \qquad (V.4)$$

Here n is the number of moles of a given compound per unit area. Equation (V.4) is equivalent to:

$$\frac{L(WO_3)\times \rho(WO_3)}{M(WO_3)} = \frac{L(W)\times \rho(W)}{M(W)} \tag{V.5}$$

where L is film thickness; ρ is density of the material and M is molecular weight of a corresponding compound. Knowing the thickness of tungsten film L(W) the thickness of tungsten oxide film can be calculated according to the formula:

$$L(WO_3) = \frac{L(W)\times \rho(W)\times M(WO_3)}{M(W)\times \rho(WO_3)} \tag{V.6}$$

Substituting the values for corresponding molecular weights and densities and taking into account equation (V.2) the following expression for the WO_3 film thickness is obtained:

$$L(WO_3)=1.027\times F\times t \tag{V.7}$$

Here F is the deposition rate from (V.1) and t is time of deposition (s).

B.3. Reduction of tungsten oxide into tungsten bronze

Two methods of reduction of WO_3 to the bronze were used: chemical reduction in aqueous solution and direct exposure of H atom in a UHV chamber at high temperatures.

B.3.1. Chemical reduction in aqueous solution

The reduction of tungsten oxide in Zn/HCl system was done according to the procedure described in Ref. 79. WO_3 thin films were immersed into the aqueous suspension of zinc powder in which concentrated HCl acid was slowly added. The reduction of tungsten oxide to bronze was due to hydrogen evolved in the reaction:

$$Zn + 2HCl \rightarrow ZnCl_2 + H_2 \tag{V.8}$$

The H_xWO_3 films were taken out of the reaction medium when they turn completely dark blue.

B.3.2. Direct hydrogen exposure in a UHV chamber

The WO_3 films were loaded into the UHV chamber described in Chapter II. Then the films were exposed with atomic hydrogen obtained by splitting molecular hydrogen with a hot filament for 3.5 hours. The temperature of the sample was recorded to be 369K. The pressure of hydrogen in the chamber was equal to 1×10^{-5} torr. As a result stable blue H_xWO_3 films were obtained.

C. Characterization of WO_3 and H_xWO_3 thin films

C.1. XRD and SEM

XRD spectra were taken by Scintag XDS 2000 difractometer using copper K_α radiation. In Figure. V-1 the XRD spectrum for a pure W-film is shown. Since this spectrum contains only one broad peak with FWHM=6°, the structure of a sputter deposited tungsten film can be considered microcrystalline. After thermal oxidation it assumes a polycrystalline phase (Fig. V-2). The spectrum corresponding to WO_3 can be attributed to a cubic phase. Such metastable configuration may arise in aqueous tungsten oxides after their annealing to higher temperatures[73]. The lattice parameter a=3.7507 Å.

H_xWO_3 XRD spectrum also reveals a cubic crystalline structure (Fig. V-3), corresponding to the bronzes with amount of hydrogen $x\geq0.5$. Analogous results were obtained for the bronzes prepared by refluxing WO_3 with iso-butanol for 12 hours[78]. The lattice parameter of such bronzes was equal to 3.700 Å.

SEM micrograph of a WO_3 film with thickness 210 nm is shown in Figure V-4. The structure can be characterized as polycrystalline with islands formation. The average size of a grain is estimated to be about 100 nm.

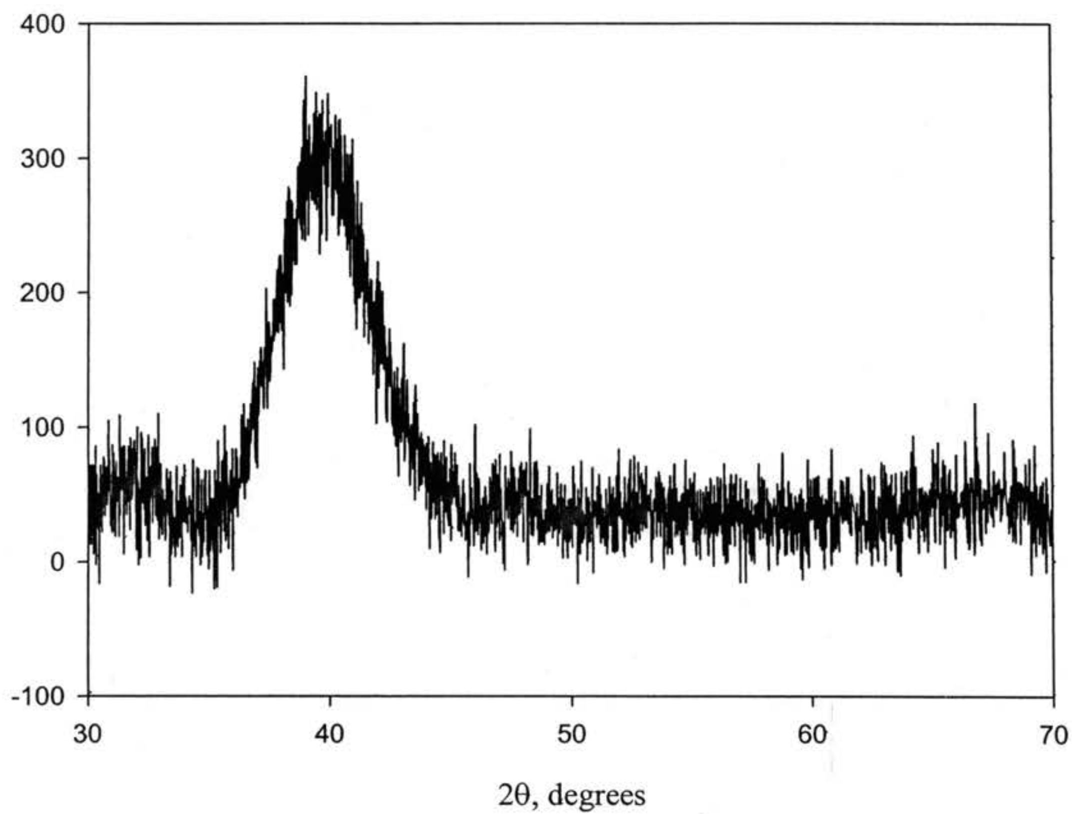

Figure V-1. XRD spectrum of a microcrystalline tungsten thin film.

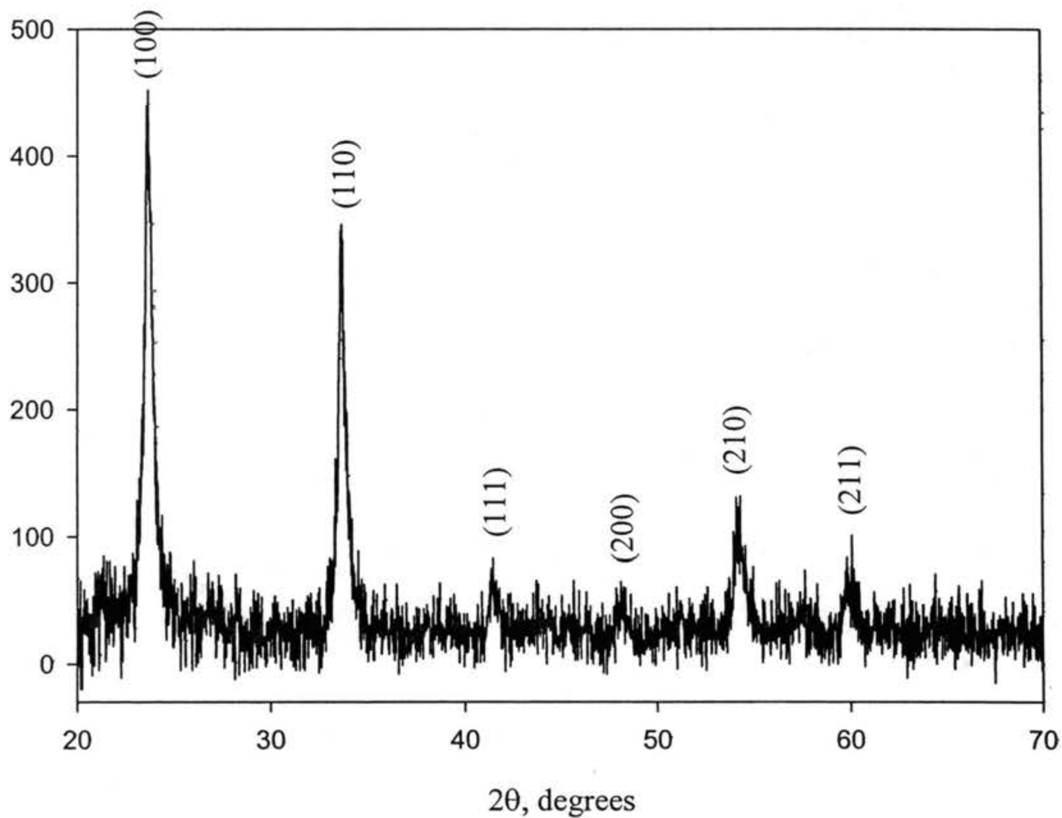

Figure V-2. XRD spectrum of a WO_3 thin film. Lattice has a cubic structure with a=3.7507 Å.

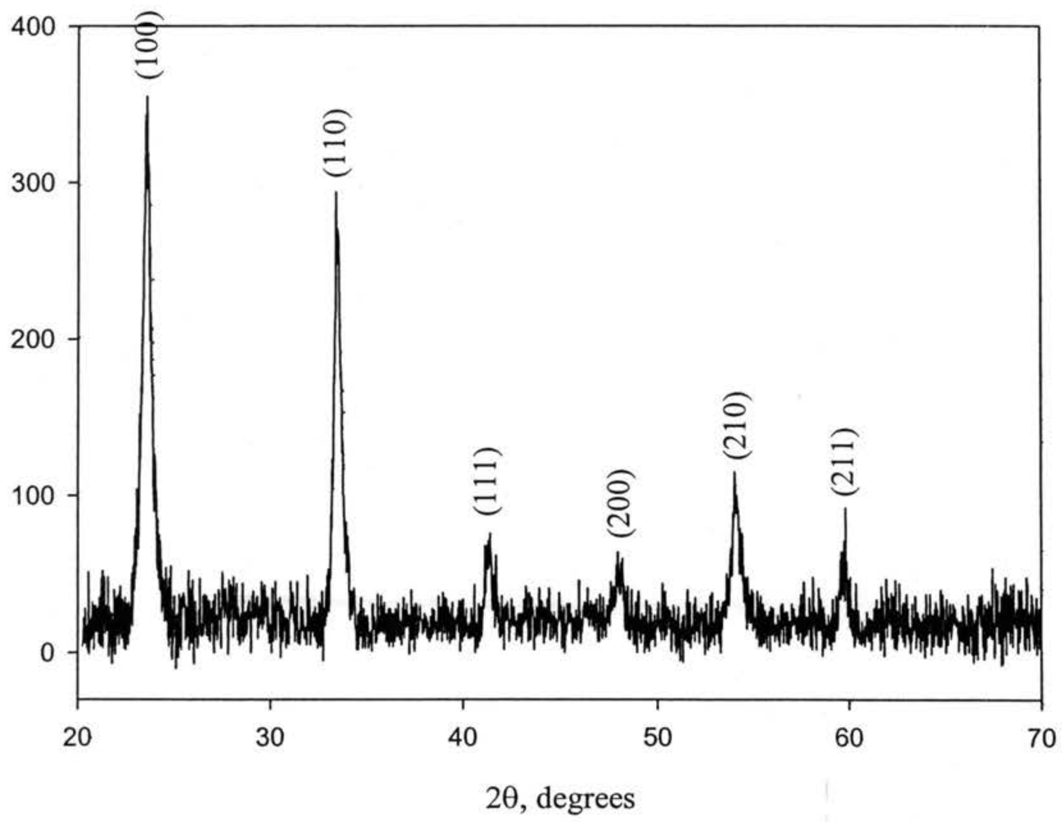

Figure V-3. XRD spectrum of a hydrogen tungsten bronze thin film.

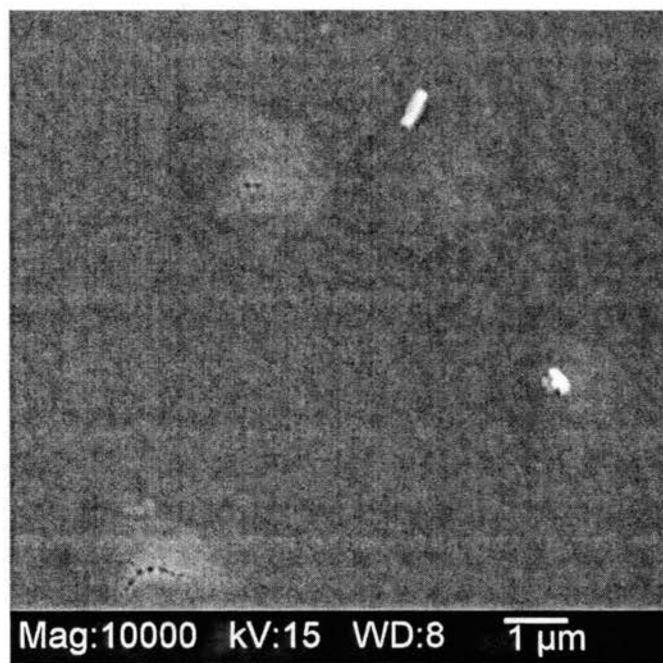

Figure V-4. SEM-micrograph of a 210 nm WO_3 film.

C.2. XPS.

The XPS spectrum of a typical WO_3 film hydrogenated in a UHV-chamber is shown in Figure. V-5. Three peaks attributed to W are clearly seen: a doublet W 4*d* at 261.3 eV and 246.4 eV and a broad peak at 35 eV corresponding to the splitting between $4f_{7/2}$ and $4f_{5/2}$ levels. Besides that a strong peak at 530.5 eV attributed to O 1*s* is also shown. The two peaks at 743 eV and 764 eV can be identified as oxygen KLL Auger peaks which is consistent with the data in the Ref. 80. The spectra of WO_3 thin films are practically indistinguishable from those for WO_3 in a powder form.

The deconvoluted W 4*f* peak for non-hydrogenated WO3 is given in Figure V-6. The Gausian-Loretzian fitting was used for the analysis. Photoelectron binding energies were calibrated with respect to C 1*s* peak centered at 284.6 eV. This peak consists of a doublet due to spin-orbit splitting between $4f_{7/2}$ and $4f_{5/2}$ levels. The separation of peaks in a doublet is constant and equal to 2.15 eV. The doublet corresponds to a $4f_{7/2}$ line with binding energy 34.3 eV, which results from the presence of W^{6+} species in a film.[80] XPS O 1*s* spectrum for a WO_3 film is given in Figure V-7. Its main component is centered at 529.7 eV and is attributed to oxygen in a WO_3 film. Another small peak at 531.7 eV results from the presence of water bound in the film structure as well as water molecules adsorbed on the film surface.[81]

In the tungsten bronze film H_xWO_3 three doublet components in W 4*f* deconvoluted spectrum are observed (Fig. V-8). The first doublet with $4f_{7/2}$ at 33.6 eV corresponds to W^{6+} oxidation state analogous to that in WO_3. The second (32.9 eV) and third (30.9 eV) ones are believed to be due to the presence of W^{5+} and W^{4+} states, correspondingly. The relative amounts of tungsten species in hydrogenated and non-

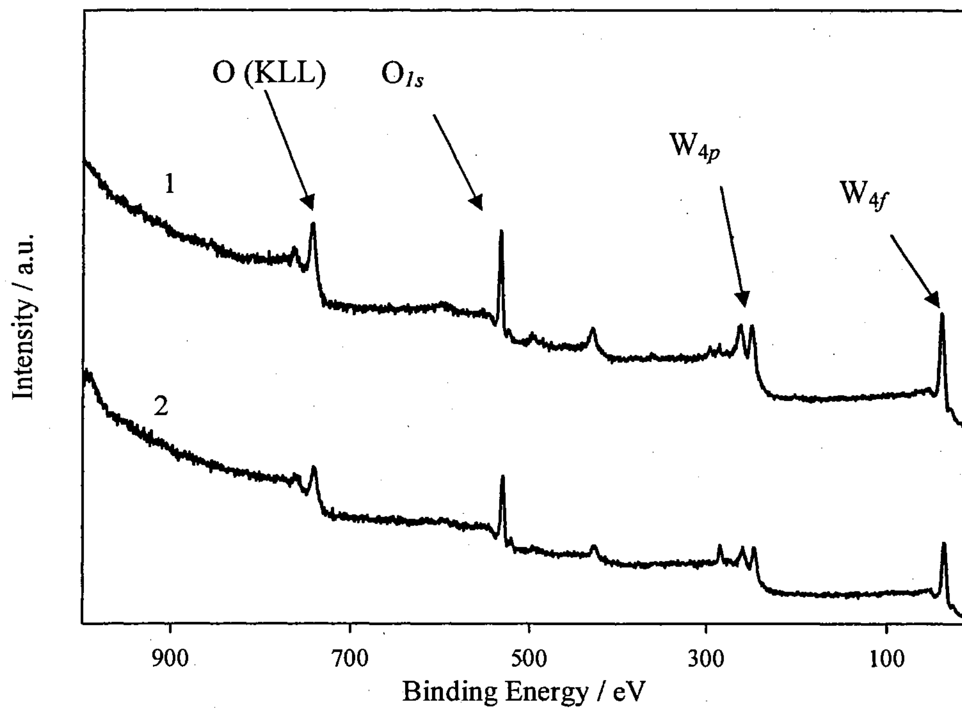

Figure V-5. XPS spectra of (1) a H_xWO_3 thin film (2) H_xWO_3 in a powder form.

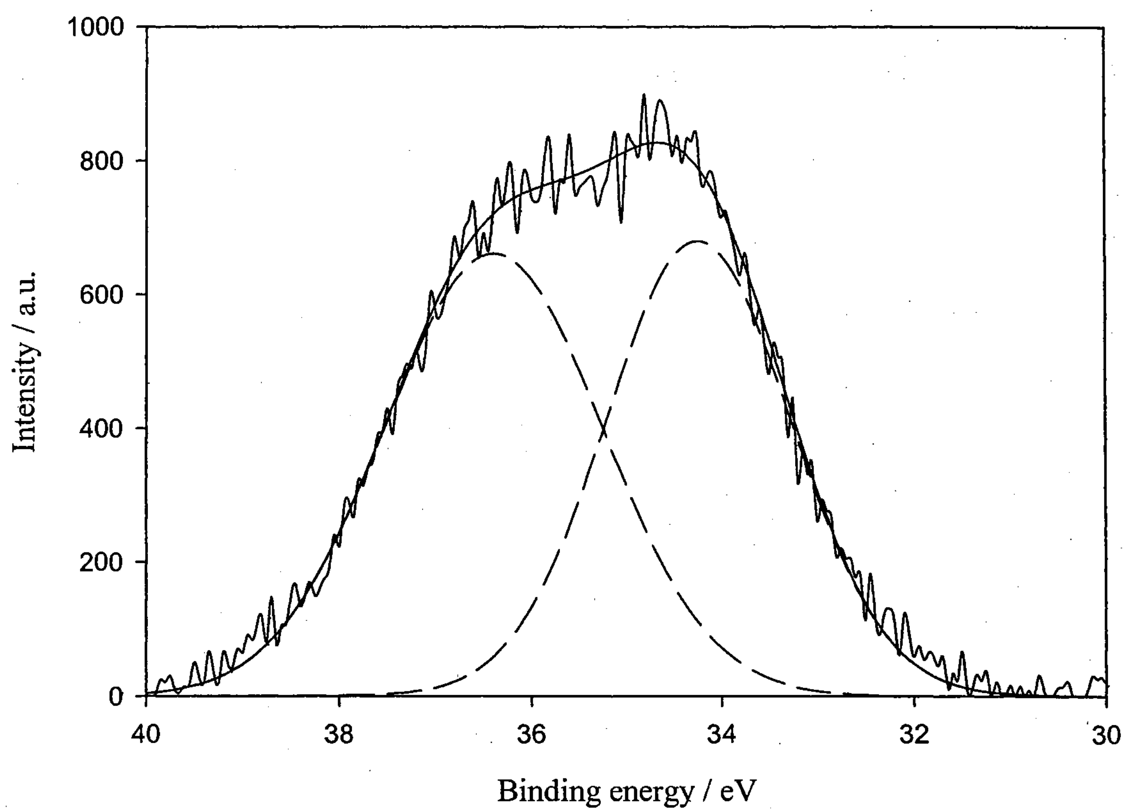

Figure V-6. XPS spectrum and deconvolution curves for W 4*f* peak in a non-hydrogenated WO_3 film.

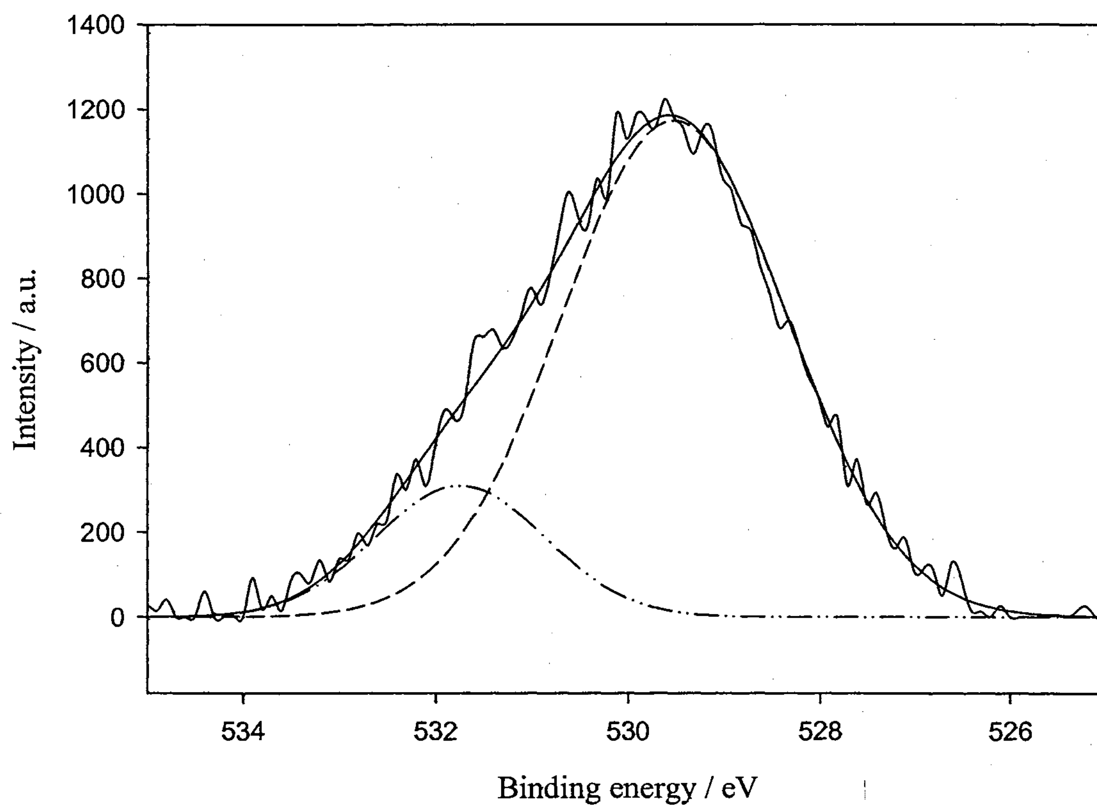

Figure V-7. XPS spectrum and deconvolution curves for O 1*s* peak in a non-hydrogenated WO_3 film.

Table V-1. *Relative amounts (%) of different tungsten oxidation states in non-hydrogenated and hydrogenated WO_3 thin films.*

	W^{6+}	W^{5+}	W^{4+}
WO_3	100	—	—
H_xWO_3	38.5	38.0	23.5

hydrogenated films are given in Table V-1.

The higher binding energy constituent in O 1*s* XPS spectrum for H_xWO_3 film (Fig. V-9) has significantly greater intensity comparing to the analogous peak for the non-hydrogenated WO_3 spectrum. This is consistent with the formation of additional O-H bonds in the process of hydrogenation.

C.3. UPS and UV-Vis

UPS studies have been done for tetragonal WO_3 as well as for tetragonal and cubic tungsten bronzes.[23,71,82-84] Pure single crystal WO_3 is characterized by a broad peak appearing at about 7.5 eV.[23] The position of the top of the valence band for amorphous tungsten oxide is 4.1 eV, whereas for polycrystalline one it is 3.65 eV.[83] Reduction of WO_3 to bronze results in broadening of the valence band peak and appearance of the additional small peak near the Fermi level, which is believed to be due to partial filling of the conduction band in the process of bronze formation.[23] In Fig.V-10 the UPS spectra of non-hydrogenated WO_3 film and H_xWO_3 one are shown. In contrast to the results for tetragonal WO_3, the UPS spectrum for cubic tungsten oxide obtained by thermal oxidation of W does not contain any peaks in the region from the Fermi level to 14 eV.

Nevertheless, after reduction to bronze a broad peak with the maximum at 10 eV appears. Similar to tetragonal tungsten oxide, this peak can be assigned to the presence of extra electrons in the valence band and shifting the Fermi level to higher energies. The intensity of the peak for the bronze obtained by hydrogenation in the UHV chamber is much higher than that for the film obtained by chemical reduction in Zn/HCl medium, which testifies about deeper surface penetration and more robust structure obtained by the first method.

UV-Vis spectra of WO_3 film and tungsten bronze film, produced by chemical oxidation in Zn/HCl medium (Fig. V-11) consistently show the extra optical band appearing at λ=1000 nm in the case of bronzes. This wavelength corresponds to the band energy 1.2 eV and can be interpreted as presence of electrons in the lower conduction band. Similar results are obtained for tungsten bronzes prepared by other methods.[27,61,75,85-87]

D. Conclusions

Hydrogen tungsten bronze thin films were prepared by the method consisting of two steps. First, tungsten oxide films were produced by sputter deposition of tungsten on a quartz substrate with subsequent thermal oxidation in a stream of gaseous oxygen. Second, those films were reduced either by direct hydrogen gas exposure in an ultra-high vacuum chamber or by chemical reaction with hydrogen evolving in a Zn/HCl reaction medium. Both tungsten oxide and bronzes obtained by this method possess cubic polycrystalline crystalline structure with lattice parameter a=3.7507 Å. This cubic

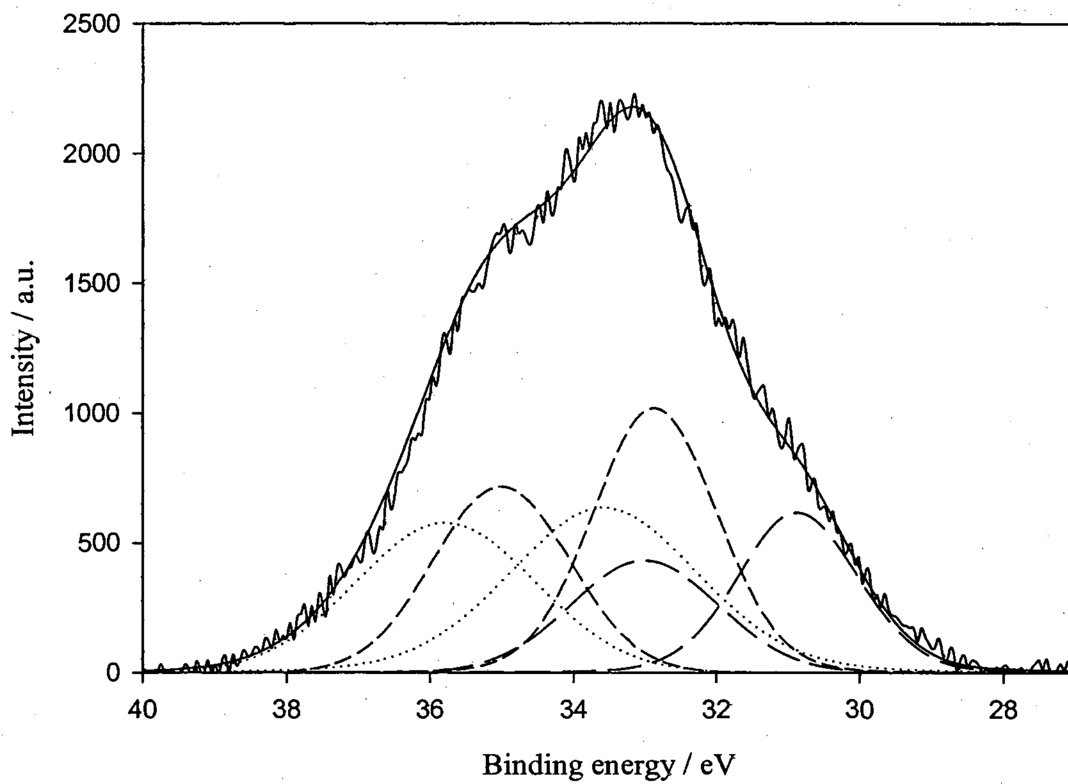

Figure V-8. XPS spectrum and deconvolution curves for W 4*f* peak in a hydrogenated H_xWO_3 film.

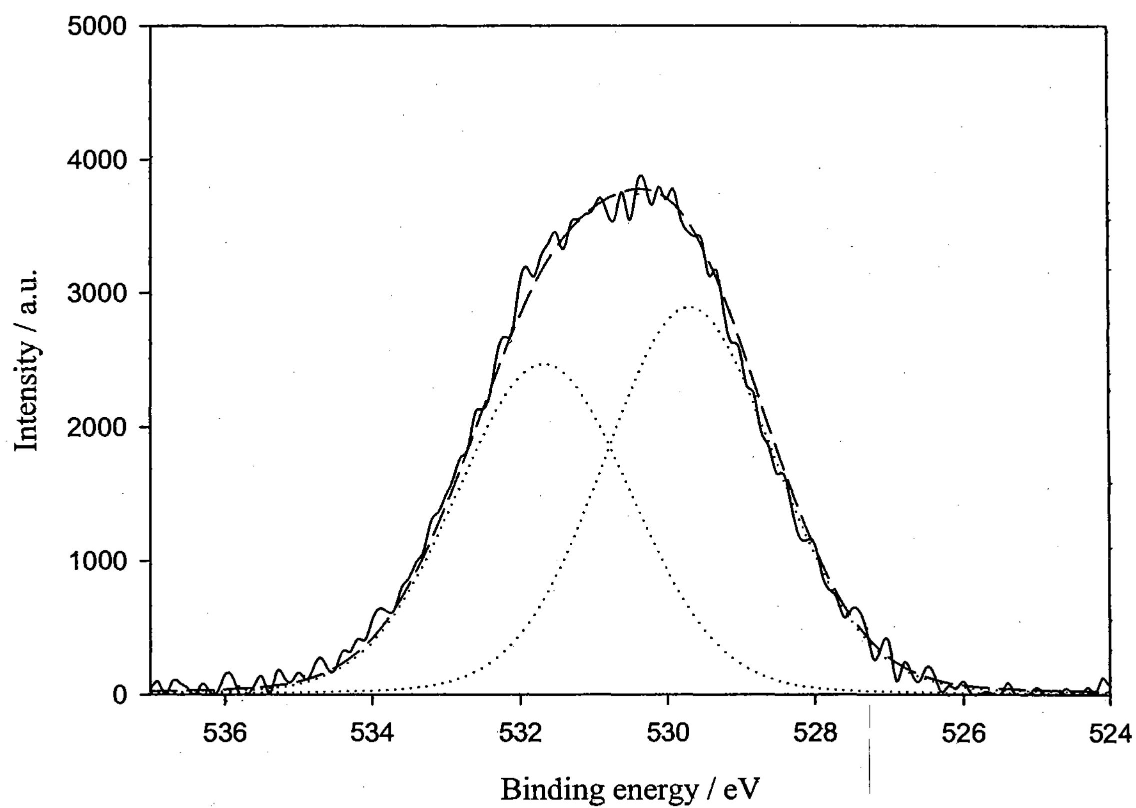

Figure V-9. XPS spectrum and deconvolution curves for O 1*s* peak in a hydrogenated H_xWO_3 film.

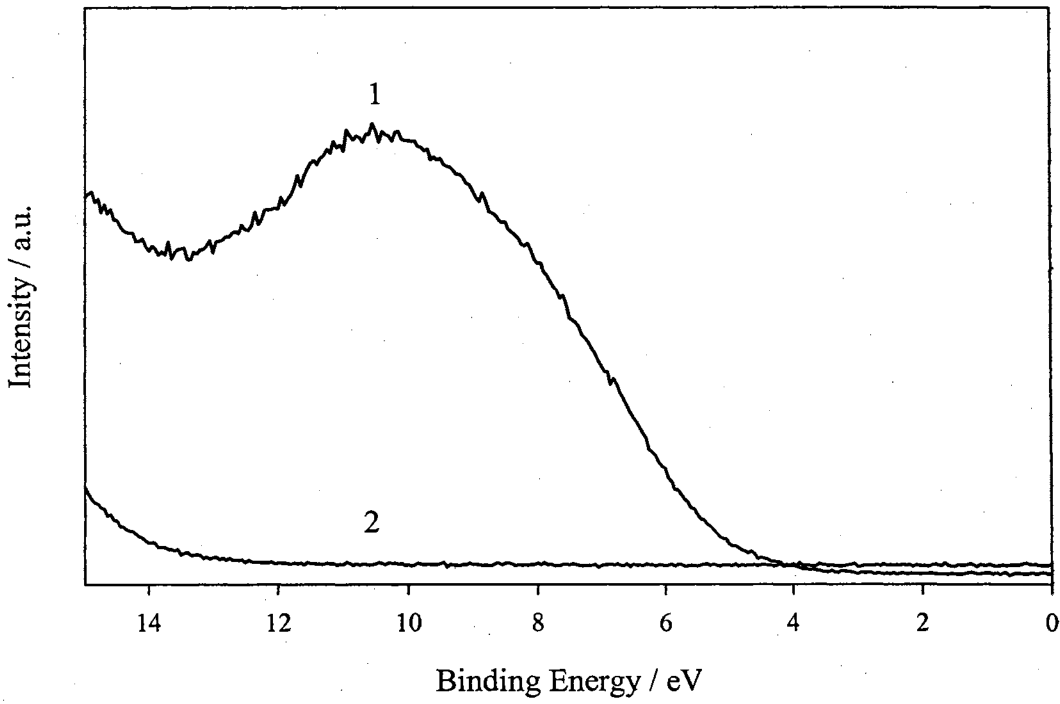

Figure V-10. UPS spectra of (1) a H_xWO_3 film (2) a non-hydrogenated WO_3 film.

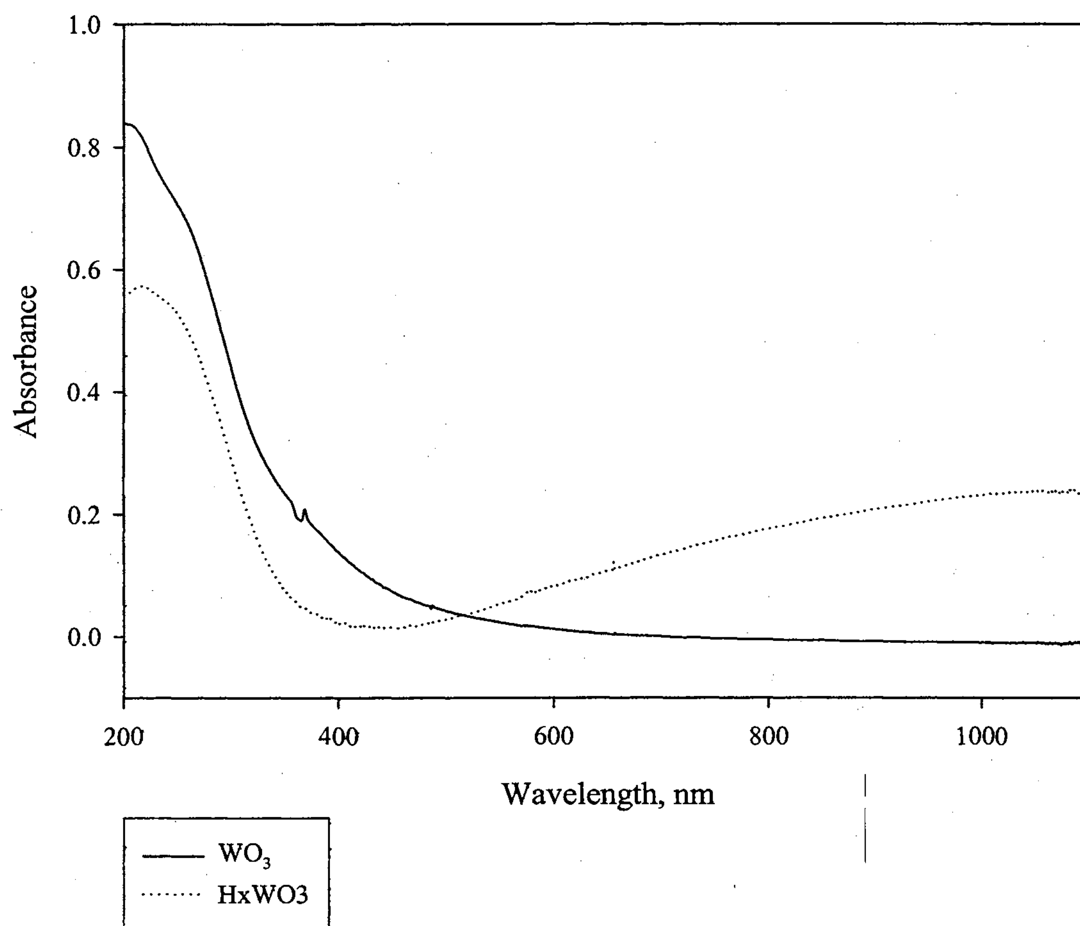

Figure V-11. UV-Vis absorbance spectra of 30 nm WO_3 and H_xWO_3 thin films.

structure corresponds to hydrogen tungsten bronzes with the formula H_xWO_3, where $x \geq 0.5$. While in pure tungsten oxide W^{6+} dominate, tungsten bronzes contain three types of species: W^{6+}, W^{5+} and W^{4+}. The change of optical properties in the process of WO_3 reduction is related to the shift of Fermi level to higher energies and partial population of the lower conduction band.

CHAPTER VI

KINETICS OF OXIDATION OF TUNGSTEN BRONZE THIN FILMS WITH NITROBENZENE

A. Introduction

Kinetics of the reaction between tungsten bronze thin films and nitrobenzene is studied in this chapter. The whole process can be described by the following equation:

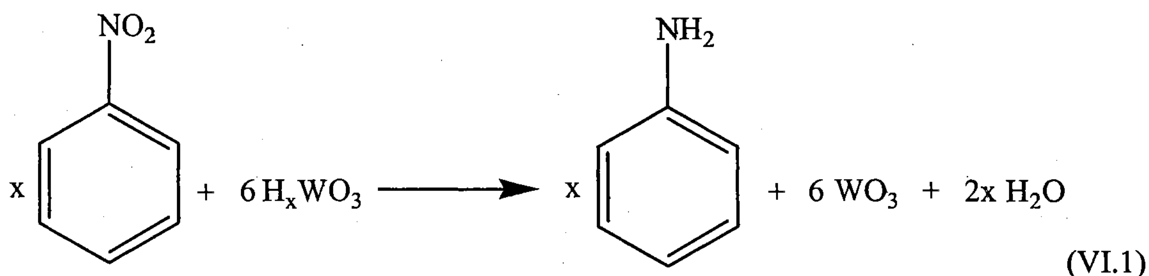

(VI.1)

The studies are done with the help of UV-Vis spectroscopy. Two series of experiments have been carried out. In the first one the concentration of nitrobenzene is held constant whereas the tungsten bronze film thickness is varied. In the second series the reaction rate dependence of concentration of nitrobenzene is measured while the film thickness remains intact. As a result, the values of diffusion coefficient and reaction constant are determined.

B. Experimental

The kinetics of oxidation of tungsten bronze films with nitro-containing organic substances was studied with DMS-200 Spectrophotometer having a beam size 2×8 mm.

The measurements of absorbance intensity at constant wavelength 900 nm were taken at different time intervals. The absorbance intensity of the samples is related to the concentration of hydrogen species in the film C according to the Beer's law:

$$I = ALC + I_0 \tag{VI.2}$$

Where A is an absorbance coefficient, L is a thickness of the film and I_0 is a non-zero adsorption intensity of a non-hydrogenated WO_3 sample. The intensity dependencies of time for the films with different thicknesses are shown in Fig. VI-1. The data are fitted quite well with the exponential relationship:

$$I = ae^{-bt} + I_0 \tag{VI.3}$$

where b is inversely proportional to the relaxation time of the film. From fitting this expression into the experimental data the value of the reaction rate b can be obtained.

C. Kinetic model

C.1. Oxidation of tungsten bronze thin films

Since absorbance intensity is proportional to the total number of incorporated hydrogen in the tungsten bronze film, the diffusion of hydrogen atoms from the bulk to the surface must be taken into account. The diffusion equation corresponding to the Fick's law looks as follows:

$$\frac{\partial C_H(x,t)}{\partial t} = D\frac{\partial^2 C_H(x,t)}{\partial x^2} \tag{VI.4}$$

Here $C_H(x,t)$ is the proton concentration as a function of two variables: coordinate along the film thickness (x) and time (t); D is a diffusion coefficient. Since the reaction takes place only on one side of the film and hydrogen atoms cannot diffuse into the quartz

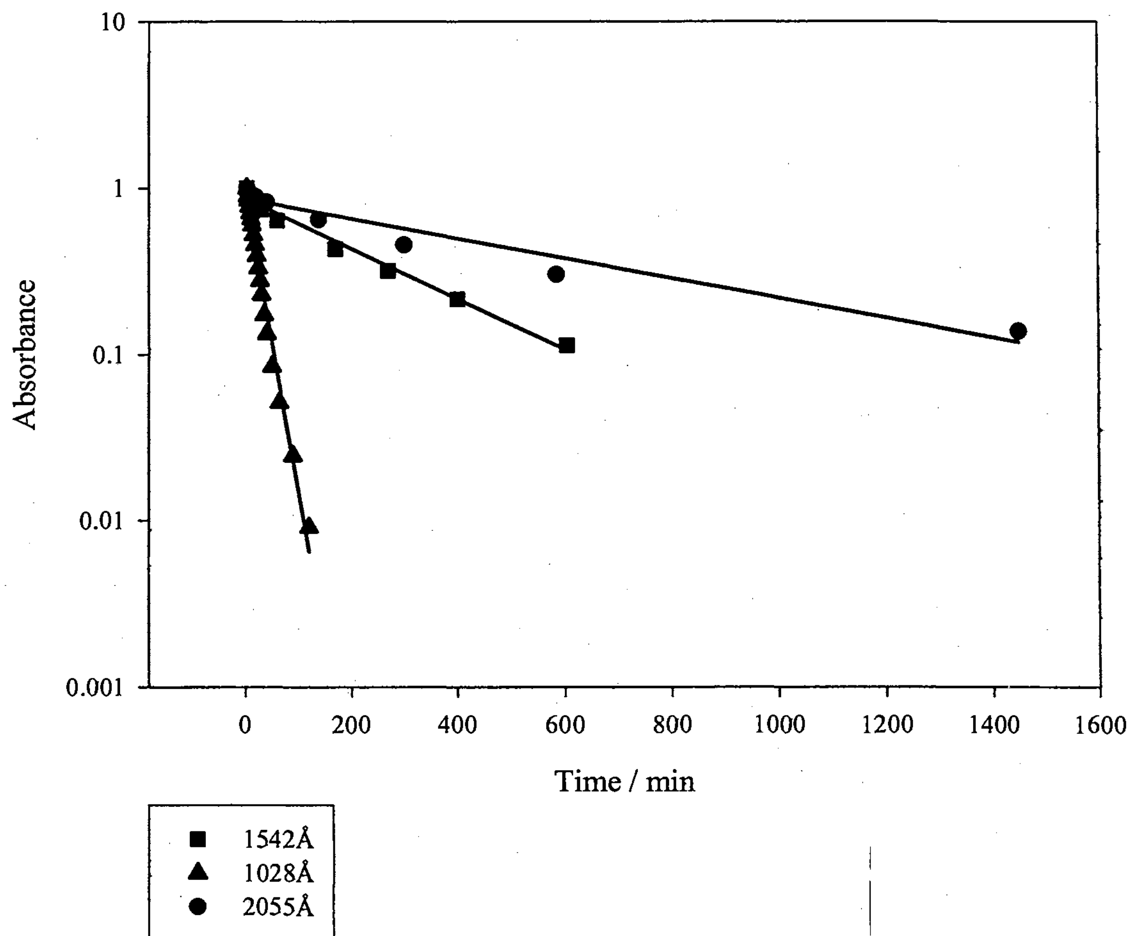

Figure VI-1. Oxidation kinetics of H_xWO_3 thin films of different thickness in 0.1M solution of nitrobenzene in Hexanes.

substrate at room temperature, the first boundary condition will be:

$$\frac{\partial C_H(x,t)}{\partial x}\Big|_{x=0} = 0 \quad \text{(VI.5)}$$

The second boundary condition reflects the second order reaction between the oxidant and the surface hydrogen:[39]

$$D\frac{\partial C_H(x,t)}{\partial x}\Big|_{x=L} = kS\theta_{ox}C_H(x,t) \quad \text{(VI.6)}$$

where L is the thickness of the film, k is a reaction constant, θ_{ox} is the surface coverage of the oxidizing agent, S in the total number of surface sites. The initial condition is:

$$C_H(x,t) = C_0 \text{ at } t=0 \quad \text{(VI.7)}$$

since at the very beginning the concentration of protons is assumed to be uniform along the film thickness. Solving this equation for $C_H(x,t)$ produces the following result:[88]

$$C_H(x,t) = 2C_0 k' \sum_{m=1}^{\infty} \frac{\cos(\lambda_m x)}{\left[\left(k'^2 + \lambda_m^2\right)L + k'\right]\cos(\lambda_m L)} e^{-D\lambda_m^2 t} \quad \text{(VI.8)}$$

where $k' = \frac{kS\theta_{ox}}{D}$ and λ_m's are the roots of the equation

$$\lambda \tan(\lambda L) - k' = 0 \quad \text{(VI.9)}$$

Fig. VI-2 shows the distribution of proton concentration in a sample with thickness L changing with time. Since the absorbance intensity is proportional to $C_H(x,t)$ integrated over the thickness of the film, the time dependence of the total hydrogen concentration will be:

$$C'(t) = A\int_0^L C_H(x,t)dx = 2C_0' k'^2 \sum_{m=1}^{\infty} \frac{1}{\lambda_m^2[(k'^2 + \lambda_m^2)L + k']L} e^{-D\lambda_m^2 t} \quad \text{(VI.10)}$$

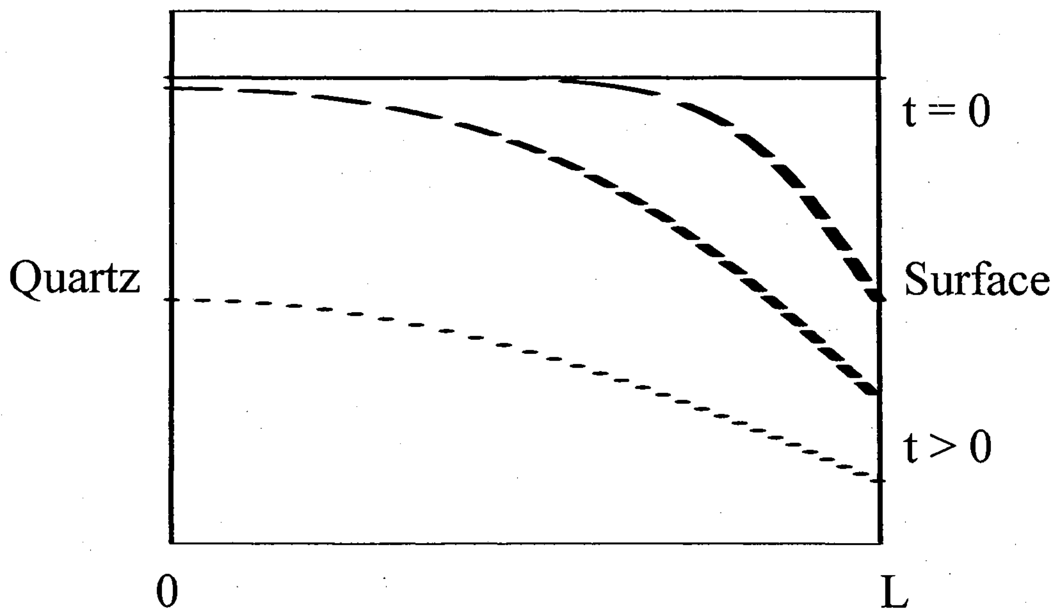

Figure VI-2. Time dependent proton concentration distribution in a tungsten bronze film with thickness L.

where $C_0' = A\int_0^L C_0 dx = C_0 LA$, A is the beam surface area.

Equation (VI.10) corresponds to the exponential form of the dependence *I(t)* (Fig. VI-1). The second-order equation for the kinetics of hydrogen concentration change looks as follows:

$$-\frac{dC_H}{dt} = \tilde{k} S\theta_{ox} C_H(L,t) \qquad \text{(VI.11)}$$

Here θ_{ox} is the surface coverage of nitrobenzene. Combining (VI.4), (VI.6) and (VI.11), the relationship between the second-order reaction constant $\tilde{k}$ and the constant k from the boundary condition (VI.6) will be:

$$\tilde{k} C_H(L,t) = -k\frac{dC_H}{dx}\Big|_{x=L} \qquad \text{(VI.12)}$$

From equation (VI.8) at $x=L$:

$$C_H(L,t) = 2C_0 k' \sum_{m=1}^{\infty} \frac{1}{\left[\left(k'^2 + \lambda_m^2\right)L + k'\right]} \times e^{-D\lambda_m^2 t} \qquad \text{(VI.13)}$$

And

$$\frac{dC_H}{dx}\Big|_{x=L} = -2C_0 k' \sum_{m=1}^{\infty} \frac{\lambda_m \tan(\lambda_m L)}{\left[\left(k'^2 + \lambda_m^2\right)L + k'\right]} \times e^{-D\lambda_m^2 t} \qquad \text{(VI.14)}$$

Approximating by taking just the first members of the series (VI.13) and (VI.14), the relationship (VI.12) becomes:

$$\tilde{k} = k\lambda_m \tan(\lambda_m L) \qquad \text{(VI.15)}$$

Using (VI.9), the equation (VI.15) transforms into:

$$\tilde{k} = \frac{k^2 S\theta_{ox}}{D} \qquad \text{(VI.16)}$$

$$\frac{\partial C_H}{\partial t} = D \times (\frac{\partial^2 C_H}{\partial r^2} + \frac{2}{r}\frac{\partial C_H}{\partial r}) \quad \text{(VI.21)}$$

where r ranges from 0 to R, R is a sphere radius. The boundary condition will be:

$$D\frac{\partial C_H}{\partial r}|_{r=R} = kS\theta_{ox}C_H \quad \text{(VI.22)}$$

and the initial condition is:

$$C_H(r,t) = C_0 \text{ at } t=0 \quad \text{(VI.23)}$$

The solution of (VI.21) in this case is:[88]

$$C_H(r,t) = \frac{2C_0 k'}{r}\sum_{m=1}^{\infty}\frac{R^2\lambda_m^2 + (Rk'-1)^2}{\lambda_m^2\left[R^2\lambda_m^2 + Rk'(Rk'-1)\right]}\sin(R\lambda_m)\sin(r\lambda_m)\times e^{-D\lambda_m^2 t} \quad \text{(VI.24)}$$

where λ_m's are the roots of the equation:

$$R\lambda\cot(R\lambda) + Rk' - 1 = 0 \quad \text{(VI.25)}$$

Approximating $\cot(x) \approx \frac{1}{x} - \frac{x}{3} - \frac{x^3}{45}$, the relationship (VI.28) will become:

$$\frac{(\lambda R)^2}{3} + \frac{(\lambda R)^4}{45} = Rk' \quad \text{(VI.26)}$$

After further simplification

$$\frac{3}{(\lambda R)^2} = \frac{1}{5} + \frac{D}{RkS\theta_{ox}} \quad \text{(VI.27)}$$

which results in the following expression for the relaxation time:

$$\tau = \frac{1}{15D}R^2 + \frac{1}{3kS\theta_{ox}}R \quad \text{(VI.28)}$$

The relationship (VI.18) for θ_{ox} will convert (VI.21) into:

$$\tau = \frac{1}{15D}R^2 + \frac{1}{3kKC_{ox}S}R + \frac{1}{3kS}R \quad \text{(VI.29)}$$

D. Reaction rate measurements

A series of UV-Vis experiments studying oxidation of tungsten bronze thin films of different thicknesses in a 0.1M solution of nitrobenzene in Hexanes has been carried out. The plot showing the dependence of the relaxation time τ of the film thickness is given in Fig. VI-3. It is seen from the data that the relaxation time increases with the increase of the film thickness, which supports the assumption about involvement of the diffusion process in the rate dependence. The plot indicates that at low thickness the fitting curve lies above the experimental points. The possible explanation for this phenomenon can be surface defects at low thickness, which result in larger reaction rates than those predicted theoretically. Using the relationship (VI.13) the value of the diffusion coefficient D was estimated to be 4×10^{-15} cm^2/s, which is consistent with the results obtained in NMR studies.[90]

The plot of relaxation time versus concentration of nitrobenzene is given in Fig. VI-4. The thickness of the films in all measurements was equal to 103 nm. The fit based on equation (VI.20) results in the value of kKS for nitrobenzene equal to 1.60×10^{-11} m/(s*M). From the Van der Waals coefficient for nitrobenzene b=0.14 L/mol the surface area of one nitrobenzene molecule is estimated to be equal to 1.82×10^{-19} m^2. S in this case will be: $S = \dfrac{1}{6.02\times10^{23}\,mol^{-1}\times1.82\times10^{-19}\,m^2} = 9.17\times10^{-6}\,\dfrac{mol}{m^2}$

And the value of kK is: $kK = \dfrac{1.60\times10^{-14}\,\dfrac{m^4}{s\bullet mol}}{9.17\times10^{-6}\,\dfrac{mol}{m^2}} = 1.75\times10^{-9}\,\dfrac{m^6}{s\bullet mol^2}$

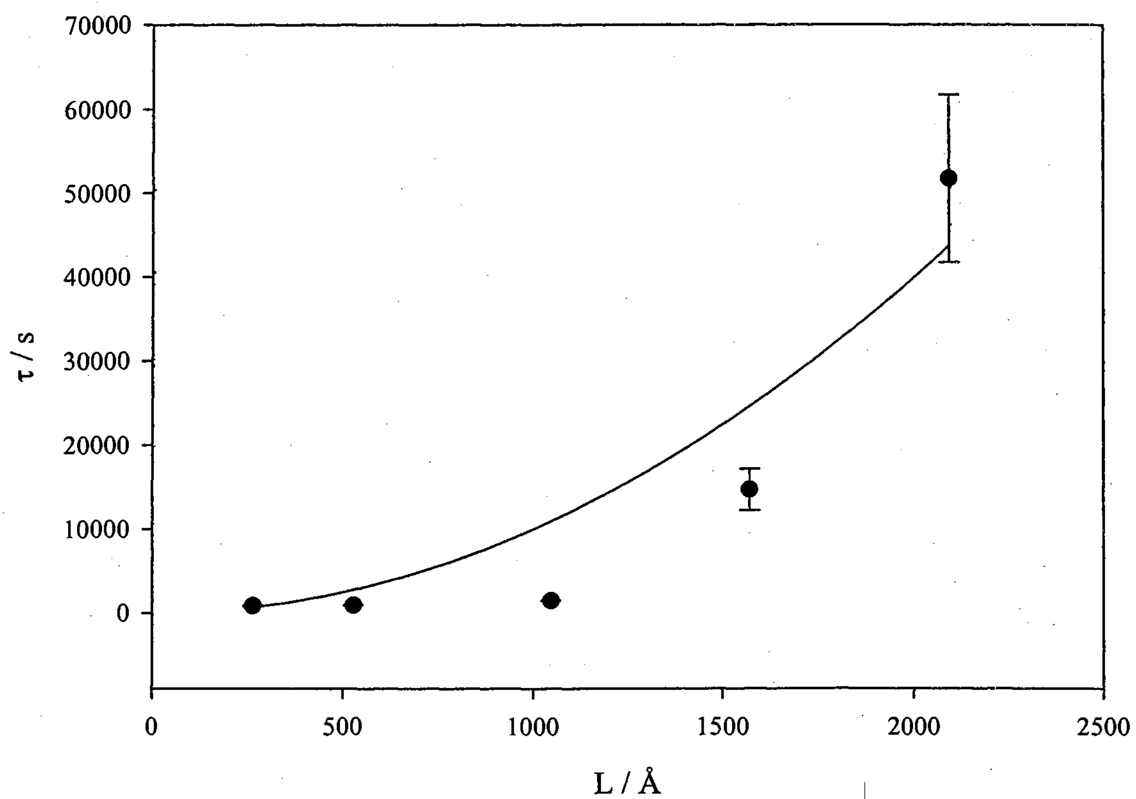

Figure VI-3. Thickness dependence of the relaxation time for H_xWO_3 thin films oxidized in 0.1M solution of nitrobenzene in Hexanes.

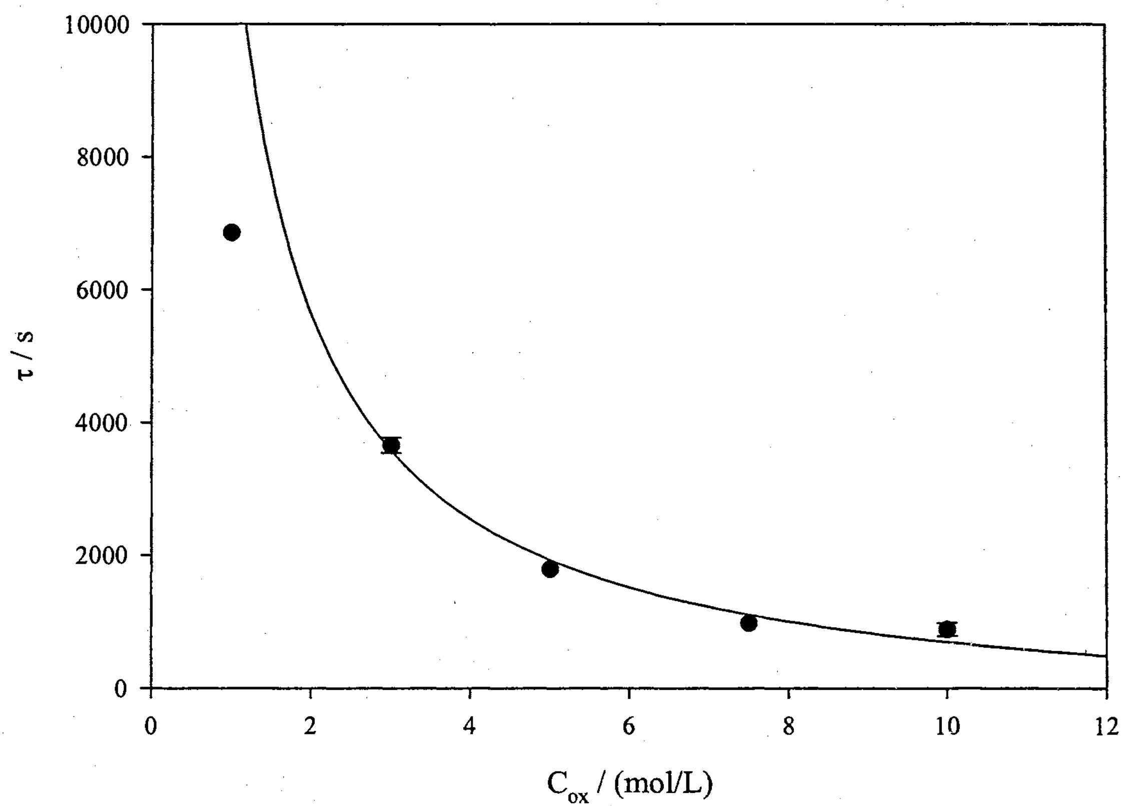

Figure VI-4. Concentration dependence of the relaxation time for 103 nm H_xWO_3 thin films oxidized in the solution of nitrobenzene in n-Hexane.

E. Conclusions

The kinetics of oxidation of polycrystalline hydrogen tungsten bronze thin films has two parameters. First, it depends on the diffusion of hydrogen from the bulk to the surface of the film. The second constituent is the reaction of surface hydrogen with the oxidizing agent. The resulting kinetic model has an exponential form, analogous to that for the regular first order reaction with respect to the total concentration of hydrogen atoms in the bronze films. This model allows estimating both the diffusion coefficient for the tungsten bronze film and reaction constant for the surface reaction. For the tungsten oxides prepared by thermal oxidation of microcrystalline W thin films, obtained by sputter deposition, the diffusion coefficient is equal to 4×10^{-15} cm^2/s. This result is close to the value obtained with the help of NMR measurements.

CONCLUDING REMARKS

A. Adsorption and decomposition of cyanogen halides on Si(100) surface.

Adsorption and decomposition of ICN, BrCN and ClCN on Si(100) surface were studied both experimentally and theoretically. Experimental techniques included XPS, UPS and TPD while quantum computations have been done with the help of Gaussian98 software. The investigations reveal that at low temperature (100K) some part of XCN adsorbs molecularly via Si-N dative bond whereas the rest adsorbs dissociatively forming –CN and –X species on the surface. Energetically such a behavior is related to the transition barrier existing on a pathway between molecularly adsorbed configuration and dissociated state on the surface. At low temperature a part of molecularly adsorbed species possesses not enough energy to overcome this transition barrier and reach the most energetically stable dissociated structure. However, heating the system up to the room temperature causes the complete dissociation of XCN on Si(100) resulting in appearance of only CN and X species bound to the surface. Further temperature increase results in disappearance of the CN species and formation of carbides and nitrides on Si(100) surface. Absence of XCN stable "side-on" configuration, in which carbon and nitrogen are attached to Si surface, in experimental observations comes from possible dissociation pathways perpendicular to the Si-Si dimer bond with lower potential barriers. Such pathways necessarily implement the use of silicon clusters with two and more dangling bonds parallel to each other. The resulting cluster size effect influences only on

the energetics of the molecularly adsorbed "end-on" structure but makes no difference for "side-on" and dissociated configuration. Such difference for the end-on structures can be explained by the formation of a dative bond between nitrogen and silicon atom and, therefore, larger effect of delocalization of donated electron density with increasing size of a cluster. However, the use of a double dimer v-trench cluster, in which two dimer bonds are not parallel to each other, but lie on the same line, results in almost no cluster size effect for the end-on adsorption structure. Therefore, for Si(100)-2×1 configuration the delocalization effect is significant along the dimer rows and small in the direction perpendicular to the dimer rows.

Energetics of the second ClCN molecule adsorption on Si(100) surface was also studied. The energy of the second-molecule adsorption strongly depends on the position and configuration of the first molecule which "poisons" certain adsorption sites. If the first ClCN molecule dissociates on the surface the adsorption energy of the second molecule icnreases comparatively to the energy released in the process of adsorption of a fisrt ClCN molecule. In this case it occurs most easily on a dissociated structure, provided that CN and Cl are bonded to the opposite sides of different dimer bonds. However, when both ClCN molecules are in the end-on position the adsorption energy for the second molecule is lower than that for the first molecule. It is mostly favorable when ClCN goes to the electropositive Si atom, determined by the buckling of the dimer bonds and corresponding charge distribution. The "poisoning" effect is negligible for the adsorption of the second molecule on the electrophilic site of the adjacent dimer row, however, it becomes more significant when it goes to the more adsorption unfavorable "buckled-up" site.

B. Characterization and chemical reaction kinetics of microcrystalline tungsten bronze thin films.

Hydrogen tungsten bronze thin films were prepared in two steps. First, sputtered tungsten thin films were thermally oxidized in a stream of oxygen gas at 400°C. Second, the obtained tungsten oxide films were reduced to bronze by means of wet Zn/HCl technique or direct hydrogen gas exposure in a UHV chamber. The films were characterized by means of XPS, UPS, SEM, UV-Vis and XRD techniques. Both tungsten oxide and tungsten bronze display cubic polycrystalline structure, which is typical for tungsten bronzes with high hydrogen content. XPS spectra show that hydrogen bronze films are indistinguishable from tungsten bronze powder by composition. The electronic bandstructure of bronzes, studied by UPS and UV-Vis spectroscopy, is similar to that for a doped semiconductor having electrons in a lower conduction band.

Kinetic studies of the tungsten bronze thin films reaction with nitrobenzene show that the total concentration of hydrogen species in a film depends on both the diffusion of hydrogen from the bulk to the surface and the kinetics of surface hydrogen reaction with nitrobenzene molecules. Combination of these two parameters results in a complex model with the exponential time dependence of total hydrogen concentration in a film. Proper fitting this model to the experimental data allows estimating the diffusion coefficient of tungsten oxide film and the second-order reaction constant for the surface reaction of hydrogen atoms with nitrobenzene. The value of the diffusion coefficient is equal to 4×10^{-15} cm^2/s, consistent with the results previously obtained by NMR measurements.

BIBLIOGRAPHY FOR CHAPTERS I-III

1. Yates, J., Jr., *Science* **1998,** *279,* 335.
2. Bent, S.F., *Surf. Sci.* **2002,** *500,* 879.
3. Pollmann, J. and Kruger, P., in *Handbook of Surface Science*, K. Horn and M. Scheffler, Editors. 2000, Institut fur Theoretische Physik II-Festkorperphysik Universitat Munster: Munster, Germany. p. 93.
4. Liu, Q. and Hoffmann, R., *J. Am. Chem. Soc.* **1995,** *117,* 4082.
5. Appelbaum, J.A., Baraff, G.A., and Hamann, D.R., *Phys. Rev. B.* **1976,** *14,* 588.
6. Redondo, A. and Goddard, W.A., III, *J. Vac. Sci. Technol. A* **1982,** *21,* 344.
7. Chadi, D.J., *Phys. Rev. Lett.* **1979,** *43,* 43.
8. Hamers, R.J., Tromp, R.M., and Demuth, J.E., *Phys. Rev. B.* **1986,** *34*(8), 5343.
9. Wolkow, R., *Phys. Rev. Lett.* **1992,** *68*(17), 2636.
10. Yokoyama, T. and Takayanagi, K., *Phys. Rev. B* **2000,** *61*(8), R5078.
11. Paulus, B., *Surf. Sci.* **1998,** *408,* 195.
12. Shoemaker, J., Burggraf, L.W., and Gordon, M.S., *J. Chem. Phys.* **2000,** *112,* 2994.
13. Tomasek, M., *Progress in Surface Science* **1987,** *25*(1-4), 147.
14. Tomasek, M. and Pick, S., *Czechoslovak Journal of Physics, B* **1988,** *38*(1), 97.
15. Hamers, R.J. and Wang, Y., *Chem. Rev.* **1996,** *96,* 1261.
16. Lu, X. and Lin, M.C., *Int. Reviews in Physical Chemistry* **2002,** *21*(1), 137.

17. Mui, C., Wang, G.T., Bent, S.F., and Musgrave, C.B., *J. Chem. Phys.* **2001**, *114*(22), 10170.

18. Cao, X., Coulter, S.K., Ellison, M.D., Liu, H., Liu, J., and Hamers, R.J., *J. Phys. Chem. B* **2001**, *105*(18), 3759.

19. Cao, X. and Hamers, R.J., *J. Am. Chem. Soc.* **2001**, *123*(44), 10988.

20. Widjaja, Y. and Musgrave, C.B., *Surf. Sci.* **2000**, *469*(1), 9.

21. Widjaja, Y., Mysinger, M.M., and Musgrave, C.B., *J. Phys. Chem. B* **2000**, *104*(11), 2527.

22. Bu, Y. and Lin, M.C., *Surf. Sci.* **1994**, *311*, 385.

23. Tindall, C., Li, L., Takaoka, O., Hasegawa, Y., and Sakurai, T., *J. Vac. Sci. Technol. A* **1997**, *15*, 1155.

24. Tindall, C., Li, L., Takaoka, O., Hasegawa, Y., and Sakurai, T., *Surf. Sci.* **1997**, *380*, 481.

25. Bu, Y., Chu, J.C.S., and Lin, M.C., *Surf. Sci.* **1992**, *264*, L151.

26. Jonathan, N.B.H., Knight, P.J., and Morris, A., *Surf. Sci.* **1992**, *275*, L640.

27. Bu, Y. and Lin, M.C., *Surf. Sci.* **1993**, *298*, 94.

28. Bacalzo, F.T., Musaev, D.G., and Lin, M.C., *J. Phys. Chem.* **1998**, *102*, 2221.

29. Hu, D., Ho, W., Chen, X., Wang, S., and Goddard, W.A., *Phys. Rev. Lett.* **1997**, *78*, 1178.

30. Imamura, Y., Matsui, N., Morikawa, Y., Hada, M., Kubo, T., Nishijima, M., and Nakatsuji, H., *Chem. Phys. Lett.* **1998**, *287*, 131.

31. Lu, X., Zhang, Q., and Lin, M.C., *Phys. Chem. Chem. Phys.* **2001**, *3*, 2156.

32. Armstrong, J.L., White, L.M., and Langell, M., *J. Vac. Sci. Technol. A* **1997**, *15*, 1146.

33. Tanaka, S., Onchi, M., and Nishijima, M., *J. Chem. Phys.* **1989**, *91*, 2712.

34. Ikeura-Sekiguchi, H. and Sekiguchi, T., *Surf. Sci.* **1997**, *390*, 214.

35. Ikeura-Sekiguchi, H. and Sekiguchi, T., *Surf. Sci.* **1999**, *433-435*, 549.

36. Bu, Y. and Lin, M.C., *Langmuir* **1994**, *10*, 3621.

37. Qiao, M.H., Cao, Y., Deng, J.F., and Xu, G.Q., *Chem. Phys. Lett.* **2000**, *325*, 508.

38. Luo, H. and Lin, M.C., *Chem. Phys. Lett.* **2001**, *343*, 219.

39. Qiao, M.H., Cao, Y., Tao, F., Liu, Q., Deng, J.F., and Xu, G.Q., *J. Phys. Chem. B.* **2000**, *104*, 11211.

40. Jeong, H.D., Lee, Y.S., and Kim, S., *J. Chem. Phys.* **1996**, *105*, 5200.

41. Bu, Y. and Lin, M.C., *J. Phys. Chem.* **1994**, *98*, 7871.

42. Takayanagi, K., Tanishiro, Y., Takahashi, M., and Takahashi, S., *J. Vac. Sci. Technol. A* **1985**, *3*, 1502.

43. Northrup, J.E., *Phys. Rev. Lett.* **1986**, *57*, 154.

44. Hamers, R.J., Tromp, R.M., and Demuth, J.E., *Surf. Sci.* **1987**, *181*, 246.

45. Wolkow, R. and Avouris, P., *Phys. Rev. Lett.* **1988**, *60*, 1049.

46. Bu, Y., Shinn, D.W., and Lin, M.C., *Surf. Sci.* **1992**, *276*(1-3), 184.

47. Bu, Y. and Lin, M.C., *Surf. Sci.* **1994**, *301*, 118.

48. Bu, Y., Breslin, J., and Lin, M.C., *J. Phys. Chem. B* **1997**, *101*, 1872.

49. Bu, Y. and Lin, M.C., *J. Chin. Chem. Soc. (Taipei)* **1995**, *42*(2), 309.

50. Edamoto, K., Kubota, Y., Onchi, M., and Nishijima, M., *Surf. Sci.* **1984**, *146*, L533.

51. Bu, Y., Ma, L., and Lin, M.C., *J. Phys. Chem.* **1993**, *97*, 11797.

52. Shirota, N., Tagi, S., Taniguchi, M., and Hashimoto, E., *J. Vac. Sci. Technol. A* **2000**, *18*, 2578.

53. Bu, Y., Ma, L., and Lin, M.C., *J. Phys. Chem.* **1995**, *99*(3), 1046.

54. Macpherson, C.D., Hu, D.Q., and Leung, K.T., *Surf. Sci.* **1992**, *276*, 156.

55. Hu, D.Q., Macpherson, C.D., and Leung, K.T., *Solid St. Commun.* **1991**, *78*, 1077.

56. Huang, C., Widdra, W., and Weinberg, W.H., *Surf. Sci.* **1994**, *315*(1-2), L953.

57. Lu, X., *J. Am. Chem. Soc.* **2003**, *125*, 6384.

58. Lopinski, G.P., Maffatt, D.J., Wayner, D.D.M., and Wolkow, R.A., *J. Am. Chem. Soc.* **2000**, *122*, 3548.

59. Lu, X. and Zhu, M., *Chem. Phys. Lett.* **2004**, *393*, 124.

60. Preuss, M., Schmidt, W.G., and Bechstedt, F., *J. Phys. Chem. B.* **2004**, *108*, 7809.

61. Silvestrelli, P.L., *Surf. Sci.* **2004**, *552*, 17.

62. Chen, L.C., Chen, K.H., Wu, J.-J., Bhusari, D.M., and Lin, M.C., *Silicon-Based Materials and Devices: Materials and Processing*, H.S. Nalwa, Editor. 2001, Academic Press: New York. p. 73.

63. Bhusari, D.M., Chen, C.K., Chen, K.H., Chuang, T.J., Chen, L.C., and Lin, M.C., *J. Mater. Res.* **1997**, *12*, 322.

64. Chen, L.C., Yang, C.Y., Bhusari, D.M., Chen, K.H., Lin, M.C., Lin, J.C., and Chuang, T.J., *Diamond Relat. Mater.* **1996**, *5*, 514.

65. Chen, L.C., Bhusari, D.M., Yang, C.Y., Chen, K.H., Chuang, T.J., Lin, M.C., Chen, C.K., and Huang, Y.F., *Thin Solid Films* **1997**, *303*, 66.

66. Bu, Y., Ma, L., and Lin, M.C., *J. Phys. Chem.* **1993**, *97*(27), 7081.

67. Bacalzo-Gladden, F., Musaev, D.G., and Lin, M.C., *J. Chin. Chem. Soc. (Taipei)* **1999**, *46*(3), 395.

68. Bacalzo-Gladden, F., Lu, X., and Lin, M.C., *J. Phys. Chem. B* **2001**, *105*, 4368.

69. Wang, J.-H. and Lin, M.C., *J. Phys. Chem. B* **2004**, *108*, 9189.

70. Tao, F., Wang, Z.H., Qiao, M.H., Liu, Q., Sim, W.S., and Xu, G.Q., *J. Chem. Phys.* **2001**, *115*(18), 8563.

71. Bournel, F., Gallet, J.J., Kubsky, S., Dufour, G., Rochet, F., Simeoni, M., and Sirotti, F., *Surf. Sci.* **2002**, *513*(1), 37.

72. Miotto, R., Oliveira, M.C., Pinto, M.M., de Leon-Perez, F., and Ferraz, A.C., *Phys. Rev. B.* **2004**, *69*(23), 235331/1.

73. Ellison, M.D. and Hamers, R.J., *J. Phys. Chem. B* **1999**, *103*, 6243.

74. Tao, F., Wang, Z.H., and Xu, G.Q., *J. Phys. Chem.* **2002**, *106*, 3557.

75. Rajasekar, P., Kadossov, E.B., Watt, T., and Materer, N.F., *Surf. Sci.* **2002**, *515*(2-3), 421.

76. Rajasekar, P., Kadossov, E.B., Ward, L., Baker, J.L., and Materer, N.F., *J. Phys. Chem. B.* **2003**, *107*, 7726.

77. Eland, J.H.D., Baltzer, P., Lundqvist, Wannberg, B., and Karlsson, L., *Chem. Phys.* **1996**, *212*, 457.

78. Eland, J.H.D., Baltzer, P., Karlsson, L., and Wannberg, B., *Chem. Phys.* **1997**, *222*, 229.

79. Heilbronner, E., Hornung, V., and Muszkat, K.A., *Helvetica Chimica Acta* **1970**, *53*, 347.

80. Hollas, J.M. and Sutherley, T.A., *Mol. Phys.* **1971**, *22*(2), 213.

81. Kovac, B., *J. Phys. Chem.* **1987**, *91*, 4231.

82. Lake, R.F. and Thompson, H., *Proc. Royal Soc. London Ser. A* **1970**, *317*(1529), 187.

83. Yee, D.S.C. and Brion, C.E., *J. Electron Spectrosc. Relat. Phenom.* **1976**, *8*, 313.

84. Yates, J.T., *Experimental Innovations in Surface Science*. 1997, Berlin: Springer.

85. Nishino, H., Yang, W., Dohnalek, Z., Ukraintsev, V.A., Choyke, W.J., and Yates, J.T., *J. Vac. Sci. Technol. A* **1997**, *11*, 182.

86. Bak, B. and Hillebert, A., *Cyanogen Iodide*, in *Organic Synthese*, N. Rabjohn, Editor. 1963, John Wiley & Sons.

87. Marshall, K.R. and Jones, R.G., *J. Vac. Sci. Technol. A* **1993**, *11*, 2024.

88. *Cyanogen Chloride*, in *Handbook of Preparative Inorganic Chemistry*, G. Brauer, Editor. 1963, Academic Press. p. 662.

89. Popov, C., Plass, M.F., Bergmaier, A., and Kulisch, W., *Appl. Phys.* **1999**, *A 69*, 241.

90. Hammer, P., Lacerda, R.G., R. Droppa, J., and Alvarez, F., *Diamond Relat Mater.* **2000**, *9*, 577.

91. Bondino, F., Baraldi, A., Comelli, G., and Netzer, F.P., *Surf. Sci.* **2000**, *461*(1-3), 31.

92. Davis, D.D. and Okabe, H., *J. Chem. Phys.* **1968**, *49*, 5526.

93. Chakarian, V., Shuh, D.K., Yarmoff, J.A., Hakansson, M.C., and Karlsson, U.O., *Surf. Sci.* **1993**, *296*, 383.

94. Dean, J.A., *Lange's Handbook of Chemistry*. 14 ed. 1992: McGraw-Hill.

95. PHI, *Handbook of X-Ray Photoelectron Spectroscopy.* 1977.

96. Jones, R.G. and Kadodwala, M., *Surf. Sci. Lett.* **1997**, *370*, L219.

97. Kruger, B. and Benndorf, C., *Surf. Sci.* **1986**, *177*, 515.

98. Johansson, L.S.O., Uhrberg, R.I.G., Lindsay, R., Wincott, P.L., and Thornton, G., *Phys. Rev. B* **1990**, *42*, 9534.

99. Martin-Gago, J.A., Roman, E., Refolio, M.C., Lopez-Sancho, J.M., Rubio, J., Hellner, L., and Comelli, G., *Surf. Sci.* **1999**, *424*, 82.

100. Michel, E.G., Pauly, T., Etelaniemi, V., and Materlik, G., *Surf. Sci.* **1991**, *241*, 111.

101. Frisch, M.J., Trucks, G.W., Schlegel, H.B., Scuseria, G.E., Robb, M.A., Cheeseman, J.R., Zakrzewski, V.G., J. A. Montgomery, J., Stratmann, R.E., Burant, J.C., Dapprich, S., J. M. Millam, Daniels, A.D., Kudin, K.N., Strain, M.C., Farkas, O., Tomasi, J., Barone, V., Cossi, M., Cammi, R., Mennucci, B., Pomelli, C., Adamo, C., Clifford, S., Ochterski, J., Petersson, G.A., Ayala, P.Y., Cui, Q., Morokuma, K., Malick, D.K., Rabuck, A.D., Raghavachari, K., Foresman, J.B., Cioslowski, J., Ortiz, J.V., Baboul, A.G., Stefanov, B.B., Liu, G., Liashenko, A., Piskorz, P., Komaromi, I., Gomperts, R., Martin, R.L., Fox, D.J., Keith, T., Al-Laham, M.A., Peng, C.Y., Nanayakkara, A., Gonzalez, C., Challacombe, M., Gill, P.M.W., Johnson, B., Chen, W., Wong, M.W., Andres, J.L., Gonzalez, C., Head-Gordon, M., Replogle, E.S., and Pople, J.A., *Gaussian 98. Revision A.7.* 1998, Pittsburgh, PA: Gaussian Inc.

102. Kadossov, E.B., Rajasekar, P., and Materer, N.F., *Chem. Phys. Lett.* **2003**, *370*(3,4), 548.

103. Kadossov, E.B., Rajasekar, P., and Materer, N.F., *J. Phys. Chem. B.* **2004**, *108*, 303.

104. Becke, A.D., *J. Chem. Phys.* **1993**, *98*, 5648.

105. Lee, C., Yang, W., and Parr, R.G., *Phys. Rev. B* **1988**, *37*, 785.

106. Francl, M.M., Pietro, W.J., Hehre, W.J., Binkley, J.S., Gordon, M.S., DeFrees, D.J., and Pople, J.A., *J. Chem. Phys.* **1982**, *77*, 3654.

107. Dunning, T.H. and Hay, P.J., *g98 basis set reference*, in *Modern Theoretical Chemistry*, H.F. Schaefer, Editor. 1977. p. 1.

108. Hay, P.J. and Wadt, W.R., *J. Chem. Phys.* **1985**, *82*, 270.

109. Carman, A.J., Zhang, L., Liswood, J.L., and Casey, S.M., *J. Phys. Chem.* **2003**, *107*, 5491.

110. Kato, T., Kang, S.-Y., Xu, X., and Yamabe, T., *J. Phys. Chem. B* **2001**, *105*, 10340.

111. Widjaja, Y. and Musgrave, C.B., *Phys. Rev. B* **2001**, *64*(20), 205303/1.

112. Samuni, U., Kahana, S., Fraenkel, R., Haas, Y., Danovich, D., and Shaik, S., *Chem. Phys. Lett.* **1994**, *225*, 391.

113. Pople, J.A., Head-Gordon, M., and Raghavachari, K., *J. Chem. Phys.* **1987**, *87*, 5968.

114. Thompson, G. and Maki, A.G., *J. Mol. Spectrosc.* **1993**, *106*, 73.

115. Cazzolli, G., Esposti, C.D., and Favero, P.G., *J. Mol. Struct.* **1978**, *48*, 1.

116. Petrie, S., *Phys. Chem. Chem. Phys.* **1999**, *1*, 2897.

117. Townes, C.H., Holden, A.N., and Merritt, F.R., *Phys. Rev.* **1948**, *74*, 1113.

118. Lee, T.J., Martin, J.M.L., Dateo, C.E., and Taylor, P.R., *J. Phys. Chem.* **1995**, *99*, 15858.

119. Lafferty, W.J., Lide, D.R., and Toth, R.A., *J. Chem. Phys.* **1965**, *43*, 2063.

120. Lu, X., Xu, X., Wu, J., Wang, N., and Zhang, Q., *New J. Chem.* **2002**, *26*, 160.

121. Bent, H.A., *Chem. Rev.* **1960**, *61*, 275.

122. Gonzalez, C. and Schiegel, B., *J. Phys. Chem.* **1990**, *94*, 5523.

123. Gonzalez, C. and Schiegel, B., *J. Chem. Phys.* **1989**, *90*, 2154.

124. Cho, J.-H. and Kleinman, L., *J. Chem. Phys.* **2003**, *119*(13), 6744.

BIBLIOGRAPHY FOR CHAPTERS IV-VI

1. Bartha, L. and Kiss, A.B., *Int. J. of Refractory Metals & Hard Materials* **1995**, *13*, 77.
2. Sum, H.-T., Cantalini, C., Lozz, L., Passacantando, M., Santucci, S., and Delino, M., *Thin Solid Films* **1996**, *287*, 258.
3. Sberveglieri, G., Depero, L., Groppelli, S., and Nelli, P., *Sensors and Actuators B* **1995**, *26-27*, 89.
4. Wang, S.-H., Chou, T.-C., and Liu, C.-C., *Sensors and Actuators B* **2003**, *94*, 343.
5. Lampert, C.M., *Sol. Energy Mater.* **1984**, *11*, 1.
6. Svenson, J. and Granqvist, C., *Appl. Phys. Lett.* **1984**, *45*, 828.
7. Faughnan, B.W. and Crandall, R.S., in *Topics in Applied Physics*, J. Pankov, Editor. 1980, Springer: Berlin.
8. Agniohotry, S.A., Saini, K.K., and Chandra, S., *Indian J. Pure Appl. Phys.* **1986**, *24*, 19.
9. Baucke, F.G.K., *Sol. Energy Mater.* **1987**, *16*, 67.
10. Deneuville, A. and Gerard, P., *J. Electron. Mater.* **1978**, *7*, 559.
11. Mucke, K., Bohm, F., Gambke, T., Ottermann, C., and Bange, K., *SPIE* **1990**, *1323*, 188.
12. Hichwa, B.P., Caskey, G., Betz, D.F., and Harlow, J.D., *J. Vac. Sci. Technol. A*

1987, *5*, 1775.

13. Davazoglou, D., Donnadieu, A., Fourcade, R., Hugot-le Goff, A., Delichere, P., and Perez, A., *Rev. Phys. Appl.* **1988**, *23*, 265.

14. Davazoglou, D., Leveque, G., and Donnadieu, A., *Sol. Energy Mater.* **1988**, *17*, 379.

15. Tracy, C.E. and Benson, D.K., *J. Vac. Sci. Technol. A* **1986**, *4*, 2377.

16. Delichere, P., Falaras, P., Froment, M., Hugot-le Goff, A., and Agius, B., *Thin Solid Films* **1988**, *161*, 35.

17. Ohtsuka, T., Goto, N., and Sato, N., *J. Electroanal. Chem.* **1990**, *287*, 249.

18. Unuma, H., Tonooka, K., Suzuki, Y., Furusaki, T., Kodaira, K., and Matsushita, T., *J. Mater. Sci. Lett.* **1986**, *5*, 1248.

19. Yamanaka, K., Oakamoto, H., Kidou, H., and Kudo, T., *Jpn. J. Appl. Phys.* **1986**, *25*, 1420.

20. Habib, M.A., Maheswari, S.P., and Carpenter, M.K., *J. Appl. Electrochem.* **1991**, *21*, 203.

21. Baba, N. and Yohino, T., *J. Appl. Electrochem.* **1982**, *12*, 607.

22. Miles, M.H., Stilwell, D.E., Hollins, R.A., and Henry, R.A., in *Electrochromic Materials*, M.K. Carpenter and D.A. Corrigan, Editors. 1990, The Electrochemical Society: Pennington. p. 137.

23. Wertheim, G.K., Campagna, M., Chazalviel, J.-N., Buchanan, D.N.E., and Shanks, H.R., *Appl. Phys.* **1977**, *13*, 225.

24. Gerand, G., Nowogrocki, G., Guenot, J., and Figlarz, M., *J. Solid State Chem.* **1979**, *29*, 429.

25. Deb, S.K., *Appl. Opt. (Suppl.3)* **1969**, 192.

26. Crandall, R.S. and Faughnan, B.W., *Appl. Phys. Lett.* **1976**, *28*, 95.

27. Wittwer, V., Schirmer, O.F., and Schlotter, P., *Solid State Commun.* **1978**, *25*, 977.

28. Schirmer, O.F., Wittwer, V., Baur, G., and Brandt, G., *J. Electrochem. Soc.* **1977**, *124*, 749.

29. Granqvist, C.G., *Appl. Phys. A* **1993**, *57*, 3.

30. Kukuev, V.I., Tutov, E.A., Domashevskaya, E.P., Yanovskaya, M.I., Obvintseva, I.E., and Venevtsev, Y.N., *Soviet Phys. Tech. Phys.* **1987**, *32*, 1176.

31. Niehus, H., *Surf. Sci.* **1978**, *78*, 667.

32. Bange, K., *Sol. Energy Mater.* **1999**, *58*, 1.

33. Goulding, M.R., Thomas, C.B., and Hurditch, R.J., *Solid State Commun.* **1983**, *46*, 451.

34. Shigesato, Y., *Jpn. J. Appl. Phys.* **1991**, *30*, 1457.

35. Kukuev, V.I., Komolova, L.F., Lesovoy, M.V., and Tomaspolsky, Y.Y., *J. Microsc. Spectrosc. Electron.* **1989**, *14*, 471.

36. Gerard, P., Deneuville, A., and Courths, R., *Thin Solid Films* **1980**, *71*, 221.

37. Bechinger, C., Herminghaus, S., and Leiderer, P., *Thin Solid Films* **1994**, *239*, 156.

38. Bechinger, C., Oetinger, G., Herminghaus, S., and Leiderer, P., *J. Appl. Phys.* **1993**, *74*, 4527.

39. Kikuchi, E., Hirota, N., Fujishima, A., Itoh, K., and Marabayashi, M., *J. Electroanal. Chem.* **1995**, *381*, 15.

40. Garrilynk, A.I., Zakarchenya, B.P., and Chudnovskii, F.A., *Sov. Tech. Phys. Lett.* **1980**, *6*, 512.

41. Garrilynk, A.I., Lanskaya, T.G., and Chudnovskii, F.A., *Sov. Tech. Phys. Lett.* **1987**, *32*, 964.

42. Nagasu, M. and Koshida, N., *Appl. Phys. Lett.* **1990**, *57*, 1324.

43. Kikuchi, E., Iida, K., and Fujishima, A., *J. Electroanal. Chem.* **1993**, *351*, 105.

44. Yao, J.N., Loo, B.H., and Fujishima, A., *Ber. Bunsenges. Phys. Chem.* **1990**, *94*, 13.

45. Bange, K., Martens, U., Nemetz, A., and Temmink, A., in *Electrochromic Materials, Proc.*, M.K. Carpenter and D.A. Corrigan, Editors. 1990, The Electrochemical Society: Pennington, USA. p. 334.

46. Delichere, P., Falaras, P., and Hugot-le Goff, A., *Sol. Energy Mater.* **1989**, *19*, 323.

47. Dautremont-Smith, W.C., *Displays* **1982**, *3*, 67.

48. Chang, I.F., Gilbert, B.L., and Sun, T.I., *J. Electrochem. Soc.* **1975**, *122*, 955.

49. Dickens, P.G. and Whittingham, M.S., *Q. Rev. Chem. Soc.* **1968**, *22*, 30.

50. Green, M., Smith, W.C., and Weiner, J.A., *Thin Solid Films* **1976**, *38*, 89.

51. Hersh, N.H., Kramer, W.E., and McGee, J.H., *Appl. Phys. Lett.* **1975**, *27*, 646.

52. Green, M. and K.S., K., *Thin Solid Films* **1977**, *40*, L19.

53. Patil, P.R., Pawar, S.H., and Patil, P.S., *Solid State Ionics* **2000**, *136-137*, 505.

54. Yao, J.N., Chen, P., and Fujishima, A., *J. Electroanal. Chem.* **1996**, *406*, 223.

55. Vertes, A. and Schiller, R., *J. Appl. Phys.* **1983**, *54*, 199.

56. Vertes, A. and Schiller, R., *Studies in Inorganic Chemistry* **1982**, *3*, 299.

57. Kamimory, T., Nagai, J., and Mizuhashi, M., *Proc. SPIE* **1983**, *428*, 51.

58. Hitchman, M., *Thin Solid Films* **1979**, *61*, 341.

59. Rauh, R.D., *Solid State Ionics* **1988**, *28-30*, 1479.

60. Schweiger, D., Georg, A., Graf, W., and Witter, V., *Sol. Energy Mater. & Solar Cells* **1998**, *54*, 99.

61. Zhuang, L., Xu, X., and Shen, H., *Surf. Coatings Tech.* **2003**, *167*, 217.

62. Fruhberger, B., Grunze, M., and Dwyer, D.J., *Sensors and Actuators B* **1996**, *31*, 167.

63. Penza, M., Cassano, G., and Tortorella, F., *Sensors and Actuators B* **2001**, *81*, 115.

64. Meixner, H., Gerblinger, J., Lampe, U., and Fleischer, M., *Sensors and Actuators B* **1995**, *23*, 119.

65. Rye, R.R. and Ricco, A.J., *J. Appl. Phys.* **1987**, *62*, 1084.

66. Dwyer, D.J., *Sensors and Actuators B* **1991**, *5*, 155.

67. Nishimura, N., Aikawa, Y., and Sukigara, M., *Nippon Shashin Gakkaishi* **1985**, *48*(6), 421.

68. Opara-Krasovec, U., Jese, R., Orel, B., Grdadolnik, J., and Drazic, G., *Monatshefte fur Chemie* **2002**, *133*, 1115.

69. Apblett, A.W., Kiran, B.P., and Oden, K., *ACS Symposium Series* **2003**, *837*, 154.

70. Kim, D.-J. and Pyun, S.-I., *J. Corros. Sci. Soc. of Korea* **1996**, *27*(4), 442.

71. Bringans, R.D., Hochst, H., and Shanks, H.R., *Phys. Rev. B* **1981**, *24*(6), 3481.

72. Salje, E. and Viswanathan, K., *Acta. Crystallogr. Sec. A* **1975**, *31*, 356.

73. Balazsi, C., Farkas-Jahnke, M., Kotsis, I., Petras, L., and Pfeifer, J., *Solid State Ionics* **2001**, *141-142*, 411.

74. Perry, W.L., Smith, B.L., Bullian, C.J., Busse, J.R., Macomber, C.S., Dye, R.C., and Son, S.F., *Propellants, Explosives, Pyrotechnics* **2004**, *29*(2), 99.

75. Ozkan, E., Lee, S.-H., Tracy, C.E., Pitts, J.R., and Deb, S.K., *Sol. Energy Mater.* **2003**, *79*, 439.

76. Dickens, P.G. and Hurditch, R.J., *Nature* **1967**, *215*, 1266.

77. Agnihotry, S.A., Rashmi, Ramchandran, R., and Chandra, S., *Sol. Energy Mater.* **1995**, *36*, 289.

78. Ayyappan, S. and Rao, C.N.R., *Mater. Res. Bull.* **1995**, *30*(8), 947.

79. Sienko, M.J. and Oesterreicher, H., *J. Am. Chem. Soc.* **1968**, *90*(23), 6568.

80. Barreca, D., Carta, G., Rossetto, G., Tondello, E., and Zanella, P., *Surf. Sci. Spectra* **2001**, *8*(4), 258.

81. Leftheriotis, G., Papaefthimiou, S., and Siokou, A., *Thin Solid Films* **2001**, *384*, 298.

82. Bringans, R.D., Hochst, H., and Shanks, H.R., *Surf. Sci.* **1981**, *111*, 80.

83. Hochst, H. and Bringans, R.D., *Appl. Surf. Sci.* **1982**, *11/12*, 768.

84. Bringans, R.D., Hochst, H., and Shanks, H.R., *Vacuum* **1981**, *31*(10-12), 473.

85. Tritthart, U., Gey, W., and Gavrilyuk, A., *Ionics* **1998**, *4*, 299.

86. Loo, B.H., Yao, J.N., Coble, H.D., Hashimoto, K., and Fujishima, A., *Appl. Surf. Sci.* **1994**, *81*, 175.

87. Tritthart, U., Gey, W., and Gavrilyuk, A., *Electrochemica Acta* **1999**, *44*, 3039.

88. Carslaw, H.S. and Jaeger, J.C., *Conduction of heat in solids*. 1948, Oxford: Oxford University Press.

89. Bekhta, P., Ozarkiv, I., Alavi, S., and Hiziroglu, S., (unpublished results)

90. Vannice, M.A., Boudart, M., and Fripiat, J.J., *Journal of Catalysis* **1970**, *17*, 359.

VITA #2

Evgueni Borisovich Kadossov

Candidate for the Degree of

Doctor of Philosophy

Thesis: ADSORPTION AND DECOMPOSITION OF CYANOGEN HALIDES ON Si(100) SURFACE. CHARACTERIZATION AND CHEMICAL REACTION KINETICS OF MICROCRYSTALLINE TUNGSTEN BRONZE THIN FILMS.

Major Field: Chemistry

Biographical:

Personal Data: Born in Kaliningrad, Moscow Region, Russia, On May 10, 1976.

Education: Graduated from High School #4, Yubileyny, Russia in May 1993; received Bachelor of Technics and Technology degree in Material Science and Technology of New Materials and Master of Technics and Technology degree in Material Science and Technology of New Materials from Mendeleev University of Chemical Technology of Russia, Moscow, Russia in June 1997 and June 1999, respectively. Completed the requirements for the Doctor of Philosophy degree with a major in Chemistry at Oklahoma State University in December, 2004.

Experience: Employed by Mendeleev University of Chemical Technology of Russia as an undergraduate research assistant, 1995-1997; employed by Oklahoma State University, Department of Chemistry as a graduate teaching and research assistant, 2000 to present.

Professional Memberships: American Chemical Society, American Vacuum Society, Phi Lambda Upsilon Chemical Honorary Society.